Brigham Young University
BYU ScholarsArchive

Theses and Dissertations

2004-07-12

A Ray-Based Investigation of the Statistical Characteristics and Efficient Representation of Multi-Antenna Communication Channels

Gus Ryan German
Brigham Young University - Provo

Follow this and additional works at: https://scholarsarchive.byu.edu/etd

 Part of the Electrical and Computer Engineering Commons

BYU ScholarsArchive Citation
German, Gus Ryan, "A Ray-Based Investigation of the Statistical Characteristics and Efficient Representation of Multi-Antenna Communication Channels" (2004). *Theses and Dissertations*. 145.
https://scholarsarchive.byu.edu/etd/145

This Thesis is brought to you for free and open access by BYU ScholarsArchive. It has been accepted for inclusion in Theses and Dissertations by an authorized administrator of BYU ScholarsArchive. For more information, please contact scholarsarchive@byu.edu, ellen_amatangelo@byu.edu.

www.manaraa.com

A RAY-BASED INVESTIGATION OF THE STATISTICAL CHARACTERISTICS AND EFFICIENT REPRESENTATION OF MULTI-ANTENNA COMMUNICATION CHANNELS

by

Gus R. German

A thesis submitted to the faculty of

Brigham Young University

in partial fulfillment of the requirements for the degree of

Master of Science

Department of Electrical and Computer Engineering

Brigham Young University

August 2004

www.manaraa.com

BRIGHAM YOUNG UNIVERSITY

GRADUATE COMMITTEE APPROVAL

of a thesis submitted by

Gus R. German

This thesis has been read by each member of the following graduate committee and by majority vote has been found to be satisfactory.

Date	A. Lee Swindlehurst, Chair
Date	Michael A. Jensen
Date	Michael D. Rice

www.manaraa.com

BRIGHAM YOUNG UNIVERSITY

As chair of the candidate's graduate committee, I have read the thesis of Gus R. German in its final form and have found that (1) its format, citations, and bibliographical style are consistent and acceptable and fulfill university and department style requirements; (2) its illustrative materials including figures, tables, and charts are in place; and (3) the final manuscript is satisfactory to the graduate committee and is ready for submission to the university library.

Date

A. Lee Swindlehurst
Chair, Graduate Committee

Accepted for the Department

Michael A. Jensen
Graduate Coordinator

Accepted for the College

Douglas M. Chabries
Dean, College of Engineering and Technology

www.manaraa.com

ABSTRACT

A RAY-BASED INVESTIGATION OF THE STATISTICAL CHARACTERISTICS AND EFFICIENT REPRESENTATION OF MULTI-ANTENNA COMMUNICATION CHANNELS

Gus R. German

Department of Electrical and Computer Engineering

Master of Science

Multi-antenna communication systems are attracting research interest as a means to increase the information capacity, reliability, and spectral efficiency of wireless information transfer. Ray-tracing methods predict the behavior of wireless channels using a model of the propagation environment and are a low-cost alternative to direct measurements. We use ray tracing simulations to validate the statistical time and angle of arrival characteristics of an indoor multipath channel and compare model parameter estimates with estimates derived from channel sounding measurements. Ray tracing predicts the time and angle clustering of multipaths observed in the measurements and provides model parameter estimates which are closely correlated with measured estimates. The ray tracing parameters relating to power characteristics show more deviation from measurements than the time and angle related parameters. Our results also indicate that the description of reflective scatterers in

www.manaraa.com

the propagation environment is more important to the quality of the predicted statistical behavior than the description of bulk materials. We use a ray synthesis model to investigate means of efficiently representing the channel for feedback information to the transmitter as a means to increase the information capacity. Several methods of selecting the ray-model feedback information are demonstrated with results from simulated and measured channels. These results indicate that an ESPRIT algorithm coupled with ad hoc transmit/receive pairing can yield better than 90% of the ideal waterfilling capacity when adequate training-based channel estimates are available. Additionally, we investigate a covariance feedback method for providing channel feedback for increased capacity. Both the ray-based and covariance-based feedback methods yield their highest capacity improvements when the signal to noise ratio is low. This results because of the larger benefit of focusing transmit power into the most advantageous eigenmodes of the channel when fewer eigenmodes have power allocated to them by the waterfilling capacity solution. In higher signal to noise ratio cases, more eigenmodes of the channel receive power when waterfilling, and the capacity improvement from feedback information decreases relative to a uniform power allocation. In general, ray model feedback methods are preferable because the covariance feedback quickly requires higher computational effort as the array sizes increase and typically results in lower capacity for a given amount of feedback information.

Index terms: multiple-input multiple-output (MIMO) channels, indoor multipath channels, ray tracing, channel state information feedback, information capacity

www.manaraa.com

ACKNOWLEDGMENTS

The completion of this thesis has been a singular challenge among the experiences of my life so far. The demands of this particular project took me to places where my accustomed reliance upon my God given talents and abilities did not result in the success that my previous academic experiences have conditioned me to expect, and I had to seek my Father in Heaven who is the giver of all good gifts. I am thankful now for the pain and frustration that have been my occasional companions along this journey, for they have brought me to know things that are more important than engineering – to know and rely upon the sustaining love of my Savior who is Jesus Christ, the Light of the World. For I have only come thus far by borrowing His strength to place my feet in the path that He alone could show. I desire that the honor and glory of this work may be His and that these most valuable lessons may never depart from my heart.

The faith and prayers of many loved ones have carried me when the fire of my hope and determination flickered dimly. Most of all, I am grateful for the love and constant faith of my choicest friend and companion: my wife, Tammy. Sweetheart, I dedicate this work to you as a token of my love and appreciation for the wonders you bring and make possible in my life. I rejoice that we travel together on the wild, wonderful road that we call life. Also, the encouragement of my dear family has cheered me on to "eat this old elephant." Mom and Dad, thank you for believing in me and for offering the prayers of faith that only parents can. It's a blessing to be your son. Mom Auble, thanks to you for your confidence that I can do things I have no idea about. Your love graces my life and that of my family. Finally, to many others who have shared in my struggle and strengthened me by their faith and concern. I

www.manaraa.com

prefer to think that my expressions of gratitude will be shown in the return of my love and friendship for you rather than the words of a lifeless page.

Dr. Swindlehurst, it has been an honor to be mentored by you. There were numerous occasions when you would have been fully justified in expressing disappointment or frustration with the slow development of these results. Instead, you always chose to be understanding, supportive, and patient. Thank you for allowing me the space to find my own way and for sharing your vision, experience, and considerable talents to guide me to a successful completion. I am grateful for the financial support you provided and for the kind interest you have taken in me personally.

I would like to thank Dr. Stephen P. Boyd of the Electrical Engineering Department at Stanford University for his generous assistance in formulating the MAXDET Covariance Feedback solution and for making the MAXDET software package available.

I view my experiences as a student at Brigham Young University as a time of great personal growth, preparation for the work that lies ahead, and of rich association with some of the finest people I have had the chance to know. I look back on these years with great fondness and know that they were made possible in large measure because of the generous financial support of people I may never meet. I hope that my diligent focus on my studies, participation in the community, and efforts to offer my talents in service are a worthy beginning to return the generous good that has been given to me.

Finally, I desire to acknowledge the friends who enriched my experiences in the 4th Floor of the Clyde Building. First, to my colleagues from the Telemetry Lab: Christian Bettweiser, Adam Davis, David De Gaston, and Vladimir Paje. Gentleman, those were the best of times! And, likewise to Miguel Apezteguia, Floyd Millet, Chris Peel, and Brett Walkenhorst among so many others. No distance of place or lapse of time can lessen the friendship of those who are thoroughly persuaded of each other's worth — Robert Touthey. Big D, Viva!

www.manaraa.com

Contents

www.manaraa.com

www.manaraa.com

www.manaraa.com

List of Tables

www.manaraa.com

List of Figures

www.manaraa.com

www.manaraa.com

www.manaraa.com

www.manaraa.com

Chapter 1

Introduction

Indoor wireless technologies are attracting increasing research and development efforts as the market demands data transmission applications which are extremely reliable, widely available, and operate at high data rates. Multiple Input, Multiple Output (MIMO) systems employ several antennas at both ends of a wireless transmission and have attracted significant attention because of the theoretical capacity gains which are predicted to grow linearly with the number of antenna elements - much faster than the gains from simply increasing the signal-to-noise ratio (SNR) in the system [3], [4]. The design of MIMO wireless communications networks to meet ever increasing performance demands requires deeper and more thorough understanding of the RF propagation environment and design tools that increasingly exploit the underlying structure of this environment. A variety of propagation models for MIMO channels have been proposed using both statistical and deterministic methodologies and are reviewed in [5]. This thesis contributes to this effort by validating some aspects of a proposed propagation model for indoor MIMO channels. In addition, we investigate a method for feedback of channel state information (CSI) to the transmitter for improving the channel information capacity.

The purpose of channel modeling is to describe the dominant features of observations with a mathematical construct that explains what we see and predicts the performance of algorithms, experiments, and practical communications systems. A consistent model can produce information formerly provided only by direct measurements which are time consuming and costly. The challenge is to identify the

www.manaraa.com

key features that the model should capture and to construct the model in a way that is consistent with as much of the observed channel behavior as possible without becoming cumbersome.

Propagation models for the wireless indoor channel may be constructed from either a deterministic or a statistical viewpoint. A statistical model can be based on the bulk properties of channel sounding measurements that observe the channel directly. Alternatively, we may use classical propagation theory and a knowledge of the physical indoor environment to deterministically predict the behavior of the channel. Ideally, there should be a firm agreement between deterministic channel models and the statistical behavior observed in actual channels.

This thesis presents results from deterministic ray tracing simulations that replicate the environment of indoor channel sounding measurements taken previously by Spencer [2]. This data is used to estimate the parameters of the extended Saleh-Valanzuela model which stochastically describes the space-time clustering structure observed in measurements [6], [7]. Additionally, the information capacity for the MIMO channel depends upon the amount of information about the channel that is available to the communication system [8]. When the transmitter has full knowledge of the channel state, the information capacity is higher than when the transmitter operates blindly. In an effort to reap the benefits of informed transmitter operation, we present a reduced parameter feedback method that increases the information capacity closer to the case where the transmitter has full CSI.

1.1 Thesis Organization

Chapter 2 presents a tutorial on the topic of MIMO wireless channel modeling. It begins with the matrix representation of narrowband channel propagation and the assumptions involved. Then, the basic theory of channel capacity is presented using elementary results from information theory. This provides the framework for the capacity metrics used to evaluate the performance of the feedback methods in Chapter 5.

www.manaraa.com

Chapter 3 describes the ray tracing simulation software used in the experiments. The WISE (for **Wi**reless **S**ystem **E**ngineering) software package was developed by Lucent Technologies Wireless Research for simulating three dimensional wireless transmission environments [9]. It includes a graphical interface, a power density simulator, a three dimensional environment viewer, and a versatile ray tracing simulator. Here we describe the design of a simulation experiment using the WISE simulator to match the indoor channel impulse response measurements taken by Spencer [2].

Chapter 4 presents the results of the ray-tracing simulation experiment designed to replicate the SISO indoor channel measurements reported in [2]. Specifically, we describe the software processing performed on the ray tracing simulator output data and the methods used to estimate the parameters of the Space-Time Clustered channel model for comparison with the values reported from earlier measurements.

Chapters 5 and 6 investigate some methods of reduced parameter feedback in an effort to achieve near-optimal MIMO capacity. Chapter 5 draws from the previous discussion of the ray-based channel model to describe a method of estimating ray synthesis model parameters at the receiver and providing them as feedback to the transmitter. This allows the construction of a channel model which, although imperfect, can be used to shape the covariance of the transmitted symbols to increase the channel information capacity above that of the blind transmitter case and approach the maximum capacity available for a transmitter with full channel state information. The goal is to feed back less information than represented by the traditional entries of the channel matrix and obtain close to full CSI capacity. Performance results from Monte Carlo simulations show the conditions where significant benefit can be obtained from parameter feedback. Finally, the algorithm is applied to measured indoor MIMO channel data to evaluate its performance for non-synthetic channel realizations. Chapter 6 takes advantage of the symmetry and structure of the transmitted symbol covariance in search of even greater reductions to the feedback necessary to produce near-optimal channel capacity. This chapter describes two alternative methods for determinining the covariance feedback parameters: an LS

www.manaraa.com

approach, drawing on traditional techniques, and a MAXDET method that seeks to maximize the ergodic capacity determinant directly. The covariance methods are demonstrated by simulation and results are presented along with processing the same indoor channel data for comparison with the Ray Model feedback method.

1.2 Problem Statement

The goal of this thesis is to investigate the following problems:

- Use ray tracing tools to simulate the measurement conditions used by Spencer [2] and determine the quality of the predictions by comparison to results from the measurements. Specifically, determine the correspondence of predicted channels with the multipath measurements and estimated parameters found for the Saleh-Valanzeula clustered model extended to include angle of departure/ arrival information (SVA model).

- Identify the most significant elements of the ray tracing simulation which determine the quality of the predicted channels.

- Investigate the use of the ray synthesis channel model as a means to provide channel state information (CSI) from the receiver to the transmitter for improved information capacity. Specifically, identify methods of determining the ray model parameters which most efficiently increase the information capacity considering the amount of resources required to communicate the feedback information.

- Investigate the use of covariance information as an alternative to the ray synthesis model for improving the channel information capacity with a small quantity of feedback information.

www.manaraa.com

1.3 Literature Review

The flood of research interest in MIMO communication systems has been triggered by a number of early publications outlining the theoretical capacity of multi-antenna systems that grows linearly with the number of array elements. Among the most frequently cited publications are Teletar [3] and Foschini and Gans [4]. To organize the literature citations in this review, the references have been separated into the following categories: MIMO Channel Modeling, Ray Tracing, Channel Sounding & Measurement, and MIMO Feedback & Channel Capacity.

MIMO Channel Modeling

A variety of channel modeling approaches have been suggested for representing MIMO communication channels. Zwick, et al [10] present a complex indoor / urban MIMO channel model that has many features in common with the SVA model used in this thesis. A deterministic ray tracing approach is also used to provide typical values for their model parameters. Ge, et al [11] use the same "sum of rays" constructive channel model in discussing the statistical properties of MIMO channel capacity with Monte Carlo simulation results. Another frequently used MIMO channel model is the "2 bounce model" as discussed by Gespert, et al [12] that assumes a single reflection in the neighborhood of both the transmitter and receiver with a direct path connecting the two. The "2 bounce model" has also been extended by Povey and Levy [13] to allow independent variation of the transmit and receive angles based on scatterers in the proximity of the transmitter and receiver. Liu, et al [14] create a virtual channel model to allow analysis of multipath richness and capacity gains under "more realistic" assumptions. They observe that the number of multipath components must grow quadratically with the number of antennas in order to achieve the linear increase in capacity.

www.manaraa.com

Ray Tracing

There are numerous publications that describe ray tracing techniques similar to those used in this research. Typically ray tracing is chosen to provide predictive information about channels which are expensive or difficult to measure. Ray tracing calculations can be generated using several different methodologies, including uniform theory of diffraction [15], ray launching [16] and [17], method of images [18] and Full Wave Finite Difference Time Domain Simulation [19]. Ray tracing techniques have been applied to many different communication problems such as urban microcells [20], vehicle interiors [21], and global positioning systems [22].

Focusing on research that relates more closely to this thesis, Tila, et al [23] use site-specific indoor ray tracing to predict the SNR and information capacity for a MIMO system at 5 GHz. They present the interesting result that capacity is significantly improved by distributing transmitter antennas to the corners of a single room rather than concentrating them in a traditional uniform linear array (ULA). An example of researchers comparing ray tracing predictions with measurements can be found in the outdoor channels analyzed by Rautiainen, et al [24]. The work of Browne, et al [19] is significant because it provides support for the 2-D planar model assumptions used in our simulations and also presents similar observations of time/angle clustering and time/power profiles which are linear in logarithmic space with high degree of scatter. Their conclusions also state that the description of the building geometry and structure is more important than description of the material properties with the finer structural description being key to accurately predictions of the clustering behavior. Additional support for a 2-D planar geometry model can be found in the work of Medbo and Berg [25] where it was reported that the contributions of the strongest 90% of scatterers in an office environment were captured within a cone of less than 20° of elevation centered in the horizontal plane.

This paragraph continues the description of ray tracing literature. Zhang and Huang [26] investigated the effects of changes in material properties while the building

www.manaraa.com

geometry was kept constant. Burr [18] uses ray tracing prediction of indoor MIMO channels to analyze information capacity. This work also argues that the 2-D planar model assumption is reasonable, and the results are displayed using Complementary CDF's of capacity. Pena, et al [27] compared ray tracing predictions of wall behavior for two common material types (brick and metal reinforced concrete) with measurements of reflection/transmission. They concluded that uniform modeling for brick walls is well-justified, but that the presence of metal reinforcing materials produce geometry specific deviations from uniform behavior. This justifies the addition of metal reinforcing materials to the geometry model used for ray tracing simulations in this research. Kim, et al [28] compared ray tracing simulations with measurements at 5 GHz in a single large room. They found that ray tracing simulation was more effective in predicting arrival/departure geometry than power characteristics. This agrees with our current observations. Finally, Passerini [29] suggests a methodology for validating ray tracing results.

The *WiSE* ray tracing software package has been used by numerous other researchers to investigate the behavior of wireless systems. There are several publications that describe the software package [9] [30]. Chuah, et al [31] (and identically in [32]) used *WiSE* to simulate narrowband MIMO channels to investigate information capacity versus the number of antenna elements. They observed that the improvement in waterfilling capacity over uniform power allocation was most significant at low SNR, as will be similarly shown in our results. They also noted that the asymptotic channel capacity limits are overestimated because they ignore limitations which result from correlation between array elements. A similar statement in this regard was made by Goldsmith, et al [8]. Ling, et al [33] used *WiSE* to demonstrate the degradation of capacity due to keyhole degenerate channels (which have zero correlation between entries but only 1 degree of freedom) can result from a diffracting wedge under realistic assumptions. Finally, Chua, et al [34] give example *WiSE* parameter settings for indoor and outdoor scenarios. They presented results using the Complementary CDF (CCDF) of capacity and used 95% Outage Capacity. Their findings

www.manaraa.com

indicate that there are more realized capacity gains when the receiver is located closer to the transmitter than when farther away. Also, they showed that capacity gains result when antenna spacings are larger than one wavelength (their simulation used 3 wavelength spacing) because of reductions in the inter-element correlation even when a strong line of sight signal is present.

Channel Sounding & Measurement

Early channel sounding experiments used a Single-input - Single Output (SISO) architecture to keep the hardware systems simple. The ray tracing results were designed for comparison with measurements taken by a SISO measurement system. Some examples can be found in the work of Guillouard, et al (60 GHz indoor) [35] and Courivaud, et al (2 GHz indoor) [36]. As interest in MIMO grew, simple MIMO channel sounding systems began producing results such as Stoytchev, et al [37] (used a single transmitter with a single moving receiver to construct 4x4 MIMO measurements from 1.8 to 3.4 GHz), Batariere, et al [38] (used 2x2 OFDM system in suburban outdoor setting), Stridh, et al [39] (used SISO superposition to construct MIMO channels at 5.8 GHz), Erceg, et al [40] (used 2x2 swept frequency at 2.48 GHz with post-processing in outdoor locations) and Kuroda, et al [41] (used Frequency Division Multiplexing for rotating 2x2 system at 5.8 GHz).

With additional systems development, more recent channel measurements have been taken with larger array sizes and more complex configurations. The 10x10 measurements used in Chapter 5 and 6 were obtained from a simultaneously sampled system in this class. References describing this system can be found in [42] [43] and [44]. Martin, et al [45] presented results from a 4x4 real-time channel sounder that transmitted orthogonal Walsh codes and estimated the channel in real-time with a sample time of 300 microseconds at 1.9 GHz. Their data provided results on ergodic capacity and inter-element correlation. Another 4x4 system reported by Kermoal, et al [46] used switched elements and a fixed velocity trolley on a linear track to probe

www.manaraa.com

indoor channels at 2.05 GHz with a sample time of 20 milliseconds. Their analysis included spatial correlation, doppler power spectrum and the eigenstructure.

This paragraph continues the description of recent channel measurement literature. A larger system described by McNamara, et al [47] collected indoor 8x8 channel data using multiplexed arrays at both endpoints with a channel sample time of 1.63 milliseconds at 5.2 GHz. They showed time evolution of Spatial Average SNR and capacity with noticeable differences between Line of Sight (LOS) and Non-Line of Sight (NLOS) channels. The NLOS channels demonstrated higher capacity even though the average SNR increases in LOS situations. This reflects the changes in the richness of the scattering and the degree of correlation between elements. A large, real-time system is discussed by Hampicke, et al [48] that multiplexes 8x8 arrays to gather the time-dependent frequency response using multi-frequency excitation at 5.2 GHz. They further processed their results to estimate the complex path gain, time difference of arrival (TDOA), directions of departure and arrival (DOD, DOA in both azimuth and elevation) and doppler shift of multipath components. They set forth Capacity CCDF's and time-evolution of channel eigenvalues versus array rotation angle. Earlier results are presented from this same system by Richter, et al [49]. Steinbauer, et al [50] used data taken with a similar system with a virtual 16x8 MIMO channel at 5.2 GHz. Their analysis included power-delay profiles, DOD and DOA analysis with correlation to actual scatters, angular power spectral density, and multipath component analysis.

MIMO Feedback & Channel Capacity

Goldsmith, et al [8] provide an excellent overview of the MIMO Channel Capacity problem along with suggestions for investigation into unsolved problems. They describe three levels of channel feedback: CSI, instantaneous channel state information (elements of H), short-term CDI, statistical distribution of the channel coefficients with non-zero mean (typically mean and covariance of a jointly Gaussian distribution), and long-term CDI, statistical distribution of channel coefficients that

www.manaraa.com

are assumed zero-mean and uncorrelated. In any given scenario, the level of feedback may be different at the receiver than at the transmitter. The research in this thesis focuses on the CSI scenario with attempts to communicate instantaneous channel gain terms to the transmitter once they have been identified by the receiver. The observation of clustered multipath arrivals composing the MIMO channel relates well with the short-term (non-zero mean) observation situation. For some tests, Monte Carlo simulations were used where the channel gain terms were independent and identically distributed which corresponds to the long-term assumption about the channel structure.

Skoglund and Jongren [51] present a generalized framework to describe MIMO systems where feedback information is employed. They observe that the initial quantity of feedback produces the largest gains with the marginal returns decreasing as more feedback information is provided. This is a consistent feature in the observations made in this research. Another practical issue for feedback systems is well-illustrated in the work of Sutivong, et al [52] who observe (for the SISO channel case) that too much feedback information precludes the transmission of user data over the channel. Medles, et al [53] present capacity simulations where the transmitter has varying levels of information about the channel state. They conclude that the channel covariance information is sufficient to produce near-optimal capacity and discount the value of additonal feedback information. This could be used as motivation for the covariance feedback methods presented in Chapter 6. Bhashyam, et al [54] demonstrate two methods for the Multiple Input - Single Output (MISO) channel: power control and beamsteering. Their results are presented in terms of outage performance rather than information capacity. They also observe that the first few bits of feedback yield the largest improvements. Another MISO channel feedback example can be found in the work of Visotsky and Madhow [55] who utilize statistical distribution information and present suggestions for using it effectively. Jafar and Goldsmith [56] outline necessary and sufficient conditions for the optimality of beamforming feedback in MISO Channels, and some theoretical proofs on the topic of covariance feedback for MISO

www.manaraa.com

and MIMO channels were presented by Jafar, et al [57]. Kang and Alouini [58] use moment generating functions to identify the mean and variance of MIMO capacity as a Gaussian random variable for the waterfilling and beamforming scenarios. Oyman, et al [59] analyze the effect of spatial correlation on the capacity of MIMO systems. They look at the tradeoff between multiplexing and diversity gains in correlated MIMO channels, and determine the capacity maximizing number of transmit and receive antennas as a function of SNR region where the total number of antenna elements is fixed.

1.4 Contributions

This research substantiates the observations of time and angle of arrival clustering reported by [6] and [7]. The deterministic ray tracing simulation results clearly show similar groupings of ray arrivals predicted from the building geometry description model, and the statistical distribution of random parameters resulting from predicted data agree with previous observations. The parameter estimates derived from predictive simulation that describe the angular distribution and arrival frequencies of clusters and discrete rays are consistent with the values from measurements. The behavior of the ray tracing suggests strongly that the description of the bulk materials in the building (such as strict wall structure) are less important to the statistical consistency of the predictions than description of reflective scatters (such as door and window frames, rebar, and other metallic features).

In addition, we demonstrate that estimates of ray parameters made from the channel transfer matrix can provide a compressed representation of channel state information which is sufficiently accurate to allow more than 90% of the Full CSI information capacity to be realized by a transmitter shaping the symbol covariance using parameter feedback. This approach offers the most significant gains in low SNR environments where the differential between Fully Informed Transmitter capacity and Blind Transmitter capacity is the largest and the dimension of the signal subspaces used for estimation is small compared to the number of array elements. Several

www.manaraa.com

estimation algorithms are compared, including a 2-D *unitary* ESPRIT estimator that determines the transmit and receive angles jointly with their pairwise correspondence. The parameter feedback algorithm is applied to channels measured with the 2.45 GHz MIMO measurement platform developed in [42].

Finally, we present an alternative method of providing channel state information in terms of the covariance of the received symbols. We show that the symmetric, positive-semidefinite structure of the received symbol covariance can reduce the feedback information required. Two methods of determining the covariance feedback information are presented: a traditional least-squares fitting approach and a direct capacity determinant maximization approach. Simulation results provide performance comparisons for small array sizes (3,4 and 5 elements) which show that significant gains can be realized with a small amount of feedback, especially at low SNR values, but that the amount of improvement offered by additional feedback terms decreases as more feedback us supplied. The covariance feedback methods are applied to the same MIMO measurement data to give comparisons with the ray model feedback method. They suggest that the covariance feedback methods are computationally burdensome for large array sizes and typically result in less attractive perfomance than that obtained using ray model feedback.

www.manaraa.com

Chapter 2

MIMO Tutorial

This chapter presents a brief introduction to some important fundamental principles relevant to MIMO indoor wireless channel modeling. Each section presents one of the following topics: matrix representation of MIMO channel propagation, narrowband versus wideband channels, common fading models, theoretical information capacity of a MIMO channel, and basic array processing. These topics contributed to my research, and it is hoped that they will prove useful to those who pursue similar research in the future.

2.1 MIMO Channel Propagation Model

The flow of signals from a transmit antenna array through some arbitrary channel to a receiver antenna array is typically modeled as a multiple input-multiple output (MIMO) linear system. If some general system has T transmit antennas and R receive antennas, the pairwise impulse response $h_{i,j}[n]$ describes the relationship between the signal sent from the jth transmitter, $s_j[n]$, and the signal observed at the ith receiver, $x_i[n]$, as a convolution

$$x_i[n] = \sum_{k=0}^{\infty} h_{i,j}[k]\, s_j[n-k] \qquad i \in \{1, 2, \ldots, R\},\ j \in \{1, 2, \ldots, T\}\,. \tag{2.1}$$

Quite often, the MIMO channel model is simplified under the assumption of a 'narrowband' channel where all but the first tap of all pairwise transfer functions are assumed to be zero:

$$\text{(Narrowband Assumption)} \quad \longleftrightarrow \quad h_{i,j}[n] = 0 \quad \forall\, n \neq 0\,. \tag{2.2}$$

www.manaraa.com

Physically, this condition arises when the frequency band of interest is sufficiently restricted so that even if the frequency response is highly variable (as in a frequency selective fading scenario), the segment of the channel's frequency response over the narrow band of interest is adequately modeled as being flat - having constant magnitude and phase. The narrowband channel can also be interpreted as a scenario where all of the significant multipaths are sufficiently coincident in time that all of the arrivals can be combined into a single non-zero tap in all of the pairwise channel impulse responses. As a result, the signal at the ith receiver due to the broadcast of s_j from the jth transmitter is

$$x_{i,j}[n] = h_{i,j} \cdot s_j[n], \tag{2.3}$$

where $h_{i,j}$ is a complex scalar. If the model needs to reflect the frequency selective behavior of the channel, $h_{i,j}$ can be replaced with $h_{i,j}[n]$. Using the principle of superposition, the observed signal at the output of the ith receive antenna is the sum of the constituent signals resulting from all T transmitters:

$$x_i[n] = \sum_{j=1}^{T} x_{i,j}[n] = \sum_{j=1}^{T} h_{i,j} \cdot s_j[n]. \tag{2.4}$$

Equation 2.4 can be conveniently expressed in matrix notation by letting each of the x_i's reside in a column vector, $\mathbf{x}[n] = \begin{bmatrix} x_1[n] & x_2[n] & \cdots & x_R[n] \end{bmatrix}^T$ and forming the matrix product

$$\mathbf{x}[n] = \begin{bmatrix} h_{1,1} & h_{1,2} & \cdots & h_{1,T} \\ h_{2,1} & h_{2,2} & \cdots & h_{2,T} \\ \vdots & \vdots & \vdots & \vdots \\ h_{R,1} & h_{R,2} & \cdots & h_{R,T} \end{bmatrix} \begin{bmatrix} s_1[n] \\ s_2[n] \\ \vdots \\ s_T[n] \end{bmatrix} = H\,\mathbf{s}. \tag{2.5}$$

Notice that multiple time samples of $\mathbf{x}$ may be formed by stacking them in columns as in

$$\begin{bmatrix} \mathbf{x}[1] & \mathbf{x}[2] & \cdots & \mathbf{x}[n] \end{bmatrix} = H \begin{bmatrix} \mathbf{s}[1] & \mathbf{s}[2] & \cdots & \mathbf{s}[n] \end{bmatrix}. \tag{2.6}$$

www.manaraa.com

2.2 Information Capacity of AWGN MIMO Channel [1]

As MIMO channels promise significant increases in the rate of data transmission, we desire to quantify the theoretically maximum amount of information that can be communicated by way of any particular MIMO channel. This result from information theory does not provide any guidance in the construction of the signaling and coding methods needed to achieve the maximum capacity. It simply states an upper bound on the information capacity that any imaginable transmission scheme may achieve.

As a starting point for this development, we take the standard narrowband MIMO model for a system with T transmit elements and R receive elements from Section 2.1:

$$\mathbf{x} = H\mathbf{s} + \mathbf{n}\,, \tag{2.7}$$

where $\mathbf{x} \in \mathbb{C}^{R\times 1}$ is the received signal vector, $H \in \mathbb{C}^{R\times T}$ is the MIMO channel transfer matrix, $\mathbf{s} \in \mathbb{C}^{T\times 1}$ is the transmitted symbol vector, and $\mathbf{n} \in \mathbb{C}^{R\times 1}$ is the noise vector. We assume that the noise, $\mathbf{n}$, is distributed as a Circular Complex Gaussian, or Complex Normal, with zero mean and unit, white covariance:

$$\mathbf{n} \sim \mathcal{CN}(\mathbf{0}, I_R)\,.$$

Additionally, we assume that the channel matrix, H, is known and that the total transmit power is constrained to be no greater than ρ:

$$\mathrm{E}\left\{\sum_{i=1}^{T} |s_i|^2\right\} \;=\; \mathrm{E}\{\mathbf{s}^H\mathbf{s}\} \;=\; \mathrm{tr}\left(\mathrm{E}\{\mathbf{s}\,\mathbf{s}^H\}\right) \;\le\; \rho\,, \tag{2.8}$$

where $\mathrm{E}\{\,\cdot\,\}$ is the statistical expectation operator and $\mathrm{tr}(\,\cdot\,)$ is the matrix trace operator. Define Q to equal $\mathrm{E}\{\mathbf{s}\,\mathbf{s}^H\}$, the covariance of the transmitted symbols. The power constraint can be expressed in terms of Q as

$$\mathrm{tr}(\,Q\,) \;=\; \sum_{i=1}^{T} Q_{ii} \;\le\; \rho\,. \tag{2.9}$$

www.manaraa.com

To achieve maximum information capacity, $\mathbf{s}$ should be chosen to maximize the *mutual information* between $\mathbf{x}$ and $\mathbf{s}$:

$$\mathcal{I}(\mathbf{x},\mathbf{s}) \;=\; \mathcal{H}(\mathbf{x}) - \mathcal{H}(\mathbf{x}\,|\,\mathbf{s}) \;=\; \mathcal{H}(\mathbf{x}) - \mathcal{H}(\mathbf{n})\,. \tag{2.10}$$

The quantity $\mathcal{H}(\mathbf{z})$ is the *entropy* of $\mathbf{z}$ defined as:

$$\mathcal{H}(\mathbf{z}) \;=\; \mathrm{E}\{-\log f(z)\}\,, \tag{2.11}$$

where $f(\mathbf{z})$ is the pdf of $\mathbf{z}$. Notice that since $\mathcal{H}(\mathbf{n})$ does not depend on $\mathbf{s}$, maximizing $\mathcal{I}(\mathbf{x},\mathbf{s})$ is equivalent to maximizing $\mathcal{H}(\mathbf{x})$.

From distribution theory, it is known that the complex distribution of highest entropy is the circular complex Gaussian (CCG) [60]. We will use the following two facts to construct $\mathbf{x}$ as a CCG random variable:

- If $\mathbf{x},\mathbf{y} \in \mathbb{C}^{N\times 1}$ are uncorrelated and distributed as CCG according to $\mathbf{x} \sim \mathcal{CN}(\mathbf{m}_x, R_x)$ and $\mathbf{y} \sim \mathcal{CN}(\mathbf{m}_y, R_y)$, the sum of $\mathbf{x}$ and $\mathbf{y}$ is also distributed as CCG according to $\mathbf{x}+\mathbf{y} \sim \mathcal{CN}(\mathbf{m}_x+\mathbf{m}_y, R_x+R_y)$.

- If $\mathbf{x} \in \mathbb{C}^{N\times 1}$ is distributed as CCG according to $\mathbf{x} \sim \mathcal{CN}(\mathbf{m}_x, R_x)$ and the matrix $A^H \in \mathbb{C}^{N\times N}$ is non-singular, the linear transform $\mathbf{y} = A^H\mathbf{x}$ is also CCG according to $\mathbf{y} \sim \mathcal{CN}(A^H\mathbf{m}_x, A^H R_x A)$. (Demonstrated for the real case in [61] on p. 59).

If $\mathbf{s}$ is chosen to be CCG, then $H\mathbf{s}$ will also be CCG as well as the sum $\mathbf{x} = H\mathbf{s}+\mathbf{n}$. This results in an $\mathbf{x}$ of maximum entropy. Therefore, to achieve maximum capacity, $\mathbf{s}$ must be chosen to be CCG distributed. Additionally, the covariance of $\mathbf{x}$ can be expressed in terms of $Q = \mathrm{cov}(\mathbf{s})$ as

$$\mathrm{cov}(\mathbf{x}) = \mathrm{cov}(H\mathbf{s}) + \mathrm{cov}(\mathbf{n}) = HQH^H + I_R\,. \tag{2.12}$$

www.manaraa.com

2.2.1 Entropy of a Circular Complex Gaussian Random Vector

Here we determine the entropy of a CCG random vector. Let $\mathbf{z} \in \mathbb{C}^{N\times 1}$ be a CCG random vector with mean $\mathbf{m}$ and covariance R as in $\mathbf{z} \sim \mathcal{CN}(\mathbf{m}, R)$.

$$\begin{aligned}
\mathcal{H}(\,\mathbf{s}) &= \mathrm{E}\{-\log f(\mathbf{z})\} = \mathrm{E}\left\{-\log\left(\det(\pi R)^{-1}\mathrm{e}^{(\mathbf{z}-\mathbf{m})^H R^{-1}(\mathbf{z}-\mathbf{m})}\right)\right\} \\
&= \log(\,\det(\pi R)) + \log(\mathrm{e})\,\mathrm{E}\left\{(\mathbf{z}-\mathbf{m})^H R^{-1}(\mathbf{z}-\mathbf{m})\right\} \\
&= \log(\,\det(\pi R)) + \log(\mathrm{e})\,\mathrm{tr}(\,\underbrace{R^{-1}\mathrm{E}\left\{(\mathbf{z}-\mathbf{m})(\mathbf{z}-\mathbf{m})^H\right\}}_{=I_N}\,) \\
&= \log(\,\det(\pi R)) + \log(\mathrm{e})\,\mathrm{tr}(\,I_N) \\
&= \log(\,\det(\pi R)) + \log(\,\mathrm{e}^N) \\
&= \log(\,\det(\pi R)) + \log(\,\det(\mathrm{e}\,I_N)) \\
&= \log(\,\det(\pi\,\mathrm{e}\,R)) \qquad (2.13)
\end{aligned}$$

2.2.2 Waterfilling Solution for Maximum Capacity

Using the result from the previous section, we now turn our efforts to determining an expression for the value of maximum capacity given that we know that all of the vectors $\mathbf{x}$,$\mathbf{s}$, and $\mathbf{n}$ are CCG distributed. Substituting Equation 2.13 into Equation 2.2 describing mutual information, we obtain the following:

$$\begin{aligned}
\mathcal{I}\,(\mathbf{x},\mathbf{s}) &= \mathcal{H}(\,\mathbf{x}) - \mathcal{H}(\,\mathbf{n}) = \log(\,\det(\pi\,\mathrm{e}\;\mathrm{cov}(\mathbf{x})) - \log(\,\det((\pi\,\mathrm{e}\;\mathrm{cov}(\mathbf{n})) \\
&= \log(\,\det(\pi\,\mathrm{e}\,(I_R + HQH^H))) - \log(\,\det((\pi\,\mathrm{e}\,I_R) \\
&= \log(\,\det(I_R + HQH^H)) + \log(\,\det(\pi\,\mathrm{e}\,I_R)) - \log(\,\det((\pi\,\mathrm{e}\,I_R) \\
&= \log(\,\det(I_R + HQH^H)) \\
&= \log(\,\det(I_T + Q\,H^H H)) \\
&= \log(\,\det(I_T + Q\,U\Lambda\,U^H)) \qquad (\text{SVD of } H^H H = U\Lambda\,U^H) \\
&= \log(\,\det(I_T + U^H Q\,U\Lambda)) \qquad (\tilde{Q} \equiv U^H Q\,U) \\
&= \log(\,\det(I_T + \tilde{Q}\,\Lambda)) \;\leq\; \sum_{i=1}^{T} \log(1 + \tilde{Q}_{ii}\,\lambda_i)\,. \qquad (2.14)
\end{aligned}$$

www.manaraa.com

The inequality in the last step arises from the relation $\det(A) \leq \prod_{i=1}^{N} A_{ii}$ for $A \in \mathbb{C}^{N \times N}$ where the upper bound is achieved when A is diagonal.

Using this result, the solution for maximum capacity, C, can be expressed as a constrained maximization:

$$C = \max_{\substack{\tilde{Q}_{ii} \\ i=1,\ldots,T}} \sum_{i=1}^{T} \log(1 + \tilde{Q}_{ii}\,\lambda_i) \quad \text{such that} \quad \sum_{i=1}^{T} \tilde{Q}_{ii} = \rho\,. \tag{2.15}$$

Writing this as a Lagrange multiplier problem yields:

$$V = \sum_{i=1}^{T} \log(1 + \tilde{Q}_{ii}\,\lambda_i) \;+\; \gamma \left(\sum_{i=1}^{T} \tilde{Q}_{ii} - \rho \right) . \tag{2.16}$$

Setting all partial derivatives with respect to $\tilde{Q}_{ii}$ to zero, we obtain

$$\begin{aligned} \frac{\partial V}{\partial \tilde{Q}_{ii}} \;&=\; \frac{\lambda_i}{1 + \tilde{Q}_{ii}\,\lambda_i} \;+\; \gamma \;=\; 0 \\ \Rightarrow \quad \lambda_i + \gamma\,(1 + \tilde{Q}_{ii}\,\lambda_i) \;&=\; 0 \\ \Rightarrow \quad \tilde{Q}_{ii} \;&=\; -\tfrac{1}{\gamma} \;-\; \lambda_i^{-1}\,. \end{aligned} \tag{2.17}$$

If we define μ as a constant (independent of i) that is chosen so that $\sum_{i=1}^{T} \tilde{Q}_{ii} = \rho$, Equation 2.17 becomes

$$\tilde{Q}_{ii} = \mu \;-\; \lambda_i^{-1}\,. \tag{2.18}$$

Because $\tilde{Q}$ is a covariance matrix ($\tilde{Q} = \mathrm{cov}(U^H \mathbf{x})$), it is positive semi-definite and all of its eigenvalues must be non-negative, and because $\tilde{Q}$ is diagonal, its eigenvalues are equal to its diagonal entries (e.g. $\mathrm{eig}(\tilde{Q}) = \tilde{Q}_{ii}$ for $i = 1, \ldots, T$). So, it is not reasonable for any of the $\tilde{Q}_{ii}$'s to be negative. For this reason, we introduce the $(\cdot)^+$ operator defined as

$$(\,z\,)^+ = max\{\,0, z\,\} \;\text{ for } z \in \mathbb{R}\,. \tag{2.19}$$

The final expression for maximum capacity of a MIMO channel H is

$$C = \log(\det(I_T + \tilde{Q}\,\Lambda)) = \sum_{i=1}^{T} \log(1 + \tilde{Q}_{ii}\,\lambda_i) \;\text{ where } \tilde{Q}_{ii} = (\,\mu \;-\; \lambda_i^{-1})^+\,. \tag{2.20}$$

www.manaraa.com

Notice that because the eigenvalues of $H^H H$ are positive ($\lambda_i = \sigma_i^2$ where the σ_i's are the singular values of H) and monotonically non-decreasing (e.g. $\lambda_1 \geq \lambda_2 \geq \cdots \geq \lambda_T$), the quantities λ_i^{-1} are monotonically non-increasing ($\lambda_1^{-1} \leq \lambda_2^{-1} \leq \cdots \leq \lambda_T^{-1}$). As a result, the values of $\tilde{Q}_{ii} = \mu - \lambda_i^{-1}$ begin positive at $i = 1$ and decrease to potentially become less than zero for some $k+1 < T$. The effect of the $(\cdot)^+$ operator is to force the $\tilde{Q}_{ii}$'s to zero for all $k+1 \leq i \leq T$. This allows k to equal the number of *non-zero entries* in $\tilde{Q}$. Equation 2.20 is referred to as the *waterfilling solution* for reasons that will be discussed in the following section.

2.2.3 Interpretation of the Waterfilling Solution for Channel Capacity

In order for the transmitter to optimally shape the covariance of its transmission, it must have knowledge of the eigenvectors of $H^H H$ (equivalent to the right singular vectors of H) and their associated eigenvalues, λ_i. We can think of the action of the waterfilling equation as selecting out the dominant eigenchannels that compose the range of the reciprocal channel, H^H, and preferentially distributing its constrained amount of power into the eigenchannels with the largest gains. This results in the covariance of the signals arriving at the receiver, before noise addition, being uncorrelated and optimally weighted (HQH^H is diagonal with entries equal to $\lambda_i \tilde{Q}_{ii}$). From the definition $\tilde{Q} = U^H Q U$, where $U = [\, u_1 \; u_2 \; \cdots \; u_T \,]$ are the eigenvectors of $H^H H$, we can see that $Q = U \tilde{Q} U^H$. This can be interpreted as a transmit beamformer that applies $U\,\tilde{Q}^{1/2}$ to initially white, unit covariance symbols, $\tilde{\mathbf{s}}$, as in:

$$\mathbf{s} = U\,\tilde{Q}^{1/2}\,\tilde{\mathbf{s}} \;\text{ where }\; \mathrm{cov}(\tilde{\mathbf{s}}) = I_T\,. \tag{2.21}$$

The resulting transmit symbols have covariance equal to the following weighted sum of outer products, where k is the number of eigenchannels with non-zero allocated transmit power:

$$Q = \sum_{i=1}^{T} \tilde{Q}_{ii}\,\mathbf{u_i}\,\mathbf{u_i}^H = \sum_{i=1}^{k} \tilde{Q}_{ii}\,\mathbf{u_i}\,\mathbf{u_i}^H\,. \tag{2.22}$$

www.manaraa.com

It is interesting to note that this defines the transmit symbol covariance with the same eigenvectors as $H^H H$ only replacing the eigenvalues $\{\lambda_i\}$ with the weights from the waterfilling equation, $\{\tilde{Q}_{ii}\}$.

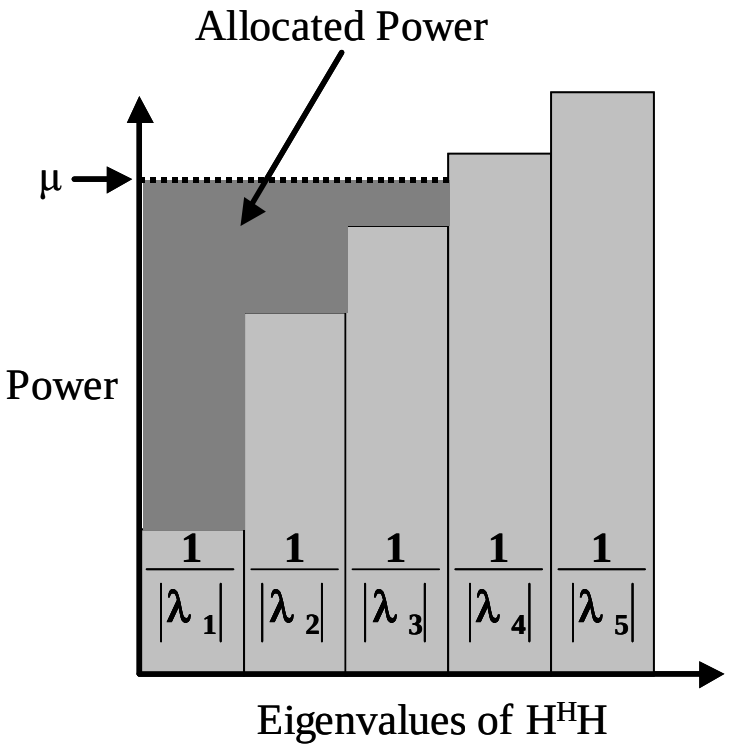

Figure 2.1: Graphical representation of waterfilling eigenchannels.

The name *waterfilling solution* can best be understood by graphing the power allocation to the eigenchannels as in Figure 2.1. If each eigenchannel has unit width, we can represent λ_i^{-1} as a "pseudo noise floor" for each channel which increases from left to right. If the power available for transmission is symbolized by a fixed amount of water that we pour in from above, we can see that it fills the eigenchannel with lowest floor first and then distributes to adjacent channels until it reaches a constant level, μ, across all of the powered channels. From this picture, we can see that the $(\cdot)^+$

www.manaraa.com

operator in Equation 2.20 serves to prevent the allocation of "negative" quantities of power into unused eigenchannels. The capacity is the log of the combined product of the eigenchannel gains and the allocated channel power with a 1 added to each term for the contribution of the noise:

$$C = \log\left(\prod_{i=1}^{T}(\lambda_i \tilde{Q}_{ii} + 1)\right) = \log\left(\prod_{i=1}^{k}(\lambda_i \tilde{Q}_{ii} + 1)\right) . \tag{2.23}$$

The base of the logarithm determines the units of the capacity result. Typically $\log_2$ is used, resulting in Capacity in units of Bits/sec/Hertz.

Another interesting feature of the waterfilling solution is its similarity to the characteristic polynomial $p_A(\lambda)$ used to find the eigenvalues of a square matrix, A. From the standard eigenvector problem, $p_A(\lambda)$ is defined by

$$A\mathbf{x} = \lambda\mathbf{x} \quad \Rightarrow \quad (A - \lambda I) = 0$$

$$p_A(\lambda) \;=\; \det(A - \lambda I) \;=\; c_1\,\lambda^n + \ldots + c_n\,\lambda_1 + c_{n+1}\,. \tag{2.24}$$

Notice that the $\log(\det(I + \tilde{Q}\Lambda))$ from Equation 2.14 is simply the log of the characteristic polynomial of $\tilde{Q}\Lambda$ evaluated at $\lambda = -1$

$$C = \log(\,\det(I_T + \tilde{Q}\,\Lambda)) = \log\, p_{\,\tilde{Q}\Lambda}(\lambda)\,\Big|_{\lambda=-1}\,. \tag{2.25}$$

Because the matrices HQH^H and $\tilde{Q}\Lambda$ have the same eigenvalues, $p_{\,HQH^H}(\lambda)$ and $p_{\,\tilde{Q}\Lambda}(\lambda)$ are interchangeable. If we expand Equation 2.25 in terms of the coefficients of $p_{\,\tilde{Q}\Lambda}(\lambda)$ as in

$$C = \log\left((-1)^n\,c_1 + (-1)^{n-1}\,c_2 + \ldots + (-1)\,c_n + c_{n+1}\right)\,,$$

we can see that it is simply the log of the alternating plus-minus sum of the coefficients, $\{c_1\,\ldots, c_{n+1}\}$. To further simplify the calculation, we can use the fact that $\tilde{Q}_{ii}$ is zero for $i > k$ by substituting for $p_{\,\tilde{Q}\Lambda}(\lambda)$, the polynomial of reduced order, k, which has the *non-zero* eigenvalues of $\tilde{Q}\Lambda$ and HQH^H as its roots. A simple process for finding this reduced order characteristic polynomial starting with a set of eigenvalues, $\{\lambda_1, \lambda_2, \ldots, \lambda_k\}$, by expanding the product $(\lambda-\lambda_1)(\lambda-\lambda_2)\ldots(\lambda-\lambda_k)$ can be outlined in MATLAB notation as shown below (see [62]).

www.manaraa.com

```
z = [ λ1 λ1 ... λk ];
c = [ zeros(1,k) 1 ];
for loop = 1:k
   c(2:loop+1) = c(2:loop+1) - z(loop)*c(1:loop) ;
end
```

Finally, because we know that capacity is a non-negative quantity, we can simplify the selection of the sign of the leading coefficient by using absolute value so long as we take the terms in a consistent order from $c_1, \ldots, c_{n+1}$ or $c_{n+1}, \ldots, c_1$:

$$C = \log(\,|\, c_1 - c_2 + c_3 - \cdots c_{N+1} \,|\,) = \log(\,|\, c_{N+1} - c_N + c_{N-1} - \cdots c_1 \,|\,)\,. \quad (2.26)$$

This formulation is interesting because it demonstrates that capacity is solely dependent upon the eigenvalues of $H^H H$ and may provide a short-cut to calculating the capacity where the characteristic polynomial is known rather than the actual eigenvalues themselves.

2.2.4 Optimal Capacity for Blind Transmitter Case

If the transmitter does not have any knowledge of the eigenstructure of $H^H H$, it clearly cannot apply the optimal beamformer from the waterfilling solution to shape the covariance of its transmission. As a fallback position, let us assume that the channel transfer matrix, H, is random with i.i.d. (independent and identically distributed) elements which are CCG with zero mean and unit variance as in

$$H_{i,j} \sim \mathcal{CN}(0,1) \quad \Leftrightarrow \quad \mathrm{E}(\,H_{i,j}) = 0\;;\; \mathrm{E}(\,H^*_{i,j}\,H_{i,j}) = 1\,, \quad (2.27)$$

where a^* denotes the complex conjugate of a. The independence of the elements of H can be expressed as

$$\mathrm{E}\,(\,H^*_{i,j}\,H_{k,l}\,) = \begin{cases} 1 & : \quad (i,j) = (k,l) \\ 0 & : \quad \text{otherwise}\,. \end{cases} \quad (2.28)$$

www.manaraa.com

In this situation, the maximum capacity channel should maximize the mutual information between the joint random variables, $(\mathbf{x}, H)$ and the transmitted symbols, $\mathbf{s}$ as in

$$\begin{aligned} \mathcal{I}\left((\mathbf{x}, H)\right) &= \mathcal{I}\left(H, \mathbf{s}\right) + \mathcal{I}\left(\mathbf{x}, \mathbf{s} \,\middle|\, H\right) \\ &= \mathcal{I}\left(\mathbf{x}, \mathbf{s} \,\middle|\, H\right) \\ &= \mathrm{E}_H\left(\mathcal{I}\left(\mathbf{x}, \mathbf{s} \,\middle|\, H = \overline{H}\right)\right) . \end{aligned} \tag{2.29}$$

Thus, we want to maximize

$$V = \mathrm{E}_H\left(\log\det(I_R + HQH^H)\right) \tag{2.30}$$

subject to the maximum transmit power constraint, $\mathrm{tr}(Q) = \rho$. Let the singular value decomposition of Q be represented as $Q = UDU^H$ using the fact that Q is a covariance matrix and therefore equal to $A^H A$ for some $A \in \mathbb{C}^{T\times T}$. Substituting into the previous equation, we obtain

$$V = \mathrm{E}_H\left(\log\det\left(I_R + (HU)D(HU)^H\right)\right) . \tag{2.31}$$

It is helpful to notice at this point, that the matrix HU is distributed identically to H as demonstrated by

$$\text{mean:}\quad \mathrm{E}\left(\{HU\}_{i,j}\right) = \mathrm{E}\left(\sum_{k=1}^{R} H_{i,k}U_{k,j}\right) = \sum_{k=1}^{R} \underbrace{\mathrm{E}\left(H_{i,k}\right)}_{=0} U_{k,j} = 0$$

$$\begin{aligned} \text{variance:}\quad \mathrm{E}\left(\{HU\}^*_{i,j}\{HU\}_{i,j}\right) &= \mathrm{E}\left((\mathbf{h}_i^H\mathbf{u}_j)^*\,\mathbf{h}_i^H\mathbf{u}_j\right) = \mathrm{E}\left(\mathbf{u}_j^H\mathbf{h}_i\,\mathbf{h}_i^H\mathbf{u}_j\right) \\ &= \mathbf{u}_j^H\,\underbrace{\mathrm{E}\left(\mathbf{h}_i\,\mathbf{h}_i^H\right)}_{I}\mathbf{u}_j = 1 , \end{aligned} \tag{2.32}$$

where $\mathbf{h}_i^H$ is the i^{th} row of H and $\mathbf{u}_j$ is the j^{th} column of U. This similarity allows us to replace HU in Equation 2.31 with H resulting in

$$V = \mathrm{E}_H\left(\log\det\left(I_R + HDH^H\right)\right) . \tag{2.33}$$

www.manaraa.com

By direct comparison with Equation 2.30, we can see that Q must be identical to D and is therefore diagonal. Our next task is to inspect the structure of the expectation of the quadratic term HQH^H:

$$\mathrm{E}\left(\{HQH^H\}_{i,j}\right) = \mathrm{E}\left(\sum_{k=1}^{T} H_{i,k}\, Q_{kk} H^*_{j,k}\right) . \tag{2.34}$$

From the independence of the elements of H shown in Equation 2.28, we can see that the expectation will be zero for all terms where $i \neq j$, leaving us with a diagonal matrix with the Q_{kk}'s on the diagonal:

$$\mathrm{E}\,(\,HQH^H\,) = \mathrm{diag}\{\,Q_{11}\,,\,\cdots\,,Q_{TT}\,\} = Q\,. \tag{2.35}$$

Using the fact that the determinant of a diagonal matrix is the product of the diagonal elements, we can write the equation for mutual information including the power constraint as

$$V = \sum_{i=1}^{T} \log\left(1 + Q_{ii}\right) \;+\; \gamma\left(\sum_{i=1}^{T} Q_{ii} - \rho\right) . \tag{2.36}$$

Taking the partial derivative of V with respect to Q_{ii} and setting to zero, we can solve for Q_{ii} as

$$\begin{aligned} \frac{\partial V}{\partial Q_{ii}} \;&=\; \frac{1}{1+Q_{ii}} \;+\; \gamma \;=\; 0 \\ \Rightarrow \quad Q_{ii} \;&=\; -\tfrac{1}{\gamma} \;-\; 1\,. \end{aligned} \tag{2.37}$$

The most important fact to be gained from this is that the Q_{ii}'s are equal for all $i \in \{1,\ldots,T\}$. Therefore, without solving explicitly for γ, we can conclude from the power constraint that the optimal covariance for transmitted symbols is

$$Q_{ii} = \frac{\rho}{T} \quad \Leftrightarrow \quad Q = \frac{\rho}{T}\, I\,. \tag{2.38}$$

It is interesting to note that when the transmitter does not have the benefit of knowing the eigenstructure of the channel, the optimal allocation of power is to distribute an equal quantity into all eigenchannels under the assumption of independent Rayleigh fading. The blind transmitter capacity can also represent a lower bound

www.manaraa.com

on the capacity achievable if the transmitter has only partial knowledge of the structure of the channel. Some interesting limiting cases for the blind transmitter MIMO channel are:

$$\begin{aligned} &\text{as } R \to \infty\,, \quad C \to T \log\left(1+\rho\right) \\ &\text{as } T \to \infty\,, \quad C \to R \log\left(1+\rho\right). \end{aligned} \tag{2.39}$$

These relationships are significant because they indicate that the capacity of the channel increases linearly with $\min\{T, R\}$.

www.manaraa.com

Chapter 3

Ray Tracing Simulation of Indoor Wireless Channels

3.1 Introduction

We recreated Quentin Spencer's indoor wireless channel impulse response measurements taken in the Clyde Engineering Building [6] using ray tracing simulation software. This provides verification of earlier results and demonstrates the utility of ray tracing as a means of predicting the influence of an indoor propagation environment in a system design scenario. In order to do so, the ray tracing experiment should approach the direct channel measurements in as many respects as possible. In particular, care was taken to reproduce the measurement locations, system power level, and the time/angle resolution of the data to suitably justify a direct comparison.

3.2 *WiSE*© Simulation Software

The Wireless Research Group at Lucent Technologies in Holmdel, New Jersey has developed a 3-D predictive simulator for wireless channel propagation referred to as *WiSE* for *Wireless System Engineering*. It makes use of computational geometry, building environment descriptions, and a complex propagation model to predict the highest strength propagation paths from arbitrary transmitter and receiver locations within a static environment [9]. Three dimensional ray-tracing is used to include the effects of frequency, polarization, the dielectric properties of encountered materials, diffraction around corners, and antenna directivity. To speed up the computationally intensive task of predicting all possible illumination paths from transmitter to receiver, only rays with power above a fixed threshold are perpetuated through the model.

www.manaraa.com

Also, rays which are outside of the three dimensional cone illuminated by reflections off of a particular wall interface are discarded. This simulation tool allows deterministic prediction of the impulse response of wireless channels for both time and angle of arrival.

The primary input into the simulator is a building geometry description which lays out the reflective surfaces in the environment as well as their properties. The locations of walls and other planar features are described by specifying the three-space coordinates of opposing corners. Then, to describe the electromagnetic behavior, the wall material can be specified from a pre-defined list which includes ground (no transmission), wood, sheetrock, concrete (with various loss factors), metallic partition, or glass. If these pre-defined wall material types are not sufficient, custom wall types can be defined by specifying a stack of dielectric layers with an additional transmission and reflection loss factor. For each layer, the thickness, dielectric constant, and conductivity can be set individually. Where two non-coplanar walls meet at a single line segment (to within an adjustable tolerance), the simulator identifies a *wedge* where diffractions can occur.

To initiate a simulation of a particular broadcast realization, the simulation is started with a parameter input file that outlines the parameters of the "system" under test. The first system parameters identify the location, frequency, power, type, and orientation of the transmitter(s) and receiver(s). The WiSE package has predefined antenna types that include dipole, patch, and isotropic. An antenna pattern definition file can be used to specify the antenna gain pattern of any other desired antenna type. Second, we set the ray tracing model parameters. There are three different ray tracing models which include image (traditional), 2-dimensional pin cushion (applicable to urban microcells), and 3-dimensional pin cushion (often used for rooftop urban microcells, but quite slow). The software also allows power prediction without ray tracing using the power law exponent model and the Keenan-Motley model which describes angle-independent transmission/reflection coefficients and an

www.manaraa.com

adjustable power law exponent. Finally, we specify the number of bounces to consider and the minimum power threshold of rays which are propagated in the model. Depending on the complexity of the environment model and the number of bounces being considered, the run time of the simulation can vary from 20 minutes to 4 hours.

The results of the simulation can be displayed graphically superimposed on the environment map or output to a file in a variety of formats. The *receiver coverage* option produces received power and RMS delay data for every receiver or grid point specified. Alternatively, the *path definition* option produces a full definition of the dominant paths along with their respective power contribution to each receiver. The paths are delineated by identifying the number of bounces for each ray as well as the 3-space end points for each path segment as the ray travels from the transmitter to the receiver. The *path definition* output file is especially useful for extracting the angles of departure/arrival and the path delay for each ray. Some typical results are displayed graphically in Figure 3.1.

3.3 Development of the Clyde Building Environment Model

The original building geometry model was generated by converting the CAD architectural layouts from the BYU Planning Office into the WiSE WALL format as shown in Figure 3.2. The CAD file represented each wall as a rectangle to show its thickness as well as position. When these rectangles were converted line-by-line into planar wall entities in the WiSE model, each wall segment resulted in four distinct surfaces for transmission and reflection. As a consequence, the density of interaction surfaces in the ray tracing model was too high to allow for quick simulation, and run times were typically around four hours per location.

We assumed that the out-of-plane contributions from reflections from the floor and ceiling surfaces could be ignored. The entire 4th floor of the Clyde Engineering Building was described as a collection of vertical planes with uniform wall material properties and no reflecting floor or ceiling surfaces. In reproducing the 55 original measurements from the Clyde Building with the ray tracing simulation, the results

www.manaraa.com

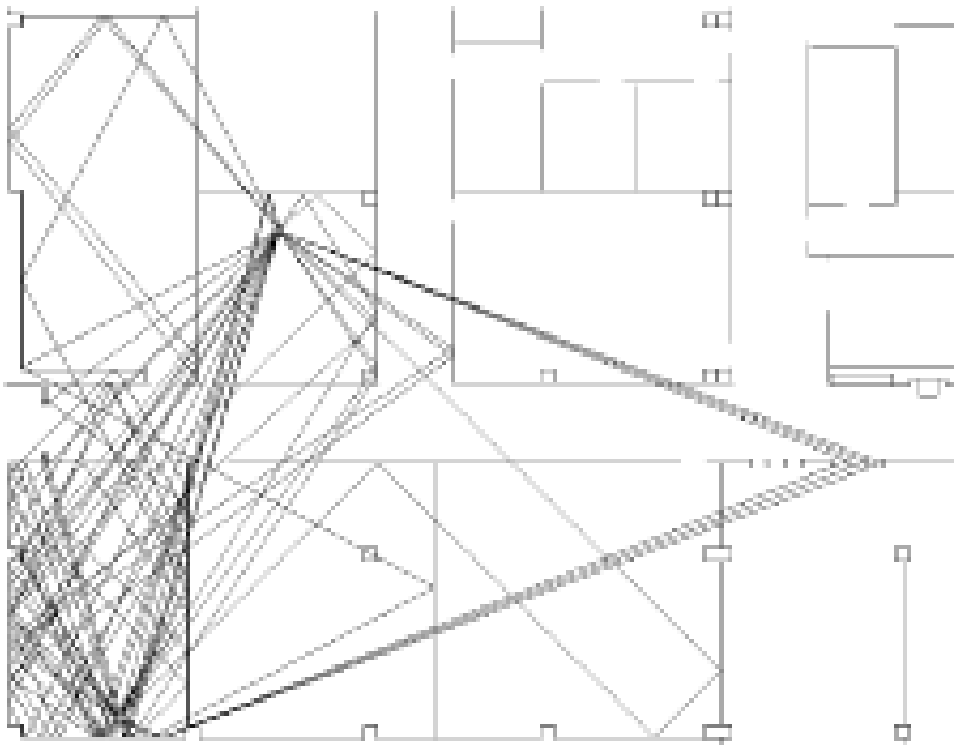

Figure 3.1: Typical results of ray tracing simulation for a single transmitter/receiver location pair.

were qualitatively similar to the measurements. However, applying the same statistical analysis to the simulation data as had been used for the measurements produced parameter values that were less consistent than desired. We considered that the parameter values might be influenced by the choice of wall materials in the building model. As the selection of material composition for all the walls was varied from sheet rock, wood, and concrete, the results of the simulation did not change appreciably.

In consideration of the weak agreement of these initial ray tracing results, we decided to refine the building geometry description. The primary improvement was to focus on the location and properties of the metallic reflection surfaces in the building. On further investigation of the architectural blueprints, it was discovered that the exterior walls of the building have steel reinforcing rods placed vertically with 11 inch separation between their centers. These reflective scatterers were added to the new

www.manaraa.com

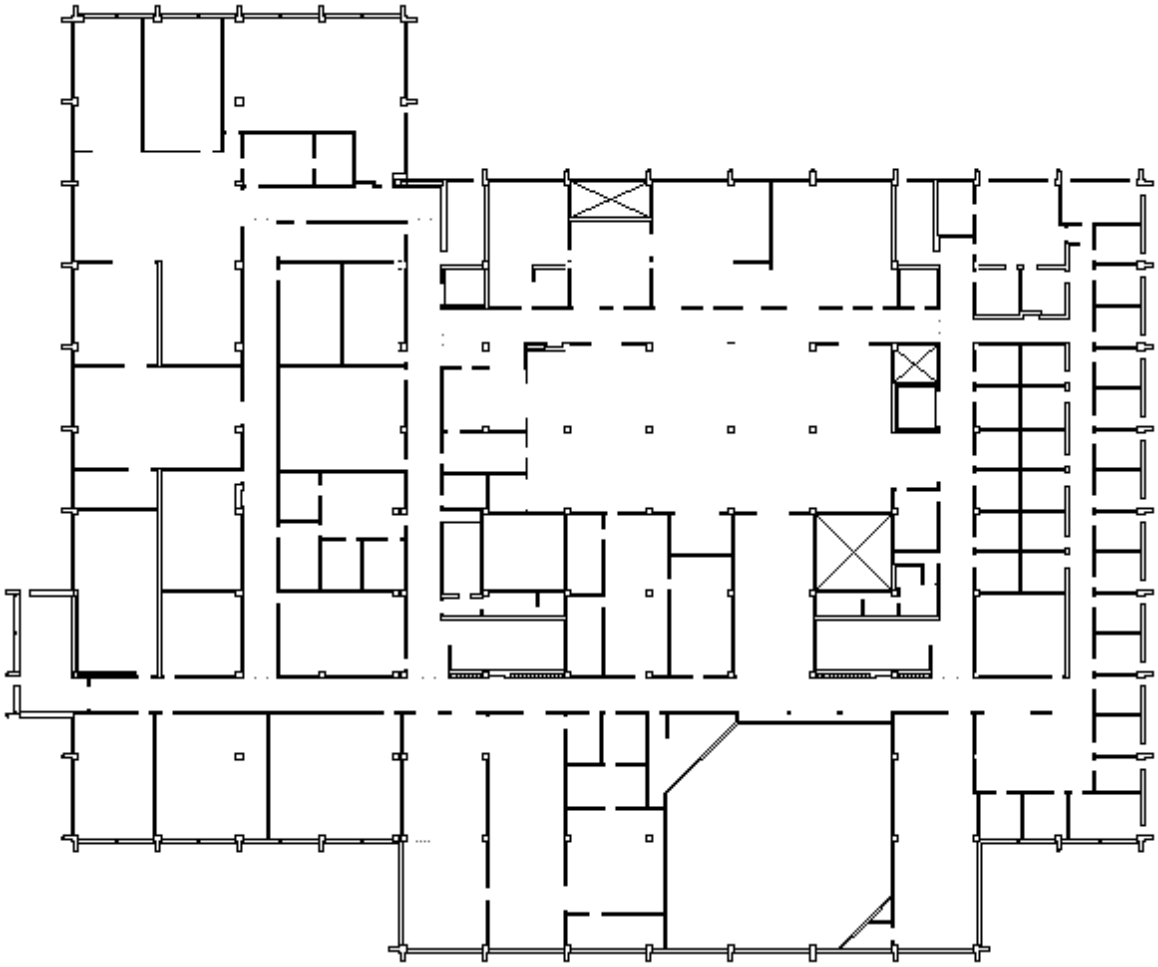

Figure 3.2: Original CAD drawing of Clyde Building 4th floor.

model along with the metal door and window frames. We also included the metal storage lockers and drinking fountains. The significant effort required to increase the detail of the model to this level made it necessary to reduce the coverage area of the building. By limiting the model area to the northwest quarter, we were able to preserve the locations used in 50 of the original 55 measurement sets. The revised model is shown in Figure 3.3.

www.manaraa.com

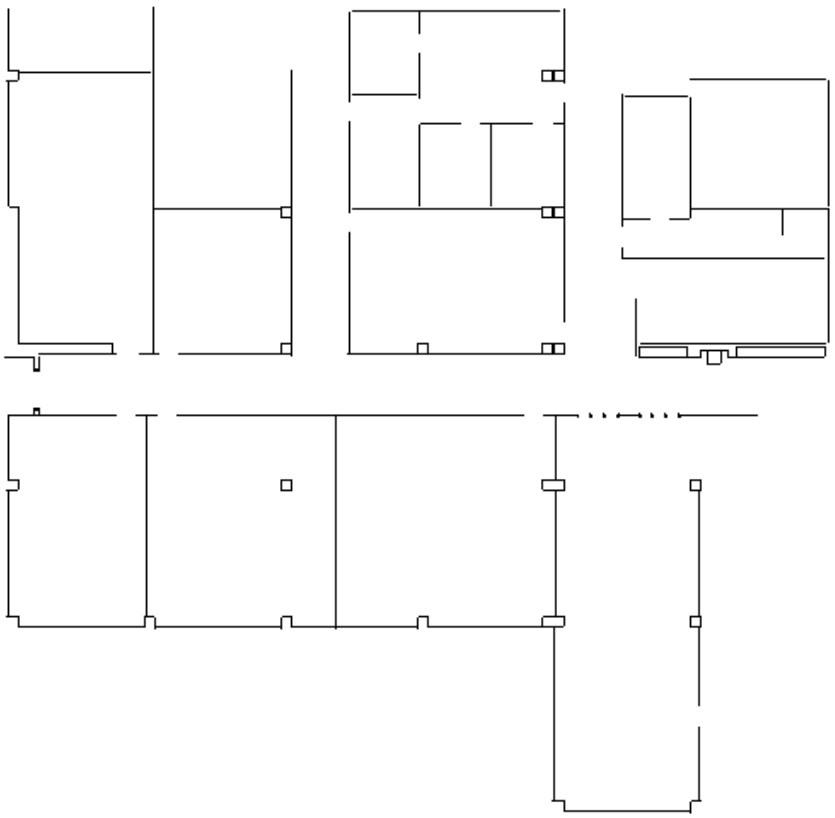

Figure 3.3: Revised model of Clyde Building 4th floor (northwest corner).

3.4 Selection of Simulation Parameters

In order to justify the comparison of the ray tracing simulation results with the previously measured data, we made every effort to reproduce the measurement conditions in the simulation. The location of the transmitter and receiver for each experiment was dictated by the distance south and west of the northeast corner of the room in which they were located. A look-up table in the MATLAB batch script translated the room number for each broadcast endpoint into x and y coordinates in the geometry model. The simulated receiver and transmitter locations were determined by adding the appropriate coordinate offset for the location within each room. The antennas at each location were modeled as isotropic sensors to remove the effects

www.manaraa.com

of a azimuthally varying antenna gain pattern in the same way that the antenna gain pattern was removed from the measurement data during post-processing. The frequency of the simulation was chosen to be 7.0 GHz to correspond to the frequency at which the measurements were taken.

The ray tracing model was chosen as the image (geometric) model recommended for indoor environments, and the power law was selected as R^2. In an effort to balance simulation accuracy against computation time, the maximum number of bounces allowed for any ray was chosen to be 5. All other propagation model parameters were left at their default values.

The simulation parameter that was most critical in normalizing the results was the apparent system transmit power. The ray tracing software allowed the variation of the power level at the transmitter, but even radical changes in this parameter had no observable effect on the results of the simulation. Instead, we normalized the simulated transmit power by adjusting the minimum power threshold (in mW) for rays which are propagated through the simulation environment. This parameter seemed to have the most direct influence on the number of rays that were detected at the receiver. We selected a value for the power threshold which resulted in the total number of rays generated after resolution screening accumulated over all of the simulation sets being equivalent to the number of arrivals detected in the measurement data summed over all 50 locations. Figure 3.4 shows the variation in the total number of ray arrivals as the value of the power threshold changes.

The total number of CLEAN peaks detected in the measurement data over the 50 locations of interest was 2213. By choosing the value of the power threshold to be $2.6\,x\,10^{-7}$, the total number of rays produced by the simulation after resolution processing was 2192. If the transmitter power was taken to be 1 mW, the equivalent SNR of the system would be $10\,log_{10}(\frac{P_{transmit}}{P_{noise}}) = 10\,log_{10}(\frac{1}{2.6\times10^{-7}}) = 65.9$ dB.

www.manaraa.com

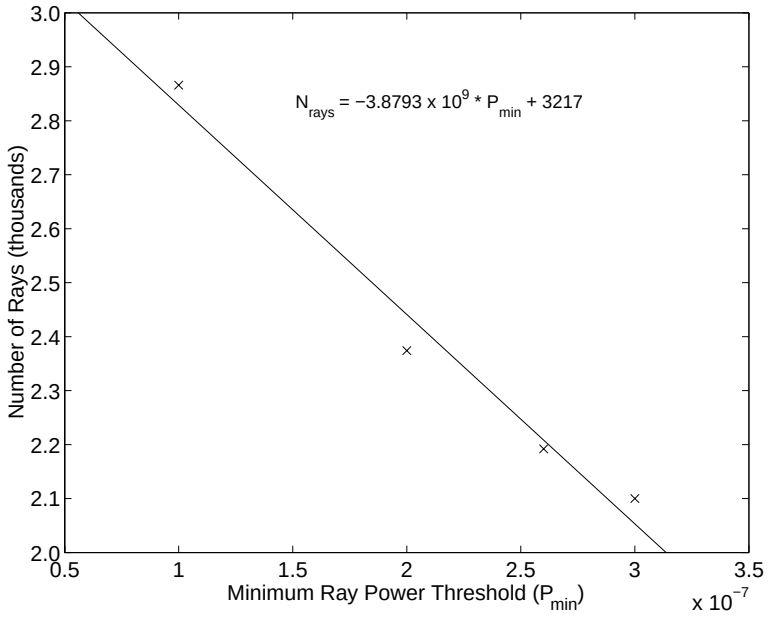

Figure 3.4: Total number of rays versus power threshold parameter value.

www.manaraa.com

Chapter 4

Comparison of Ray Tracing Simulation Results with SISO Channel Measurements

4.1 Introduction

We replicated the indoor channel measurements with the WiSE software package using the normalized simulation parameters discussed in Chapter 3. The original measurements were made by transmitting a chirp signal centered at 7 GHz from a stationary dipole antenna. A network analyzer recorded the channel frequency response at the receiver where a dish antenna was rotated in 2° increments between chirps through a full circle to measure the channel response as a function of arrival angle. The channel impulse response was calculated by transforming the frequency response back to the time domain, and discrete arrivals were detected by finding replicas of the system point spread function with successive subtraction. The ray tracing simulator recreated the 50 measurement location pairs from the northwest corner of the 4th floor of the Clyde Engineering Building with parameters chosen to most closely match the conditions of the measurement data. By processing the simulation output files, we were able to gather data on the time and angle distribution of the dominant arrivals predicted from the building environment model. The analysis software filtered the ray arrivals using the same resolution characteristics as the original measurement hardware. The net result was to synthesize a spatio-temporal impulse response where the discrete ray arrivals are analogous to the arrivals detected in the measurement data. Spencer observed that the measured channel impulse response fit a model similar to that proposed by Saleh and Valenzuela [7]. By grouping ray arrivals into clusters, the

www.manaraa.com

spatial impulse response information could be analyzed statistically to estimate the values of the model parameters [2]. When an identical analysis was applied to the spatial impulse response information produced by the ray tracing software, the results corresponded very closely to the measurement observations both in the structure of the spatial clustering and in the values of the model parameter estimates.

4.2 Synthesis of the Spatial Impulse Response

We used MATLAB scripts to extract the information from the ray tracing predictions for each transmitter/receiver location pair. Parsing the *path definition* output file gave us the 3-D coordinates of each bounce location along the path traveled by each ray along with its predicted power contribution at the receiver. The departure and arrival angles were calculated from the directions of the first and last path segments, and the sum of the lengths of the path segments determined the path delay for each ray.

The original measurement experiment had a minimum resolution of 0.5 ns in time and 2° in angle. The software processing duplicated this effect by creating a resolution grid with identical spacing. When multiple arrivals occurred in a single cell, all but the first arrival were discarded. Of the 2,459 rays initially predicted by the simulator, only 2192 remained after resolution screening.

The predicted spatial impulse response of the channel for each location can be represented on a scatter plot where each ray is assigned an x-y location from its angle of arrival at the receiver and its path delay. The spatial clustering structure described by the extended Saleh-Valanzuela model in [6] is immediately apparent in the simulated channel response as demonstrated in Figure 4.1. The channels represented in this figure demonstrate that although there is definite correlation between the measured and simulated channels, the agreement is more likely to be on a cluster scale rather than matching individual ray arrivals.

www.manaraa.com

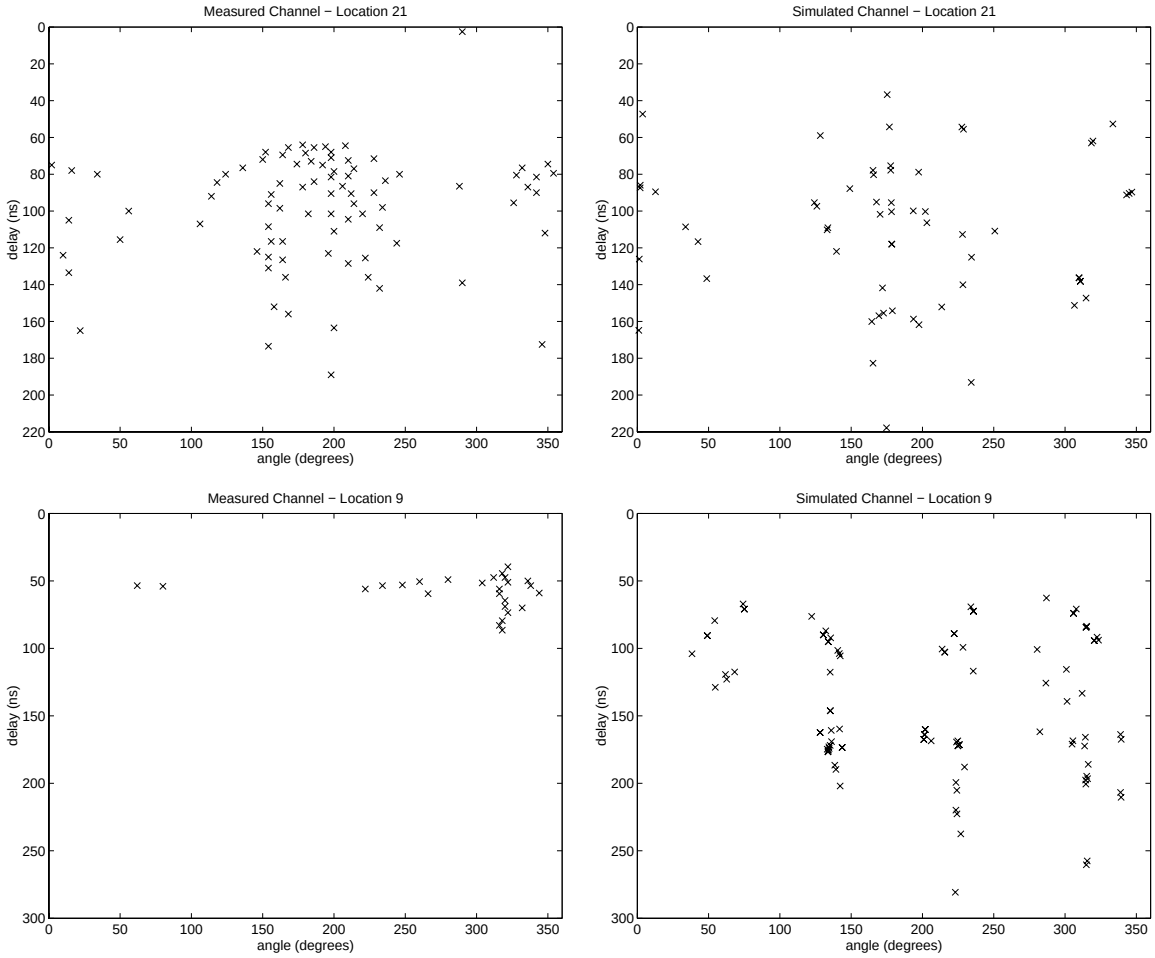

Figure 4.1: Comparison of time-angle plots for measured channel (left) and synthesized channel response (right) at location 21 (top) and location 9 (bottom).

4.3 Space-Time Clustered Channel Model [2]

The time/angle clustering structure observed in the indoor channel response measurements is described by a spatially extended model proposed by Spencer in [2] and [6] based on earlier time-only channel propagation modeling done by Saleh and Valenzuela [7]. The model describes the indoor propagation channel response as a collection of clusters which are formed from a sum of rays which arrive at the receiver localized in both time and angle of arrival. The time/angle impulse response

www.manaraa.com

is described in [6] as:

$$h(t,\theta) = \sum_{l=0}^{\infty}\sum_{k=0}^{\infty} \beta_{kl} e^{j\phi_{kl}} \delta(t - T_l - \tau_{kl}) \delta(\theta - \Theta_l - \omega_{kl}) \,, \tag{4.1}$$

where the sum over l represents the clusters, and the sum over k represents the rays within each cluster. The electrical phase of each ray, ϕ_{kl}, is assumed to result from an independent and identically distributed uniform random process over the interval $[0, 2\pi)$.

The magnitude of each ray, β_{kl}, is modeled as a Rayleigh distributed random variable with mean square value described by a doubly decaying exponential curve as illustrated in Figure 4.2. The mean squared power of the rays is assumed to decay with time within the decaying envelope of the mean squared cluster power. The mathematical expression for the mean of the power distribution as a function of time is:

$$\overline{\beta_{kl}^2} = \overline{\beta^2(T_l, \tau_{kl})} = \overline{\beta^2(0,0)}\, e^{-T_l/\Gamma}\, e^{-\tau_{kl}/\gamma} \,, \tag{4.2}$$

where $\overline{\beta^2(0,0)}$ is the average power of the first arrival of the first cluster and is derived as explained in [2] and [7] as a function of the separation distance between the transmitter and receiver, the RF wavelength of the system, and the gain of both antennas. The parameters Γ and γ represent the time constant of the exponential decay of the magnitude envelope with cluster delay time and ray delay time respectively.

The time of arrival for clusters and rays within clusters is dictated by independent Poisson processes with rate parameters Λ and λ respectively. As a result, the time intervals between arrivals (of either clusters or rays) follow continuous exponential distributions conditioned on the time of arrival of the previous cluster or ray as described in the following:

$$p\left(T_l | T_{l-1}\right) = \Lambda\, e^{-\Lambda(T_l - T_{l-1})}, \qquad T_{l-1} < T_l < \infty \tag{4.3}$$

$$p\left(\tau_{kl} | \tau_{(k-1)l}\right) = \lambda\, e^{-\lambda(\tau_{kl} - \tau_{(k-1)l})}, \qquad \tau_{(k-1)l} < \tau_{kl} < \infty \,. \tag{4.4}$$

One important consequence of the conditional distribution of the times of discrete

www.manaraa.com

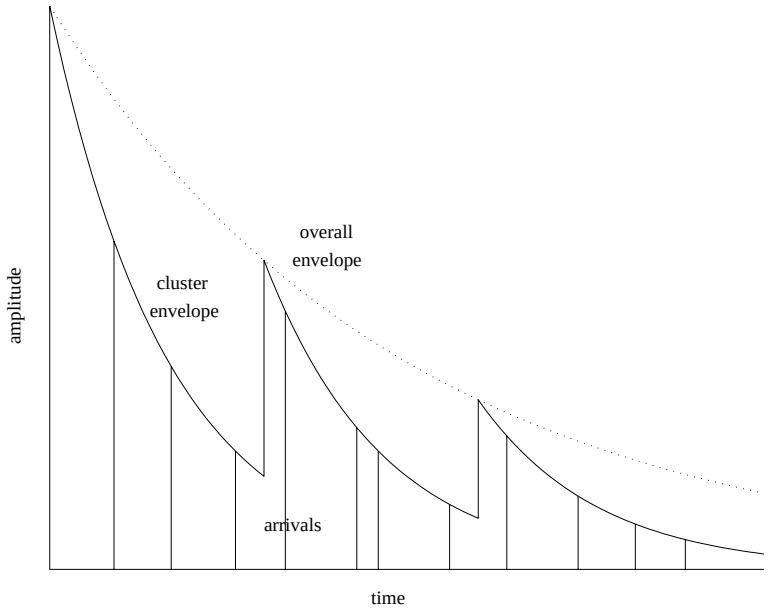

Figure 4.2: Mean value of ray power, $\overline{\beta_{kl}^2}$, as a function of time.

cluster and ray arrivals is that we can use the intercluster arrival times (relative cluster arrival times) to estimate the cluster arrival rate parameter, Λ, and the intracluster arrival times (relative ray arrival times) to estimate the ray arrival rate parameter, λ. These results are derived in Section 4.5.2 on page 44.

The main contribution of this channel response model is its description of the angular clustering of arrivals at the receiver. The angle at which each ray arrives at the receiver is specified relative to the mean arrival angle of all the rays in its parent cluster, Θ_l. The deviation of each ray's arrival angle from the mean angle in the cluster is modeled by the parameter ω_{kl}, which is taken to have a Laplacian distribution with standard deviation σ:

$$p(\omega_{kl}) \quad = \quad \frac{1}{\sqrt{2}\sigma} \, \mathrm{e}^{-|\sqrt{2}\omega_{kl}/\sigma|} \, . \tag{4.5}$$

In proposing this model in [6], Spencer discusses the potential for correlation between the time and angle of each ray's arrival. From his observations that scatter plots of the time and angle of cluster or rays relative to the time and angle of the first cluster or ray displayed no correlation, the time and angle distributions are concluded

www.manaraa.com

to be independent resulting in cluster and ray parameters whose probability densities are separable functions:

$$p(T_l, \Theta_l | T_{l-1}, \Theta_0) = p(T_l | T_{l-1})\, p(\Theta_l | \Theta_0) \quad (4.6)$$

$$p(\tau_{kl}, \omega_{kl} | \tau_{(k-1)l}) = p(\tau_{kl} | \tau_{(k-1)l})\, p(\omega_{kl})\,. \quad (4.7)$$

This allows the time parameters for clusters and rays to be estimated independently from the corresponding angular parameters.

4.4 Cluster Identification

Once we have generated the time/angle channel impulse response from either measured or simulated data, we need to group the arrivals into temporo-spatial clusters in preparation for estimating the parameter values for the model. We used the original manual cluster finding method proposed by Spencer [2] using a graphical user interface. When the clusters are sufficiently separated and the number of data sets is not too high, this method can be reasonably practical and repeatable. At the normalized power level used for the simulations, the resulting clusters were well separated. However, when simulating higher power levels, the clusters can have heavily populated tails in their angular spread such that neighboring clusters will overlap significantly and cannot be well identified using this simple graphical cluster identification algorithm. Figure 4.3 shows an example of cluster overlap at higher power levels and the difficulty of visually separating arrivals into their parent clusters without additional information such as amplitude decays.

In addition, we observed that the values of the model parameter estimates (particularly the angular spread parameter, σ) could be significantly affected by changing the assumptions made during cluster identification. As an example, we re-clustered the simulation data from the original building geometry model with uniform sheet rock wall composition under the assumption that the clusters were wider and longer. Figure 4.4 shows the variation in the clustering strategies applied to the same data. The effect on the model parameter estimates using the wide/long clustering strategy

www.manaraa.com

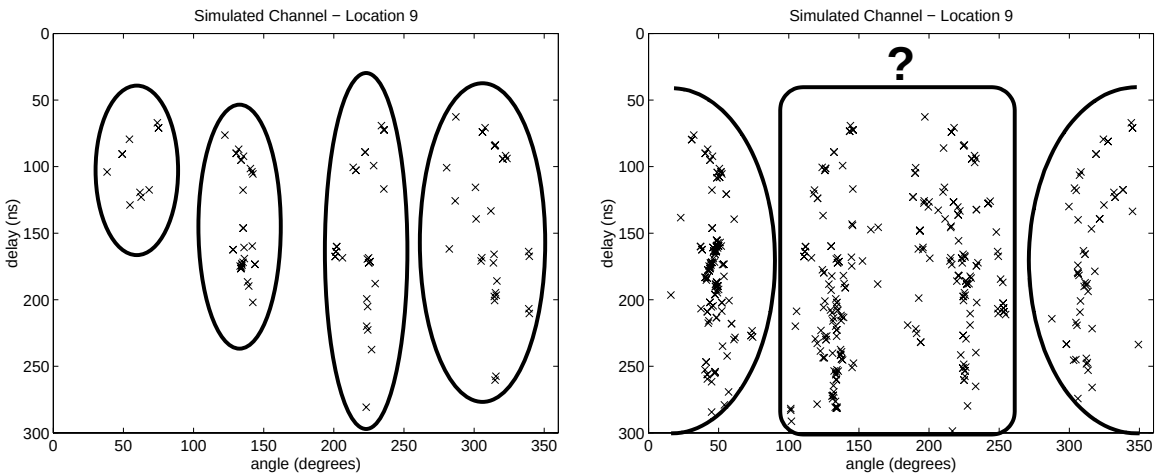

Figure 4.3: Comparison of cluster overlap as the simulated power level is increased.

was most noticeable in the radical increase in the estimated standard deviation of the angular spread distribution, σ. The cluster arrival rate, λ was essentially unchanged. Table 4.1 compares the parameter estimates resulting from each clustering strategy. An additional effect of assuming clusters with wider angular spread is that the total number of identified clusters is sharply reduced. Where the quantity of relative cluster arrival time data available to estimate the cluster arrival rate parameter, Λ, is limited, the reduction of cluster data in the cluster identification stage may bring the variance of this estimate into question. From these observations, we recognize the limitations associated with manual cluster identification. Because the clusters in this simulation data were distinct and non-overlapping, it was easy to visually separate arrivals into clusters without using additional information or resorting to more

Table 4.1: Comparison of model parameter values using different cluster identification strategies.

Model Parameter	**Narrow Clusters**	**Wide Clusters**
σ	16.1°	62.9°
$1/\lambda$	1.65 ns	1.56 ns

www.manaraa.com

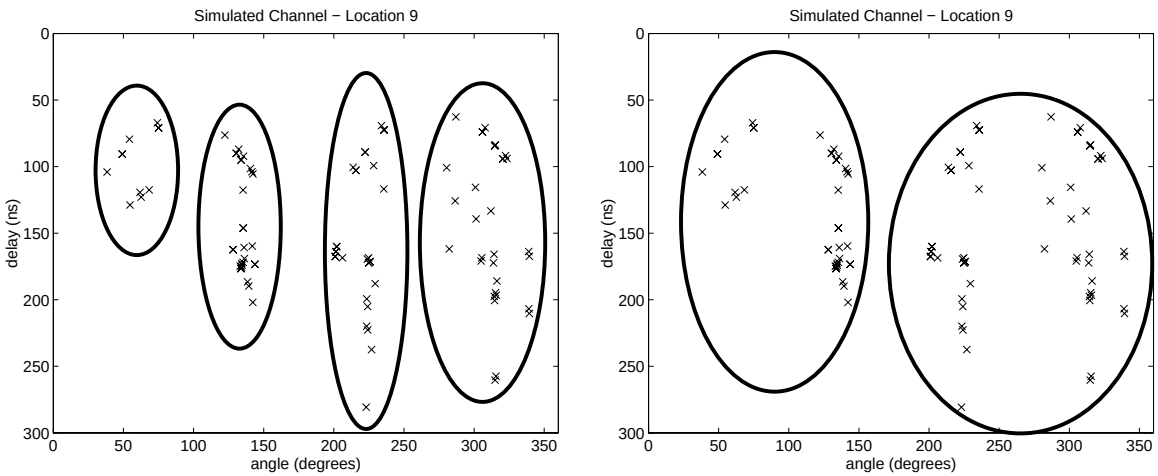

Figure 4.4: Comparison of cluster strategies applied to identical data.

complex automatic clustering methods. Also, because the number of distinct cluster groups per data set was low, only radical variation in the clustering strategy could affect the cluster grouping. As long as a reasonable strategy was applied consistently over all of the data sets, the cluster identification results were sufficiently repeatable to avoid introducing variations into the model parameter estimates.

4.5 Estimation of Model Parameters

In order to justify a direct comparison of the parameter estimates derived from the simulated channel response with those from the SISO measurements, we need to apply identical analysis to both sets of data. We used the original MATLAB scripts written by Quentin Spencer to calculate the Least Squares (LS) estimates of the model parameters from data describing the relative angles of arrival for rays and the relative times of arrival for rays and clusters. These estimators select the value of the parameter which minimizes the sum of the squared error of the distribution curve to the histogram of the data as described in the following sections. In addition, the power decay rate parameters for both clusters and rays were estimated using the same LS linear regression approach used on the previous data.

www.manaraa.com

4.5.1 Laplacian Distributed Parameters

As described in the Space-Time Clustered Channel Model of [2] and [6], the angular spread of a cluster around its mean angle follows a zero-mean Laplacian Distribution and is described by the following probability density function:

$$p\left(\omega_{kl}, \sigma\right) \quad = \quad \frac{1}{\sqrt{2}\sigma} \, \mathrm{e}^{-|\sqrt{2}\omega_{kl}/\sigma|} \, . \tag{4.8}$$

The zero-mean Laplacian Distribution is fully specified by a single parameter, σ, which represents the standard deviation of the distribution. The mean of the distribution is always zero, but the width of the pdf is determined by σ. Large values of σ result in a very wide, flat curve indicating higher probabilities of arrival angles farther from the mean than for a lower value of σ. The estimator should select the value of σ which "best" fits a zero-mean Laplacian distribution to the values of arrival angles represented in the data.

The first step is to form a histogram to measure the relative frequency of values in the data. If we view $x_1, x_2, \ldots, x_n$ as the set of n data values for the angles of arrivals for rays relative to the mean cluster arrival angle, we choose the range for the histogram bin centers using the minimum magnitude present in the data in the following way:

$$a = -\max_i |\, x_i \,| \qquad b = +\max_i |\, x_i \,| \, . \tag{4.9}$$

For an N bin histogram, the bin centers, $c_1, c_2, \ldots, c_N$, are defined as:

$$c_i = a + \frac{(i-1)\,(b-a)}{N-1} \qquad i = 1, 2, \ldots, N \, . \tag{4.10}$$

The bin edges delineate the partition of the range of values and can be expressed in terms of the bin centers, $c_1, c_2, \ldots, c_N$, as:

$$\begin{array}{ll} P_1 & (-\infty, \frac{c_1+c_2}{2}] \\ P_2 & (\frac{c_1+c_2}{2}, \frac{c_2+c_3}{2}] \\ P_3 & (\frac{c_2+c_3}{2}, \frac{c_3+c_4}{2}] \\ \vdots & \vdots \\ P_N & (\frac{c_{n-1}+c_n}{2}, \infty) \, , \end{array} \tag{4.11}$$

www.manaraa.com

where partitions $P_2, \ldots, P_{N-1}$ are of width $(b-a)/(N-1)$. The number of samples in bin P_k can be expressed in terms of the cardinality of the set:

$$n_k = |\ \{\ x_i \mid x_i \in P_k\ \}\ | \,. \tag{4.12}$$

The normalized histogram is then formed as an ordered set of relative frequencies, $h_1, \ldots, h_N$, where

$$h_k = \frac{n_k}{n} \qquad k = 1, 2, \ldots, N \,. \tag{4.13}$$

The Least Squares (LS) criterion for selecting the "best" value of σ to fit the relative angle of arrival data is defined in terms of the normalized histogram and the parameterized zero-mean Laplacian distribution, $p(\omega_{kl}, \sigma)$:

$$\sigma_{\mathrm{LS}} = \arg\min_{\sigma} \left\{ \sum_{k=1}^{N} \left| h_k - \int_{P_k} p(\omega_{kl}, \sigma)\, \mathrm{d}P_k \right|^2 \right\} . \tag{4.14}$$

The integral in Equation 4.14 can be written for the zero-mean Laplacian distribution in the following closed form derived below where P_k is the interval $(c, d]$:

$$\begin{aligned} F \quad = \quad \int_{P_k} p(x, \sigma)\, \mathrm{d}P_k \quad &= \quad \int_c^d \frac{1}{\sqrt{2}\sigma}\, \mathrm{e}^{-|\sqrt{2}x/\sigma|}\, \mathrm{d}x \\ &= \quad \begin{cases} \frac{1}{2}\left(\mathrm{e}^{\sqrt{2}d/\sigma} - \mathrm{e}^{\sqrt{2}c/\sigma}\right) & : \quad c, d \le 0 \\ \frac{1}{2}\left(2 - \mathrm{e}^{\sqrt{2}c/\sigma} - \mathrm{e}^{-\sqrt{2}d/\sigma}\right) & : \quad c \le 0, d \ge 0 \\ \frac{1}{2}\left(\mathrm{e}^{-\sqrt{2}c/\sigma} - \mathrm{e}^{-\sqrt{2}d/\sigma}\right) & : \quad c, d \ge 0 \end{cases} \end{aligned} \tag{4.15}$$

Case I : $c, d \le 0$

$$\begin{aligned} F \quad &= \quad \int_c^d \frac{1}{\sqrt{2}\sigma}\, \mathrm{e}^{\sqrt{2}x/\sigma}\, \mathrm{d}x \\ &= \quad \frac{1}{2}\, \mathrm{e}^{\sqrt{2}x/\sigma}\Big|_c^d \\ &= \quad \frac{1}{2}\left(\mathrm{e}^{\sqrt{2}d/\sigma} - \mathrm{e}^{\sqrt{2}c/\sigma}\right) \end{aligned}$$

www.manaraa.com

Case II : $c \leq 0\ ,\ d \geq 0$

$$\begin{aligned} F &= \int_c^0 \frac{1}{\sqrt{2}\sigma}\, \mathrm{e}^{\sqrt{2}x/\sigma} + \int_0^d \frac{1}{\sqrt{2}\sigma}\, \mathrm{e}^{-\sqrt{2}x/\sigma}\, \mathrm{d}x \\ &= \frac{1}{2}\, \mathrm{e}^{\sqrt{2}x/\sigma}\Big|_c^0 - \frac{1}{2}\, \mathrm{e}^{-\sqrt{2}x/\sigma}\Big|_0^d \\ &= \frac{1}{2}\, (2 - \mathrm{e}^{\sqrt{2}c/\sigma} - \mathrm{e}^{-\sqrt{2}d/\sigma}) \end{aligned}$$

Case III : $c, d \geq 0$

$$\begin{aligned} F &= \int_c^d \frac{1}{\sqrt{2}\sigma}\, \mathrm{e}^{-\sqrt{2}x/\sigma}\, \mathrm{d}x \\ &= -\frac{1}{2}\, \mathrm{e}^{-\sqrt{2}x/\sigma}\Big|_c^d \\ &= \frac{1}{2}\, (\mathrm{e}^{-\sqrt{2}c/\sigma} - \mathrm{e}^{-\sqrt{2}d/\sigma})\ . \end{aligned}$$

The Laplacian curve fits to simulated angle of arrival data use the LS estimator for σ described in Equation 4.14 with the number of bins, N, chosen to be 100 to match the Laplacian fits for the SISO data. The LS estimate of σ for simulated data was 23.4° as compared with 25.5° obtained from the measurements. The zero-mean Laplacian fits are compared in Figure 4.5 where the "best fit" distributions are superimposed over the normalized histograms.

4.5.2 Exponentially Distributed Parameters

The discrete arrivals of clusters and rays within clusters is described in the Space-Time Clustered Channel Model using independent Poisson processes with rate parameters Λ and λ respectively. The Poisson process arises from the following assumptions about the occurrence of discrete events (This development of the Poisson-Exponential relationship closely follows material found in [63]):

(i) The probability of an event occurring during a very small interval of time from t to $t + \Delta t$ is $\lambda \cdot \Delta t$,

(ii) The probability of more than one event occurring during the interval from t to $t + \Delta t$ is small enough to be ignored,

www.manaraa.com

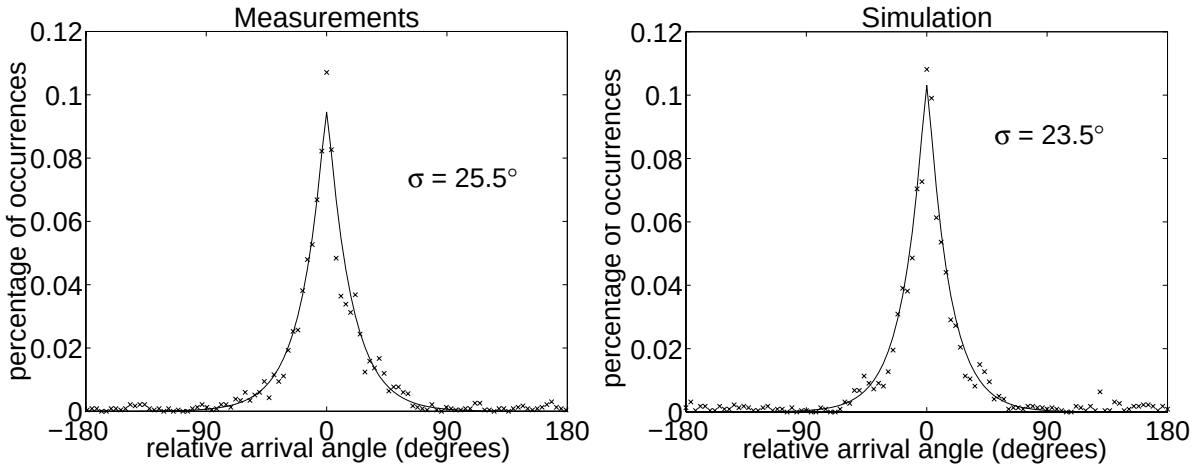

Figure 4.5: LS Laplacian fit to angle of arrival data from SISO measurements(left) and ray tracing simulation(right).

(iii) The probability of an event occurring between t and $t + \Delta t$ does not depend at all on whatever occurred before time t.

Under these conditions, we can express $f(x,t)$, the probability that x events occur during a time interval of length t using the Law of Total Probability as the probability that $x-1$ events have occurred in the interval $t - \Delta t$ times the probability that 1 event occurs between $t - \Delta t$ and t added to the probability that x events occurred in the interval $t - \Delta t$ times the probability that an event does not occur between $t - \Delta t$ and t:

$$f(x,t) = f(x-1, t-\Delta t)\,\lambda \cdot \Delta t + f(x, t-\Delta t)\,(1 - \lambda \cdot \Delta t)\,. \tag{4.16}$$

We can make use of this to show that the derivative of $f(x,t)$ is formed as:

$$\begin{aligned} \frac{\mathrm{d}[f(x,t)]}{\mathrm{d}t} &= \lim_{\Delta t \to 0} \frac{f(x, t+\Delta t) - f(x,t)}{\Delta t} \\ &= \lim_{\Delta t \to 0} \frac{f(x-1,t)\lambda \cdot \Delta t + f(x,t)(1 - \lambda \cdot \Delta t) - f(x,t)}{\Delta t} \\ &= \lim_{\Delta t \to 0} \frac{f(x-1,t)\lambda \cdot \Delta t - f(x,t)\lambda \cdot \Delta t}{\Delta t} \\ &= \lambda\,[f(x-1,t) - f(x,t)]\,. \end{aligned} \tag{4.17}$$

www.manaraa.com

Using substitution, it can be shown that the system of differential equations formed by Equations 4.16 and 4.17 can be solved by the Poisson distribution function

$$p\,(x, \lambda t) = \frac{(\lambda t)^x \; \mathrm{e}^{-\lambda t}}{x!} \tag{4.18}$$

for any value of $x = 0, 1, 2, \ldots, \infty$. We are particularly interested in the continuous distribution which describes the waiting time between events which we will represent with the random variable X. This can be identified by examining the cumulative distribution function:

$$\begin{aligned} F(y) &= P(Y \leq y) = 1 - P(Y \geq y) \\ &= 1 - P(0 \text{ events in time interval of length } y) \\ &= 1 - p(0, \lambda y) \qquad \text{(from Eq. 4.18)} \\ &= 1 - \frac{(\lambda y)^0 \; \mathrm{e}^{-\lambda y}}{0!} \\ &= \begin{cases} 1 - \mathrm{e}^{-\lambda y} & \text{for } y > 0 \\ 0 & \text{for } y \leq 0\,. \end{cases} \end{aligned} \tag{4.19}$$

If we differentiate with respect to the time variable, y, we find that the probability density function for times between events is

$$f(y) = \frac{\mathrm{d}F(y)}{\mathrm{d}y} = \begin{cases} \lambda \, \mathrm{e}^{\lambda y} & \text{for } y > 0 \\ 0 & \text{for } y \leq 0 \end{cases} \tag{4.20}$$

which is exactly the exponential distribution we described for the relative times of cluster and ray arrivals in Equations 4.3 and 4.4 on page 37. The significant result of this development is that it becomes possible to estimate the rate parameter of a Poisson process using data that represent the relative times between event occurrences.

If we take the absolute times of arrivals for $n + 1$ clusters, $T_1, T_2, \ldots, T_{n+1}$, and form the n relative times of cluster arrivals as

$$x_i = T_{i+1} - T_i \qquad\qquad i = 1, 2, \ldots, n\,, \tag{4.21}$$

www.manaraa.com

we can re-write Equation 4.3 in terms of x_i as:

$$p\,(x_i\,,\ \Lambda) = \Lambda\ \mathrm{e}^{-\Lambda\,x_i}\ . \tag{4.22}$$

In an analogous way, when x_i represents the relative times of $n+1$ ray arrivals, as in

$$x_i = \tau_{(i+1)l} - \tau_{i\,l} \qquad\qquad i = 1, 2, \ldots, n\ , \tag{4.23}$$

the distribution in Equation 4.4 becomes:

$$p\,(x_i\,,\ \lambda) = \lambda\ \mathrm{e}^{-\lambda\,x_i}\ . \tag{4.24}$$

Note that these exponential distributions are completely specified by a single parameter, Λ or λ respectively which is equal to 1 over the mean of the distribution and 1 over the standard deviation.

The next step is to form the normalized histogram for the relative event time data in the same way as the exponential LS estimator originally used for the SISO Channel measurements. The range of the histogram was determined by

$$a = \mathrm{round}\{\max_i\ x_i\} \tag{4.25}$$

and partitioned into N bins:

$$\begin{array}{cc} P_1 & [0, \frac{a}{N}) \\ P_2 & [\frac{a}{N}, \frac{2a}{N}] \\ P_3 & [\frac{2a}{N}, \frac{3a}{N}] \\ \vdots & \vdots \\ P_N & [\frac{(N-1)\,a}{N}, a)\ . \end{array} \tag{4.26}$$

The number of samples in bin P_k can be expressed in terms of the cardinality of the set:

$$n_k = |\ \{\ x_i \mid x_i \in P_k\ \}\ |\ . \tag{4.27}$$

The normalized histogram is then formed as an ordered set of relative frequencies, $h_1, \ldots, h_N$, where

$$h_k = \frac{n_k}{n} \qquad k = 1, 2, \ldots, N\ . \tag{4.28}$$

www.manaraa.com

The Least Squares (LS) criterion for selecting the "best" value of Λ (or λ as appropriate) to fit the relative event time data is defined in terms of the parameterized exponential distribution, $p\left(x_i, \Lambda\right)$ and the normalized histogram,

$$\Lambda_{\mathrm{LS}} = \arg\min_{\Lambda} \left\{ \sum_{k=1}^{N} \left| h_k - \int_{P_k} p\left(x_i, \Lambda\right) \mathrm{d}P_k \right|^2 \right\} . \tag{4.29}$$

The integral in Equation 4.29 can be written for the exponential distribution in closed form where P_k is the interval $[c, d)$:

$$\begin{aligned} \int_{P_k} p\left(x_i, \Lambda\right) \mathrm{d}P_k &= \int_c^d \Lambda\, \mathrm{e}^{-\Lambda\, x}\, \mathrm{d}x = -\mathrm{e}^{-\Lambda\, x}\Big|_c^d \\ &= \mathrm{e}^{-\Lambda\, c} - \mathrm{e}^{-\Lambda\, d} . \end{aligned} \tag{4.30}$$

The exponential curve fits to relative cluster and ray arrival data use the LS estimator for Λ and λ described in Equation 4.29 with the number of bins, N, chosen to be 100 to match the exponential fits for the SISO data. The LS estimate of the cluster arrival rate parameter, $1/\Lambda$, predicted from the ray tracing simulation was 18.94 ns as compared to the value of 16.8 ns estimated from measurements. The simulated data for ray arrival rate resulted in an LS estimate for $1/\lambda$ of 5.97 ns to be compared with the measurement estimate, 5.17 ns. The "best fit" exponential distributions for relative cluster arrival times and relative ray arrival times are shown comparing simulation results with SISO measurements in Figures 4.6 and 4.8 superimposed over the normalized histograms.

In both of the exponential Λ fits, the points of the normalized histogram are widely scattered around the LS curve. This scatter results from the relatively few samples available for relative cluster arrival times. In both the measurements and simulation data, there were 123 relative cluster times as compared to 2165 (measured) and 2029 (simulated) relative ray arrival times available for estimating λ. To reduce the noisy appearance of these fits, the plots can be represented as complementary

www.manaraa.com

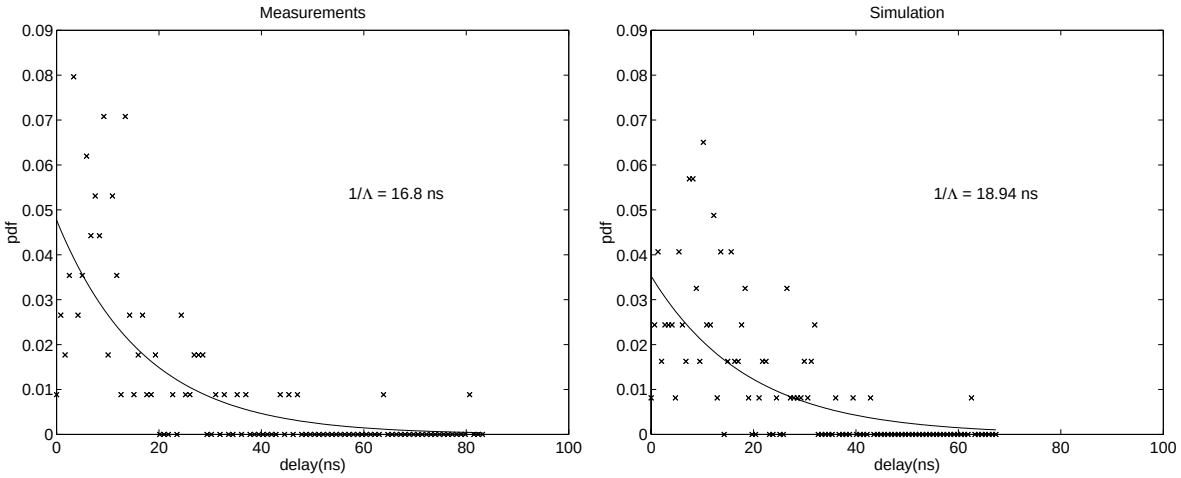

Figure 4.6: LS Exponential fit to relative cluster arrival times for measurements (left) and ray tracing simulation (right).

cumulative distributions which smooth the functions by integration:

$$1 - \sum_{k=0}^{\frac{i \cdot a}{N}} h_k \qquad i = 1, 2, \ldots, N \tag{4.31}$$

$$1 - \int_0^{\frac{i \cdot a}{N}} p\left(x, \Lambda\right) \mathrm{d}x \qquad i = 1, 2, \ldots, N \, .$$

These representations of both the Λ and λ fits are shown in Figures 4.8 and 4.9. It is hard to evaluate the quality of the fits when the complementary cdf's are shown on a linear scale, so they are depicted on semilog scales where the fitted distributions appear linearly and it is easier to observe the behavior of the data over several orders of magnitude. It is interesting to note how the estimate of λ varies as the number of bins, N, changes. Figure 4.10 shows the LS estimates of $1/\lambda$ for both measured and simulated ray arrival data as N varies from 10 to 300. At $N \approx 110$, the error metric reaches a minimum point for the measured data before rising again as the simulated data error continues to decrease. If we repeat the original estimates using

$N = 100$ bins in the histogram, the values are nearly identical: 5.86 ns (measured) and 5.87 ns (simulated). Because the simulated and measured parameters maintain their agreement over a range of N values, we can maintain confidence that

www.manaraa.com

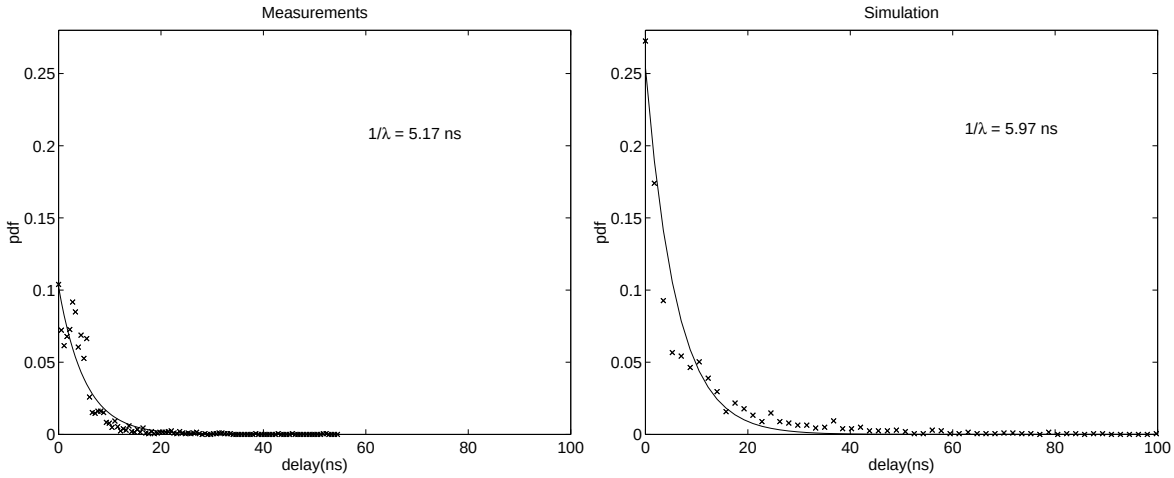

Figure 4.7: LS Exponential fit to relative ray arrival times for measurements (left) and ray tracing simulation (right).

the simulation is reasonably reproducing the observed model behavior. However, this provides a reminder of the subjectivity associated with LS curve fitting and it sensitivity to arbitrary estimator parameters. The estimates of $1/\Lambda$ are insensitive to N.

4.5.3 Amplitude Decay Rate Parameters

The Γ and γ parameters represent the exponential decay time constant in the envelope of the cluster and ray amplitude terms as described in Equation 4.2 and Figure 4.2. In order to make comparisons with estimates of these parameters taken from the SISO channel measurements in [2], we gathered ray and cluster amplitude data generated with the ray tracing software, normalized it, and performed the LS linear regression on the amplitude exponent. The most critical step in the process was to normalize the quantities used for the time and amplitude of the data points. The relative delay of each ray in the simulation was derived by dividing the total path length from transmitter to receiver and dividing by the speed of propagation. The arrival time and amplitude of an individual cluster was taken to be the time and amplitude of the first ray arrival identified within that cluster.

www.manaraa.com

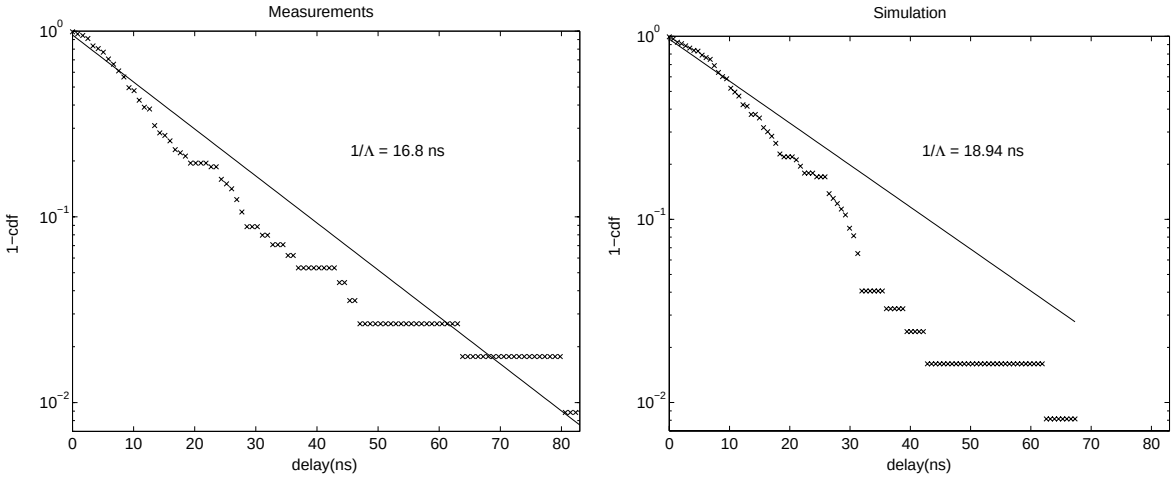

Figure 4.8: Log CCDF of relative cluster arrival times for measurements (left) and ray tracing simulation (right).

The cluster amplitude decay parameter, Γ, was estimated by collecting the cluster arrival times and amplitudes for a single simulation set. The cluster with the shortest path delay was taken as the reference with time t_0 and amplitude a_0. The remaining clusters were normalized in both time and amplitude by subtracting t_0 from their path delays and dividing their amplitudes by a_0. In a set the C clusters, this results in $(C-1)$ normalized time/amplitude data points. The data points were collected over all simulation sets, and we took the natural logarithm of the amplitudes to obtain their normalized exponential dependence with time. Γ was estimated by curve fitting the line (representing an exponential decay curve) to minimize the mean squared error resulting in an estimate of $\Gamma = 18.87$ ns.. The scatter plot of the simulated cluster amplitude versus time is shown with the Γ estimation curve fit in Figure 4.11.

An analogous estimation procedure was applied for the ray amplitude decay parameter, γ. For each cluster, the ray with the shortest path delay was taken as the reference with time t_0 and amplitude a_0. The subsequent rays arriving in the cluster were normalized in time by subtracting t_0 and in amplitude by dividing by a_0. These normalized points were aggregated over all clusters and all simulation sets, and the natural logarithm was applied to obtain the exponent of the normalized amplitude.

www.manaraa.com

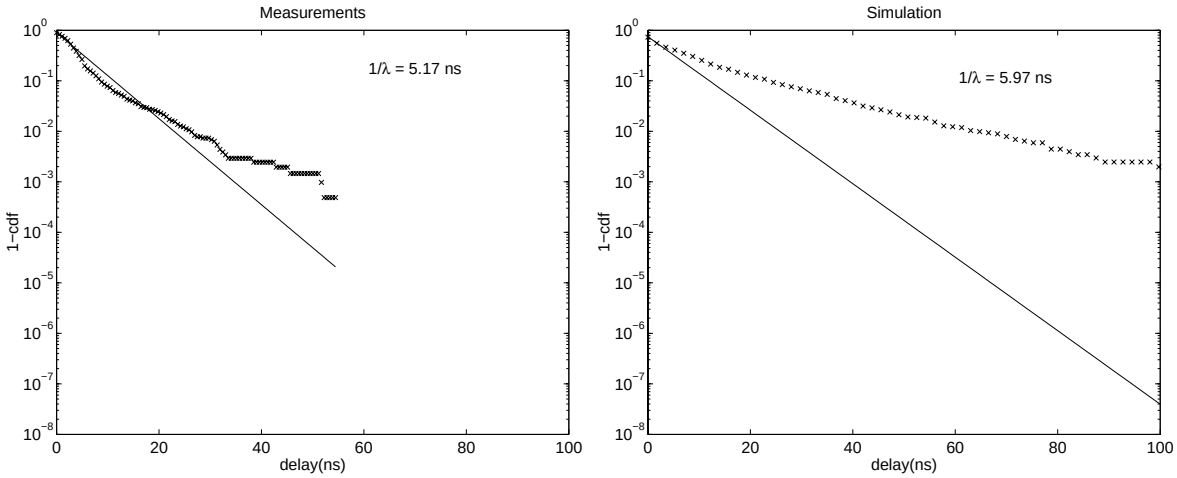

Figure 4.9: Log CCDF of relative ray arrival times for measurements (left) and ray tracing simulation (right).

The γ parameter was chosen to minimize the squared error of the exponential curve fit in log coordinates. The scatter plot of the simulated ray amplitude versus time is shown in Figure 4.12 along with the γ estimation curve fit.

The plot in [2] presenting the ray amplitude data and γ estimation used a 5 data point averaging filter to reduce apparent clutter in the figure. This has the additional effect of reducing the apparent scatter of the data around the fit. For consistent

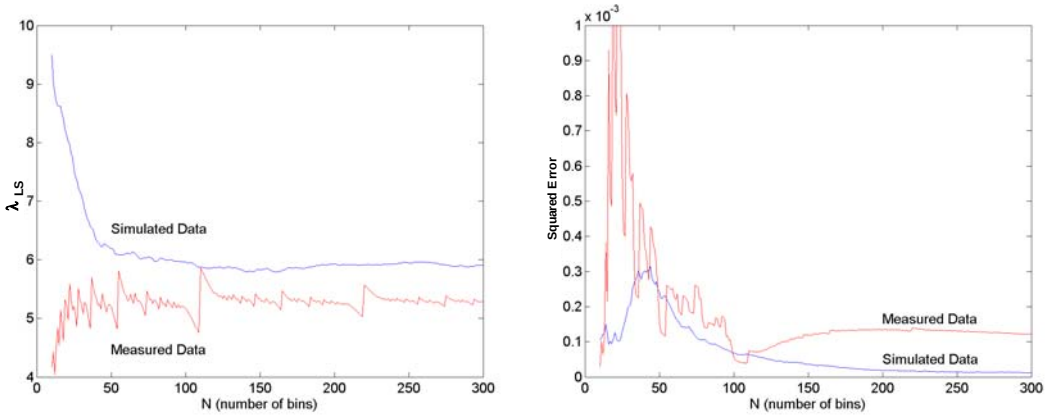

Figure 4.10: Estimates of $1/\lambda$ versus N (left) and LS metric (right).

www.manaraa.com

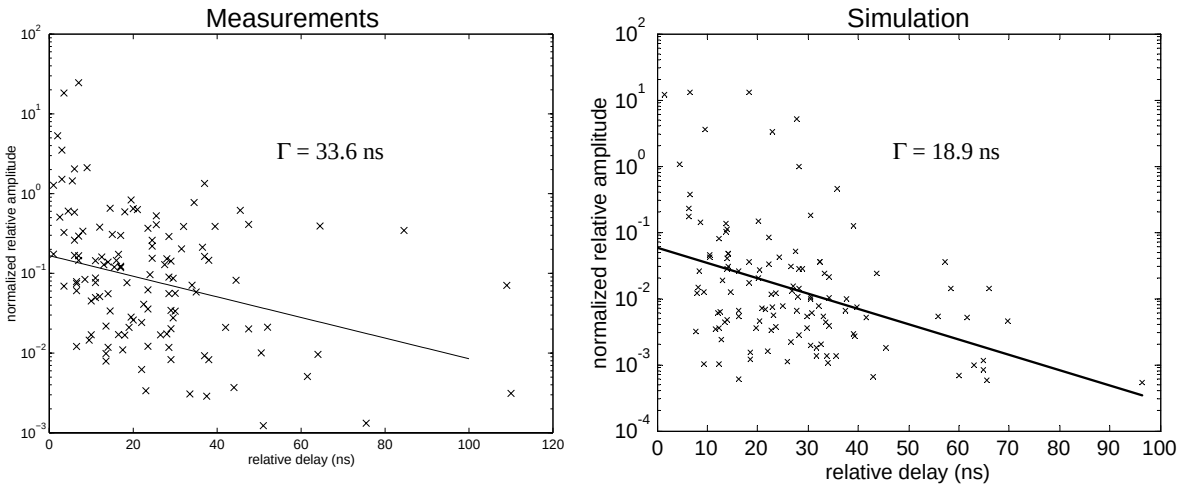

Figure 4.11: Plot of normalized cluster amplitude vs. relative delay for measurements (left) and ray tracing simulation (right).

comparison, a similar filter was applied to the data in Figure 4.12 to produce Figure 4.13 which is very consistent with the figure from the measured data.

The significant variance of the data around the fit lines in these plots is similar to that observed in the measurement data and reflects a low degree of confidence in the Γ and γ parameter estimates. One can also notice the artificially sharp lower threshold of the ray amplitudes shown in Figure 4.12 caused by the behavior of the software threshold parameter, which discards rays below a minimum power level from the simulation. Because of the inconsistent behavior of the power related controls of the ray tracing simulation software discussed in Section 3.4, the value of the amplitude decay time estimates may be somewhat discredited, but this may be less important than the agreement with the overall trend.

4.6 Comparison of Model Parameter Estimates

A summary comparing the model estimates derived from the ray tracing simulation data with those reported from the SISO measurements is shown in Table 4.2. The most exciting feature is the excellent agreement with the spatio-temporal parameters that describe the shape of the clusters predicted and measured in this

www.manaraa.com

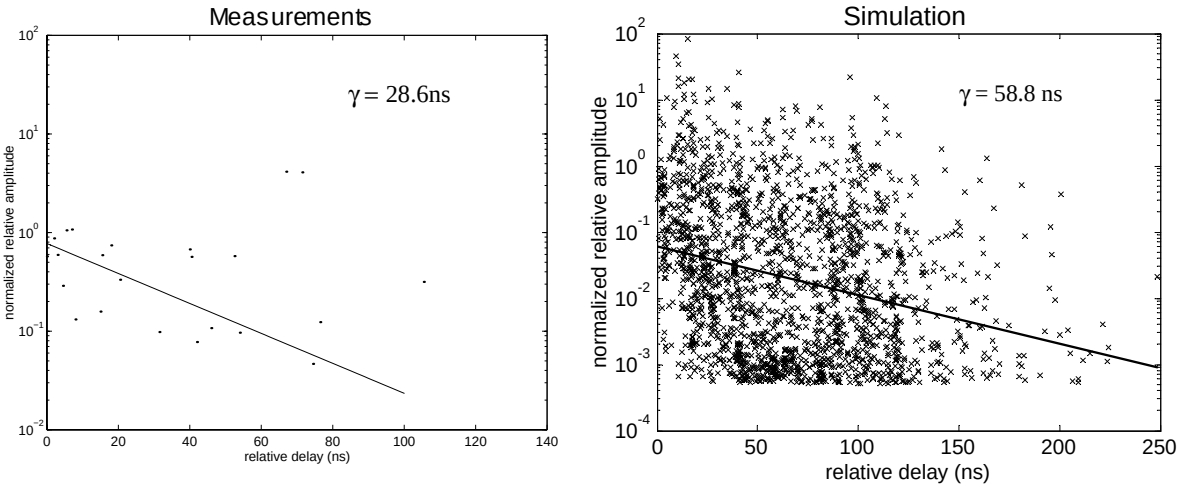

Figure 4.12: Plot of normalized ray amplitude vs. relative delay for measurements (left) and ray tracing simulation (right).

indoor environment. The width of the zero-mean Laplacian distribution for angular deviation within clusters is predicted within 10% of the measurement value. Likewise, the arrival rates for both clusters and individual rays are predicted within 15% of the observations. The quality of the agreement does not hold for the amplitude decay rate parameters. However, these parameters are estimated from data with very high

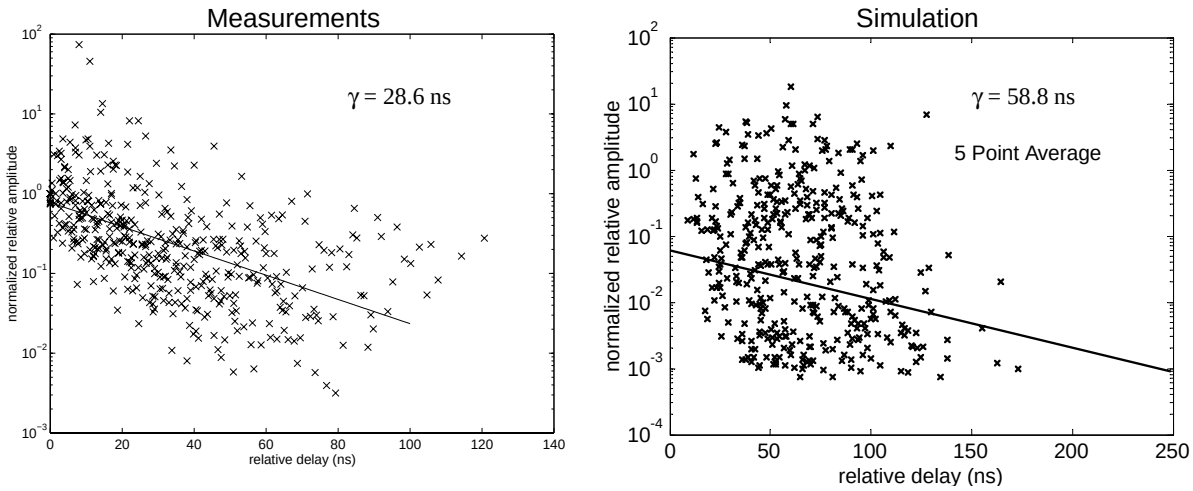

Figure 4.13: Plot of normalized ray amplitude vs. relative delay for measurements (left) and ray tracing simulation (right) with 5 point averaging filter applied.

www.manaraa.com

variance, and the artificially sharp minimum ray power threshold adds an effect to data that is not reflected in the measured data. Also the inconsistency of the ray tracing simulation's power related outputs casts doubt on the reliability of this information. Overall, the ray tracing simulation reproduces the previously observed space-time clustering structure in a reasonably consistent statistical sense. It does not yield ray-for-ray information that appears consistent with the CLEAN peaks detected in the measured data. We can also conclude that the integrity of the statistical clustering structure is dependent on a building geometry description that focuses on the locations of conductive scatterers more than on the simple bulk architechural shapes.

Table 4.2: Comparison of model parameter values from simulated and measured data.

Parameter	**Description**	**Measured Data**	**Simulated Data**
σ	Cluster Angular Standard Deviation	25.5°	**23.4°**
$1/\Lambda$	Cluster Arrival Rate	16.8 ns	**18.94 ns**
$1/\lambda$	Ray Arrival Rate	5.17 ns	**5.97 ns**
Γ	Cluster Amplitude Decay Rate	33.6 ns	**18.9 ns**
γ	Ray Amplitude Decay Rate	28.6 ns	**58.8 ns**

4.7 Conclusions

These results indicate that ray tracing is an effective tool for predicting the statistical behavior of indoor wireless environments. We did not observe a direct correlation one-to-one of individual predicted rays to arrivals detected in measured data, but there was strong similarity in the prediction of cluster structures to clusters

www.manaraa.com

measured in the channel response. The results obtained from ray tracing depend strongly on the level of detail used to describe the broadcast enviroment and upon the methods of grouping arrivals into clusters. We found that the description of the reflective surfaces in the environment were the most significant determinant of the behavior of the simulation. The ray tracing simulations were more useful for predicting the direction-related and time-related behavior of the channel than for describing its power-related characteristics.

www.manaraa.com

Chapter 5

Ray Model Feedback for Improved Capacity

In order for the transmitter to shape the transmitted symbols with optimal covariance for maximum information capacity, it must have some knowledge of the structure of the MIMO channel. The simplest way to obtain this information is to assume that the *uplink channel* and the *downlink channel* are reciprocal:

$$H_{down} = H_{up}^{H},$$

where we arbitrarily define the transmission from the transmitter to the receiver as the *downlink* and the transmission in the opposite direction as the *uplink*. The user at each endpoint of the link is able to estimate the current channel transfer matrix using a pre-arranged training sequence sent by its counterpart or some other method and uses this information to shape the covariance of its transmission appropriately. In cases where the channel is not reciprocal – for example, the case of a frequency division duplexing system where uplink and downlink transmissions are assigned to distinct frequencies with dissimilar MIMO transfer behavior – only the receiver is able to estimate the channel and must return some portion of this information to the transmitter.

We propose the following ray parameter feedback algorithm as an alternative to sending full H or subspace information in situations where the transmitter does not have the benefit of knowledge or estimates of the downlink channel transfer function. We begin with the assumption that the channel matrix can be reasonably represented

www.manaraa.com

by the ray synthesis model given by [64]

$$H = \sum_{i=1}^{N_{rays}} \mathbf{a}_{rcv}(\theta_i)\, \beta_i\, \mathbf{a}_{xmit}(\phi_i)^H \,, \tag{5.1}$$

where $\mathbf{a}_{xmit}(\phi) \in \mathbb{C}^{T\times 1}$ and $\mathbf{a}_{rcv}(\theta) \in \mathbb{C}^{R\times 1}$ are the steering vectors for the transmit and receive arrays and β_i is the complex ray gain for the i^{th} ray. The model can also be expressed conveniently in matrix form as

$$H = A_{rcv}\, B\, A_{xmit}^H \,, \tag{5.2}$$

where the following matrices are defined:

$$\begin{aligned} A_{rcv} &= [\, \mathbf{a}_{rcv}(\theta_1) \;\; \mathbf{a}_{rcv}(\theta_2) \;\; \cdots \;\; \mathbf{a}_{rcv}(\theta_N)\,] \,, \\ B &= \mathrm{diag}\{\, [\, \beta_1 \;\; \beta_2 \;\; \cdots \;\; \beta_N\,]\} \,, \\ A_{xmit} &= [\, \mathbf{a}_{xmit}(\phi_1) \;\; \mathbf{a}_{xmit}(\phi_2) \;\; \cdots \;\; \mathbf{a}_{xmit}(\phi_N)\,] \,. \end{aligned} \tag{5.3}$$

The receiver will estimate the parameters N_{rays} and $(\theta_i, \beta_i, \phi_i)$ for each ray and optionally k, the number of non-zero weighted eigenchannels in the waterfilling solution covariance. These are fed back to the transmitter where H is synthesized according to Equation 5.1 and the eigendecomposition of $H^H H$ performed in preparation for the waterfilling solution of the transmit MIMO beamformer for optimal capacity. If k is included, this amounts to N_{rays} complex values and $(2N_{rays}+1)$ real values or equivalently, $(4N_{rays}+1)$ real valued items. It is not necessary that the value N_{rays} be fed back as it is simply the cardinality of the set of ray parameters, $(\theta_i, \beta_i, \phi_i)$. Also, k may be treated as an integer rather than a floating-point value.

5.1 Considerations for Evaluating Performance

In the analysis of any sub-optimal feedback of covariance information for achieving MIMO capacity, we can never hope to exceed the upper bound stated by the waterfilling solution when the transmitter has full knowledge of H. Conversely, if the feedback process does not achieve an improvement over the blind transmitter solution for capacity, we would not view the extra effort of estimation and feedback to be

www.manaraa.com

worthwhile. These upper and lower bounds will be used to evaluate the performance of the ray parameter feedback algorithm.

Ideally, we would like to return the least possible amount of feedback information to the transmitter to impose the smallest possible overhead on link resources available for sending user data. A brute force feedback method might call for the receiver to send all of the complex entries of the channel matrix, $H \in \mathbb{C}^{R \times T}$, representing $2RT$ real scalars of information. The transmitter would then compute the eigendecomposition of $H^H H$ and form the MIMO beamformer using the waterfilling solution. Alternatively, if sufficient computational resources are available to the receiver, the quantity of feedback information may be reduced by sending only the k non-zero gain factors and the associated eigenvectors, resulting in k real values and kT complex values where k is typically less than T for all but the highest values of SNR. This subspace information would require $k\,(2\,T+1)$ real valued feedback items and allow the transmitter to form the optimum MIMO beamformer without significant additional calculation. It is hoped that the feedback methods described here will achieve significant improvements upon the uninformed channel capacity using less than the full amount of feedback (ie. $(4N_{rays}+1) \ll k\,(2\,T+1)$).

5.2 Ray Parameter Estimation

To identify the feedback information, we need to estimate the number of discrete rays present in the channel, N_{rays}, and the parameters to best describe them in the model $(\phi_i, \beta_i, \theta_i)$ for $i = 1, \ldots, N_{rays}$. Assuming that we start with either knowledge of the MIMO channel transfer matrix, H, or an estimate of it $\hat{H}$, we estimate the number of rays by minimizing a metric function between the channel matrix synthesized from the model parameter estimates, H_{model}, and our information about the channel, H or $\hat{H}$, as shown in Figure 5.1. We consider two metric functions, Least

www.manaraa.com

Squares and Information Capacity, as defined by:

$$f_{LS}(H, H_{model}) = \sum_{i=1}^{R}\sum_{j=1}^{T} |H_{model}(i,j) - H(i,j)|^2$$
$$= \|H_{model}(i,j) - H(i,j)\|_F^2 \tag{5.4}$$

$$f_{cap}(H, H_{model}) = C(H) - C(H_{model}) . \tag{5.5}$$

Where information capacity is the primary measure used in this research, the f_{cap} metric would seem to be the best measure of how well the ray-parameter feedback represents the information necessary to approximate the transmitted signal covariance for optimal capacity. However, this requires that the capacity calculations be performed for every value of N_{rays}, rather than once at the end of the N_{rays} iteration to calculate the capacity achieved by the parameters as selected by some other metric. For this reason, the f_{LS} metric was preferred for the bulk of the simulations presented. In cases where the transmitter was assumed to have knowledge of the channel state information (CSI), H in Equation 5.4 represented the known channel matrix. In cases where a training-based channel estimation process was simulated, H was replaced with $\hat{H}$ estimated from the known training symbol sequence. To provide a penalty for increasing the order of the model, the metric value of H_{model} generated with a larger number of rays was required to be less than 90% of the metric value of H_{model} produced with fewer rays. Otherwise, the parameter set with fewer rays was selected. By this process, a higher order model of the channel matrix must provide significant improvement in the metric to justify the increased amount of feedback information required.

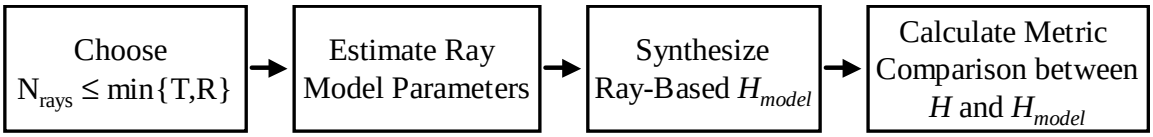

Figure 5.1: Metric calculation for model parameters as a function of N_{rays}

www.manaraa.com

Once a value of N_{rays} is selected, the ray model parameters are estimated in a four step process:

- estimate angles of departure from transmitter, ϕ_i,
- estimate angles of arrival at receiver, θ_i,
- determine the pairwise correspondence between ϕ_i and θ_i,
- estimate the complex ray gains, β_i.

In this research, we investigate several methods of Direction of Arrival estimation. First, the MIMO beamscan method is a 2-dimensional application of conventional beam steering. Second, we tested two 1-dimensional subspace-based Direction of Arrival estimation methods: MUSIC and 1-D ESPRIT. These methods estimate transmit ray angles and receive ray angles separately which makes it necessary to determine the pairwise correspondence of transmit rays to receive rays in a subsequent step. Our pairwise matching technique is based on [65]. Finally, we also present an alternative 2-dimensional subspace Direction of Arrival estimator, 2-D Unitary ESPRIT, that estimates paired transmit and receive ray angles jointly for a Uniform Linear Array (ULA) configuration.

5.2.1 MIMO Beamscan

Our MIMO beamscan algorithm projects the channel transfer matrix, $\hat{H}$, onto conventional beam steering vectors for transmit and receive arrays while sweeping the beams through the range of directions on both arrays. The ray angle estimator searches for peaks in the magnitude of the 2-D beamformer output:

$$\hat{P}_{bf}(\phi,\theta) = |\, \mathbf{a}_{xmit}\,(\phi)^H\, \hat{H}\, \mathbf{a}_{rcv}\,(\theta)\,|\,, \tag{5.6}$$

where $\mathbf{a}_{xmit}(\phi) \in \mathbb{C}^{T\times 1}$ and $\mathbf{a}_{rcv}(\theta) \in \mathbb{C}^{R\times 1}$ are the steering vectors for the transmit and receive arrays as used in the ray synthesis of the channel matrix in Equation 5.1. The operator $|\cdot|$ indicates here the magnitude of a complex scalar. If the

www.manaraa.com

values of both ϕ and θ are drawn from a discrete set of values, $\{\psi_1, \psi_2 \ldots, \psi_k\}$, which samples the angular space in an appropriate way, we can express the beamformer output in terms of the matrices $A_{xmit} = [\ \mathbf{a}_{xmit}(\phi_1) \cdots \mathbf{a}_{xmit}(\phi_k)\ ]$ and $A_{rcv} = [\ \mathbf{a}_{rcv}(\theta_1) \cdots \mathbf{a}_{rcv}(\theta_k)\ ]$ as

$$\hat{P}_{bf} = |\, A_{xmit}^H \, \hat{H} \, A_{rcv} \,|\,, \tag{5.7}$$

where $\hat{P}_{bf}$ is a $k \times k$ matrix and $|\cdot|$ represents the complex magnitude of each entry. The locations of local maxima within $\hat{P}_{bf}$ are mapped back to angles using the ordered set of $\{\psi_1, \psi_2 \ldots, \psi_k\}$. For example, if $\hat{P}_{bf}(i, j)$ is a local maximum, we conclude that there is a MIMO ray pair with $\phi = \psi_i$ and $\theta = \psi_j$.

5.2.2 MUSIC

The MUSIC (**Mu**ltiple **Si**gnal **C**lassification) algorithm was invented by Schmidt [66] and independently by Bienvenu and Kopp [67], as noted by VanTrees in [68]. Our presentation here draws significantly from the latter reference.

The MUSIC algorithm for signal direction estimation assumes that there are D plane waves incident on the sensor array at angles $\theta_1, \ldots, \theta_D$ and that D is less than the number of sensors, N. The covariance of the received signal is defined in terms of the array geometry and the covariance of the transmitted signals as

$$R_x = A(\boldsymbol{\theta})\, R_s\, A(\boldsymbol{\theta})^H + \sigma_n^2 I\,, \tag{5.8}$$

where $A(\boldsymbol{\theta}) = [\,\mathbf{a}(\theta_1)\ \mathbf{a}(\theta_2)\ \cdots\ \mathbf{a}(\theta_D)\,]$ is composed of D steering vectors for the array, R_s is the covariance of the transmitted signals, and σ_n^2 is the uncorrelated noise power. R_x is often referred to as the *spectral matrix* of the received signals. The columns of $A(\boldsymbol{\theta})$ span a D dimensional *signal subspace* that contains all of the signal energy. Under the assumption that R_s is full rank, the algorithm separates R_x into the D dimensional signal subspace and a $(N - D)$ dimensional *noise subspace* using eigendecomposition. In terms of its eigenvalues, λ_i, and eigenvectors, $\mathbf{u}_i$, R_x can be

www.manaraa.com

expressed as

$$R_x = \sum_{i=1}^{N} \lambda_i \, \mathbf{u}_i \, \mathbf{u}_i^H \quad \text{or} \quad R_x = U \, \Lambda \, U^H \, , \tag{5.9}$$

where $U = [\, \mathbf{u}_1 \; \mathbf{u}_2 \; \cdots \; \mathbf{u}_N \,]$ and $\Lambda = \text{diag}\{[\, \lambda_1 \; \lambda_2 \; \cdots \; \lambda_N \,]\}$. For convenience, it is assumed that the λ_i's are arranged in decreasing magnitude so that

$$\lambda_i \; \geq \; \lambda_2 \; \geq \cdots \geq \lambda_D > \lambda_{D+1} = ... = \lambda_N = \sigma_n^2 \, .$$

This allows us to define the bases for the signal and noise subspaces in terms of partitions of U :

$$U_S = [\, \mathbf{u}_1 \; \mathbf{u}_2 \; \cdots \; \mathbf{u}_D \,] \quad \text{and} \quad U_N = [\, \mathbf{u}_{D+1} \; \mathbf{u}_{D+2} \; \cdots \; \mathbf{u}_N \,] \, . \tag{5.10}$$

As a result of the composition of the signal subspace, all of the basis vectors in U_S can be formed by a unique linear combination of the steering vectors in $A(\boldsymbol{\theta})$, as in

$$\mathbf{u}_i = [\, \mathbf{a}(\theta_1) \; \mathbf{a}(\theta_2) \; \cdots \; \mathbf{a}(\theta_D) \,] \begin{bmatrix} c_{i,1} \\ c_{i,2} \\ \vdots \\ c_{i,D} \end{bmatrix} = A(\boldsymbol{\theta}) \; \mathbf{c}_i \qquad i = 1, 2, \ldots, D \, . \tag{5.11}$$

This allows us to express U_S as a full-rank transformation of $A(\boldsymbol{\theta})$,

$$U_S = A(\boldsymbol{\theta}) \; [\, \mathbf{c}_1 \; \mathbf{c}_2 \; \cdots \; \mathbf{c}_D \,] = A(\boldsymbol{\theta}) \; C \, . \tag{5.12}$$

Because the signal subspace is orthogonal to the noise subspace, any vector in the signal subspace will have zero projection onto any vector in the noise subspace. This provides the essential result for most subspace-based processing: that the steering vectors projected onto the noise subspace have zero norm:

$$\| \, \mathbf{a}(\theta_i)^H \; U_N \, \|^2 = \mathbf{a}(\theta_i)^H U_N \, U_N^H \; \mathbf{a}(\theta_i) = 0 \qquad i = 1, 2, \ldots, D \, . \tag{5.13}$$

In situations where the received signal covariance, R_x, is not known, we rely on an estimate $\hat{R}_x$, and use its eigendecomposition, $\hat{R}_x = \hat{U} \hat{\Lambda} \hat{U}^H$, to estimate the signal and noise subspaces:

$$\hat{U}_S = [\, \hat{\mathbf{u}}_1 \; \hat{\mathbf{u}}_2 \; \cdots \; \hat{\mathbf{u}}_D \,] \quad \text{and} \quad \hat{U}_N = [\, \hat{\mathbf{u}}_{D+1} \; \hat{\mathbf{u}}_{D+2} \; \cdots \; \hat{\mathbf{u}}_N \,] \, . \tag{5.14}$$

www.manaraa.com

Frequently, a quantity called the *MUSIC spectrum* is defined as a function of θ in terms of the squared norm of a beamsteering vector projected onto all of the basis vectors of the noise subspace, $\hat{U}_N$:

$$P(\theta) = \frac{1}{\sum_{i=D+1}^{N} \| \mathbf{a}(\theta)^H \hat{\mathbf{u}}_i \|^2} = \frac{1}{\mathbf{a}(\theta_i)^H \hat{U}_N \hat{U}_N^H \mathbf{a}(\theta_i)} . \tag{5.15}$$

In the absence of estimation error, $P(\theta)$ is infinite when $\theta = \theta_i$ $(i = 1, 2, \ldots, D)$ because the $a(\theta_i)$'s lie in the signal subspace, not the noise subspace. In practice, the θ_i's are determined by the D largest peaks in $P(\theta)$. One significant downside of the MUSIC algorithm is the computational burden of evaluating $P(\theta)$ at many sampling values of θ.

The algorithm described so far is often referred to as *spectral* MUSIC and is applicable to any array configuration. Other MUSIC algorithms have extended this general case by using specific structure of the arrays. For example, *root* MUSIC can be applied to a Uniform Linear Array and expresses the projection onto the noise subspace as a polynomial in the complex z-plane. Angles are identified by finding the roots of the polynomial and choosing the D roots inside the unit circle and closest to the unit circle. Root MUSIC is able to remove the effect of estimation error that produces displacement of the roots in the radial direction because it determines the θ_i's using only the angular component of the D root locations. Common extensions to root music include (1) *forward-backward root* MUSIC which improves the estimate of the spectral matrix by exploiting conjugate centro-symmetry to average out part of the estimation errors and (2) *unitary* root MUSIC which performs transformations on the spectral matrix to represent it with purely real entries to achieve the same performance as forward-backward root music with significant computational savings [68].

In this research, the received signal covariance estimate, $\hat{R}_x$, is formed from the channel transfer matrix, H, or its estimate $\hat{H}$ and using the assumption that the transmitted signals are uncorrelated. To estimate the angles of arrival at the receiver,

www.manaraa.com

we use the covariance $\hat{R}_{rcv} = H\,H^H$ which leads to signal and noise subspaces derived from the left singular vectors of H. Similarly, to estimate the angles of departure from the transmitter, we use the reciprocal channel, H^H to compose the covariance $\hat{R}_{xmit} = H^H H$ which leads to subspaces composed of the right singular vectors of H. Table 5.2.2 shows the MUSIC algorithm quantities in terms of the singular value decomposition of $H = U\Sigma\,V^H$. Note that the value of D is equal to our choice of N_{rays} as described in Section 5.2.

Table 5.2.2 - Comparison of MUSIC algorithm quantities used in receive angle and transmit angle estimation

Algorithm Quantity	Receive Angle Estimation	Transmit Angle Estimation
Channel Matrix	$H = U\Sigma\,V^H$	$H^H = V\Sigma\,U^H$
R_x	$HH^H = U\Sigma^2 U^H$	$H^H H = V\Sigma^2 V^H$
Signal Subspace	$[\,\mathbf{u}_1\ \mathbf{u}_2\ \cdots\ \mathbf{u}_D\,]$	$[\,\mathbf{v}_1\ \mathbf{v}_2\ \cdots\ \mathbf{v}_D\,]$
Noise Subspace	$[\,\mathbf{u}_{D+1}\ \mathbf{u}_{D+2}\ \cdots\ \mathbf{u}_N\,]$	$[\,\mathbf{v}_{D+1}\ \mathbf{v}_{D+2}\ \cdots\ \mathbf{v}_N\,]$
$P(\theta)$	$\dfrac{1}{\mathbf{a}_{rcv}(\theta_i)^H U_N\,U_N^H\ \mathbf{a}_{rcv}(\theta_i)}$	$\dfrac{1}{\mathbf{a}_{xmit}(\theta_i)^H V_N\,V_N^H\ \mathbf{a}_{xmit}(\theta_i)}$

By selecting the $D = N_{rays}$ peaks of $P_{rcv}(\theta)$ and $P_{xmit}(\theta)$ evaluated at a reasonably sampled set of $\theta \in [-90, 90\,]$, we have estimated the set of values for receive and transmit angles, but these sets do not have any ray angle pairing information or complex gains associated with them. At this point in the estimation process, we would proceed with the Transmit-Receive Ray Pairing processing as described in Section 5.2.4.

www.manaraa.com

5.2.3 1-D ESPRIT

The ESPRIT (**E**stimation of **S**ignal **P**arameters via **R**otational **I**nvariance **T**echniques) algorithm was derived by Roy in his doctoral dissertation [69] and several other publications as noted by VanTrees in [68] and Swindlehurst in [70]. Both of the latter references outline the derivation and present a step-by-step process for estimating angles of arrival for plane waves on a sensor array. The following development incorporates significant portions of material from these references.

ESPRIT is applicable for arrays which can be decomposed into two (or more) identical subarrays which are displaced from each other by a constant translation vector, $\mathbf{\Delta}$. It is permissible for array elements to be members of both subarrays when the subarrays are overlapping. For an array with N total sensor elements and m members in each subarray, we can conclude that $N \leq 2m$ with equality representing cases with non-overlapping subarrays. The algorithm depends on the assumption of D plane waves incident on the sensor array at angles $\theta_1, \ldots, \theta_D$ and that D is less than the number of sensors in each subarray, m.

Starting with the narrowband array model from section 2.1, the output of the array can be modeled in terms of the array manifold matrix composed of D steering vectors for the array, $A(\boldsymbol{\theta}) = [\, \mathbf{a}(\theta_1)\ \mathbf{a}(\theta_2)\ \cdots\ \mathbf{a}(\theta_D)\,]$, as

$$\mathbf{x} = A(\boldsymbol{\theta})\,\mathbf{s} + \mathbf{n}\,. \tag{5.16}$$

This results in the same expression for the received signal covariance used in equation 5.8 in the previous section:

$$R_x = A(\boldsymbol{\theta})\,R_s\,A(\boldsymbol{\theta})^H + \sigma_n^2 I\,, \tag{5.17}$$

where R_s is the covariance of the transmitted signals and σ_n^2 is the uncorrelated noise power. The columns of $A(\boldsymbol{\theta})$ span a D dimensional *signal subspace* that contains all of the signal energy. The algorithm separates R_x into the D dimensional signal subspace and a $(N-D)$ dimensional *noise subspace* using an eigendecomposition. In

www.manaraa.com

terms of its eigenvalues, λ_i, and eigenvectors, $\mathbf{u}_i$, R_x can be expressed as

$$R_x = \sum_{i=1}^{N} \lambda_i \, \mathbf{u}_i \, \mathbf{u}_i^H \quad \text{or} \quad R_x = U \, \Lambda \, U^H \, , \tag{5.18}$$

where $U = [\, \mathbf{u}_1 \; \mathbf{u}_2 \; \cdots \; \mathbf{u}_N \,]$ and $\Lambda = \text{diag}\{[\, \lambda_1 \; \lambda_2 \; \cdots \; \lambda_N \,]\}$. For convenience, it is assumed that the λ_i's are arranged in decreasing magnitude so that

$$\lambda_i \; \geq \; \lambda_2 \; \geq \cdots \geq \lambda_D > \lambda_{D+1} = ... = \lambda_N = \sigma_n^2 \, .$$

This allows us to define the bases for the signal and noise subspaces in terms of partitions of U :

$$U_S = [\, \mathbf{u}_1 \; \mathbf{u}_2 \; \cdots \; \mathbf{u}_D \,] \quad \text{and} \quad U_N = [\, \mathbf{u}_{D+1} \; \mathbf{u}_{D+2} \; \cdots \; \mathbf{u}_N \,] \, . \tag{5.19}$$

The subarrays are mathematically identified by use of selection matrices, J_1 and J_2, operating on the array manifold matrix for the total array as in

$$A_1 = J_1 \, A(\boldsymbol{\theta}) \quad \text{and} \quad A_2 = J_2 \, A(\boldsymbol{\theta}) \, . \tag{5.20}$$

Some examples of subarrays selected from a uniform linear array are shown on page 1172 of [68] with their associated selection matrices, J. The ESPRIT algorithm exploits the shift invariance property inherent in this special array structure:

$$A_2 = A_1 \, \Phi \, . \tag{5.21}$$

The matrix Φ is a unitary diagonal matrix defined in terms of the angles of arrival by

$$\Phi = \text{diag}\{[\, \phi_1 \; \phi_2 \; \cdots \; \phi_D \,]\} \, , \tag{5.22}$$

where

$$\phi_i = \exp\{-j \, 2\pi \Delta \sin\theta_i / \lambda\} \quad i = 1, \ldots, D \tag{5.23}$$

uses the wavelength of the narrowband signal, λ, and the subarray separation distance, $\Delta = |\boldsymbol{\Delta}|$. Because of the shift structure inherent in $A(\boldsymbol{\theta})$, ESPRIT is able to estimate Φ, and consequently the angles of arrival $\theta_1, \ldots, \theta_D$, *without* knowledge of the reference array manifold matrix, A_1.

www.manaraa.com

Assuming that the source covariance matrix, R_s, is full rank, the D signal subspace eigenvectors U_S span the same subspace as the columns of $A(\boldsymbol{\theta})$, which implies that

$$U_S = A(\boldsymbol{\theta})\, T \tag{5.24}$$

for some full-rank matrix $T \in \mathbb{C}^{D \times D}$. In other words, the signal subspace eigenvectors are linear combinations of the array manifold vectors of the D sources.

Selecting the *subarray signal subspaces* using J_1 and J_2 and substituting from equation 5.24 gives

$$U_{S1} = J_1\, U_S = J_1\, A(\boldsymbol{\theta})\, T = A_1\, T \tag{5.25}$$

and

$$U_{S2} = J_2\, U_S = J_2\, A(\boldsymbol{\theta})\, T = A_2\, T\,. \tag{5.26}$$

The goal is to express U_{S2} in terms U_{S1} to allow direct exploitation of the shift invariance relation between the two subarray signal subspaces. This can be done by solving equation 5.25 for A_1 which yields

$$A_1 = U_{S1}\, T^{-1}\,, \tag{5.27}$$

and substituting into the shift invariance relation in equation 5.21 to obtain the following expression for A_2 :

$$A_2 = A_1\, \Phi = U_{S1}\, T^{-1}\, \Phi\,. \tag{5.28}$$

Using this last expression as a substitution for A_2 in equation 5.26, leads to a mapping which relates the subspace spanned by U_{S2} to the subspace spanned by U_{S1} given by

$$U_{S2} = A_2\, T = A_1\, \Phi\, T = U_{S1}\, (\, T^{-1}\, \Phi\, T\,) = U_{S1} \Psi\,, \tag{5.29}$$

where linear operator $\Psi = T^{-1}\, \Phi\, T$ has been defined. This equation expresses the same invariance relationship as $A_2 = A_1\, \Phi$ now in terms of the signal subspace eigenvectors. We can conclude from this that U_{S1} and U_{S2} span an identical subspace and that the matrix Ψ has eigenvalues identical to the entries of Φ which uniquely specify the angles of arrival if $m > D$ and $\Delta < \lambda/2$.

www.manaraa.com

In practice, the sample covariance $\hat{R}_x$ must be used in place of R_x, which results in estimates for the subarray signal subspace eigenvectors, $\hat{U}_{S1}$ and $\hat{U}_{S2}$, which will not exactly satisfy the shift invariance relationship in equation 5.29. Consequently, there is no matrix Ψ that can exactly map the columns of $\hat{U}_{S1}$ onto the columns of $\hat{U}_{S2}$. The best we can do at this point is to find $\hat{\Psi}$ which minimizes the difference between $\hat{U}_{S2}$ and $\hat{U}_{S1}\,\hat{\Psi}$ in some least-squares sense.

If we solve equation 5.29 using ordinary least-squares, we seek to minimize the Frobenius norm distance between $\hat{U}_{S2}$ and $\hat{U}_{S1}\,\hat{\Psi}$ as in

$$\begin{aligned} \hat{\Psi}_{LS} &= \arg\min_{\Psi} \left\{ \| \hat{U}_{S2} - \hat{U}_{S1}\,\Psi \|_F^2 \right\} \\ &= \arg\min_{\Psi} \left\{ \mathrm{tr} \left\{ [\,\hat{U}_{S2} - \hat{U}_{S1}\,\Psi\,]^H\,[\,\hat{U}_{S2} - \hat{U}_{S1}\,\Psi\,] \right\} \right\} . \end{aligned} \tag{5.30}$$

This leads to the pseudoinverse solution of

$$\hat{\Psi}_{LS} = \hat{U}_{S1}^{\dagger}\,\hat{U}_{S2} = [\hat{U}_{S1}^H\,\hat{U}_{S1}]^{-1}\,\hat{U}_{S1}^H\,\hat{U}_{S2} . \tag{5.31}$$

The steps in the LS-ESPRIT algorithm can be summarized as follows:

1. Perform the eigendecomposition of $\hat{R}_x$ to obtain $\hat{U}_S$,
2. Find $\hat{U}_{S1} = J_1\,\hat{U}_S$ and $\hat{U}_{S2} = J_2\,\hat{U}_S$,
3. Find $\hat{\Psi}_{LS} = \hat{U}_{S1}^{\dagger}\,\hat{U}_{S2}$,
4. Find the eigenvalues of $\hat{\Psi}_{LS}$: $\hat{\lambda}_1, \hat{\lambda}_2, \ldots, \hat{\lambda}_D$,
5. Use equation 5.23 to find the angle estimates, $\hat{\theta}_i = \arcsin\left\{ \arg\{\lambda_i\} \frac{\lambda}{2\pi\,\Delta} \right\}$.

As an alternative to the ordinary LS solution for $\hat{\Psi}$, a total least squares (TLS) criterion may be used. This is probably more appropriate given that the estimates of both $\hat{U}_{S1}$ and $\hat{U}_{S2}$ contain errors, whereas the LS solution assumes that $\hat{U}_{S2}$ is error-free. The TLS solution is described in Section 12.3 of [71] and Section 7.7 of [72]. VanTrees states that LS-ESPRIT and TLS-ESPRIT have the same asymptotic variance as the data available to estimate $\hat{R}_x$ goes to infinity, but that TLS-ESPRIT generally has better threshold behavior [68]. Our presentation follows that of [70].

www.manaraa.com

The TLS solution for $\hat{\Psi}$ may be stated as follows:

Given the subspace estimates $\hat{U}_{S1}$ and $\hat{U}_{S2}$, find a $D \times D$ matrix $\hat{\Psi}$ and $m \times D$ matrices X and Y to minimize

$$\|X\|_F^2 + \|Y\|_F^2$$

subject to

$$(\,\hat{U}_{S1} + X\,)\,\hat{\Psi} = \hat{U}_{S2} + Y\ .$$

As shown in the references above, the TLS solution to this minimization is obtained from

$$\hat{\Psi}_{TLS} = -V_{12}\,V_{22}^{-1}\ , \tag{5.32}$$

where

$$V = \begin{bmatrix} V_{11} & V_{12} \\ V_{21} & V_{22} \end{bmatrix} \tag{5.33}$$

is the matrix of right singular vectors taken from the singular value decomposition of

$$\bar{U} \triangleq \left[\hat{U}_{S1} \,\vdots\, \hat{U}_{S2}\right] = U\,\Sigma\,V^H\ , \tag{5.34}$$

or from the eigendecomposition of

$$\bar{U}^H\,\bar{U} = \begin{bmatrix} V_{11} & V_{12} \\ V_{21} & V_{22} \end{bmatrix} \Lambda \begin{bmatrix} V_{11} & V_{12} \\ V_{21} & V_{22} \end{bmatrix}^H\ . \tag{5.35}$$

The steps of the TLS-ESPRIT algorithm can be summarized:

1. Perform the eigendecomposition of $\hat{R}_x$ to obtain $\hat{U}_S$,
2. Find $\hat{U}_{S1} = J_1\,\hat{U}_S$ and $\hat{U}_{S2} = J_2\,\hat{U}_S$,
3. Compute the eigendecomposition of $\bar{U}^H\,\bar{U}$ and set $[\,V_{12}^T \;\; V_{22}^T\,]^T$ equal to the eigenvectors associated with the D smallest eigenvalues,
4. Find $\hat{\Psi}_{TLS} = -V_{12}\,V_{22}^{-1}$,

www.manaraa.com

5. Find the eigenvalues of $\hat{\Psi}_{TLS}$, $\hat{\lambda}_1, \hat{\lambda}_2, \ldots, \hat{\lambda}_D$,

6. Use equation 5.23 to find the angle estimates, $\hat{\theta}_i = \arcsin\left\{\arg\{\lambda_i\}\frac{\lambda}{2\pi\Delta}\right\}$.

In addition to the LS-ESPRIT and TLS-ESPRIT algorithms presented here, there are several other versions of ESPRIT similar to those mentioned earlier for MUSIC. *Forward-Backward* or FB-ESPRIT can be used in the special case of arrays with conjugate centro-symmetry to average out part of the estimation errors. *Unitary* ESPRIT performs the FB averaging with particular unitary transformations allowing the eigendecomposition calculations to be performed on purely real matrices. This realizes performance equivalent to FB-ESPRIT but with significant computation savings.

In this research, the received signal covariance estimate, $\hat{R}_x$, is formed from the channel transfer matrix, H, or its estimate $\hat{H}$ and using the assumption that the transmitted signals are uncorrelated. To estimate the angles of arrival at the receiver, we use the covariance $\hat{R}_{rcv} = H\,H^H$ which leads to signal and noise subspaces derived from the left singular vectors of H. Similarly, to estimate the angles of departure from the transmitter, we use the reciprocal channel, H^H to compose the covariance $\hat{R}_{xmit} = H^H H$ which leads to subspaces composed of the right singular vectors of H. LS-ESPRIT is used for simplicity. We have performed simulations with maximally overlapping subarrays spaced by $\lambda/4$ as shown in Figure 5.2 and with 8 element maximally overlapping subarrays spaced by $\lambda/2$. In the second case the subarray separation distance is 2Δ by comparison to the figure. When the subarray spacing is less than $\lambda/2$ it becomes possible for the argument of the $\sin^{-1}(\cdot)$ function to have magnitude greater than one. This results in imaginary values for angles, which is not physically interpretable. In these cases, these estimates were simply discarded and the processing proceeded with the remaining real estimates. Table 5.2.3 shows the ESPRIT algorithm quantities in terms of the singular value decomposition of $H = U\Sigma V^H$. Note that the value of D is equal to our choice of N_{rays} as described in Section 5.2.

www.manaraa.com

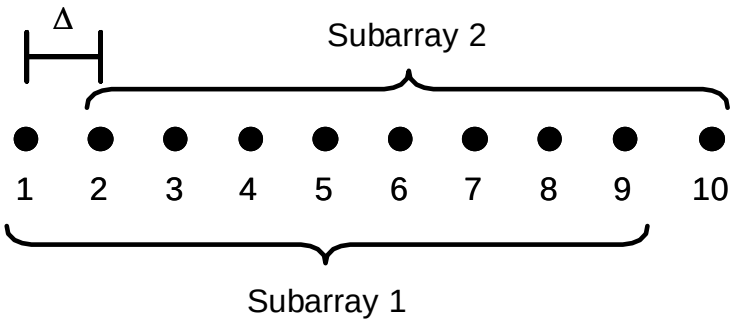

Figure 5.2: Maximally overlapping 9-element subarrays for 10-element ULA

Table 5.2.3 - Comparison of 1-D ESPRIT algorithm quantities used in receive Angle and transmit angle estimation

Algorithm Quantity	Receive Angle Estimation	Transmit Angle Estimation
Channel Matrix	$H = U\Sigma V^H$	$H^H = V\Sigma U^H$
R_x	$HH^H = U\Sigma^2 U^H$	$H^H H = V\Sigma^2 V^H$
Signal Subspace	$[\,\mathbf{u}_1\ \mathbf{u}_2\ \cdots\ \mathbf{u}_D\,]$	$[\,\mathbf{v}_1\ \mathbf{v}_2\ \cdots\ \mathbf{v}_D\,]$
J_1 Selection Matrix	$[\,I_{9\times 9}\ \vdots\ \mathbf{0}_{9\times 1}\,]$	$[\,I_{9\times 9}\ \vdots\ \mathbf{0}_{9\times 1}\,]$
J_2 Selection Matrix	$[\,\mathbf{0}_{9\times 1}\ \vdots\ I_{9\times 9}\,]$	$[\,\mathbf{0}_{9\times 1}\ \vdots\ I_{9\times 9}\,]$

5.2.4 Transmit-Receive Ray Pairing and Ray Gain Estimation

Once we have estimates of the sets of transmit angles, ϕ_i, and receive angles θ_i, we need to establish the pair-wise correspondence between the two sets and estimate the complex gain factors that best approximate the channel transfer matrix, H, as a weighted sum of outer products as described in the ray synthesis channel model in Equation 5.2. We use the ad hoc successive removal method proposed by Jeffs and Wallace in [65] and follow closely the development outlined there. For compactness

www.manaraa.com

of notation, we will adopt the following notation used by Jeffs and Wallace:

$$Q = [\, \mathbf{q}_1 \; \mathbf{q}_2 \; \cdots \; \mathbf{q}_N \,] = A_{rcv} \tag{5.36}$$
$$W = [\, \mathbf{w}_1 \; \mathbf{w}_2 \; \cdots \; \mathbf{w}_N \,] = A_{xmit} \, .$$

We note from their description that the pairwise angle correspondence problem between ϕ_i and θ_j is non-trivial because a ray-based channel with $K = N_{rays}$ rays has $K!$ distinct possible pairings of i and j. Continuing the assumption that the additive noise in the channel is i.i.d. Gaussian distributed, the maximum likelihood estimate for complex gain parameters and pairing information is

$$[\hat{B}, \hat{P}\,] = \arg \min_{B,P} \| H - \hat{Q}\, P\, B\, \hat{W}^H \|_F^2 \, , \tag{5.37}$$

where the ray gain matrix, B, is constrained to be diagonal and the pairing matrix, P, is a permutation with each row and column containing at most one "1". The locations of the '1' terms in P associates columns of $\hat{Q}$ dependent on θ_j with columns of $\hat{W}$ derived from ϕ_i. The beam steering matrices, $\hat{Q} = \hat{A}_{rcv}$ and $\hat{W} = \hat{A}_{xmit}$ are formed as in Equation 5.3 using the angle estimates determined previously but without knowledge of correct column ordering. The fact that Equation 5.37 is not convex in P requires an exhaustive search over all $K!$ possible pairing configurations for P. As an alternative, this ad hoc pairing algorithm reduces the candidate search space by limiting the number of departure - arrival angle pairings.

The development begins by pointing out that the least squares solution to Equation 5.37 without constraining B to be diagonal is

$$\hat{B} = \hat{Q}^{\dagger}\, H\, (\hat{W}^H)^{\dagger} \, , \tag{5.38}$$

where $(\,)^{\dagger}$ indicates matrix pseudo-inverse. Note that $\hat{B} \approx P\, B$ where the approximation is due only to estimation errors in ϕ_i and $\theta_{rcv,j}$ and array calibration errors. Without considering these errors, $\hat{B}$ will have non-zero entries only at locations corresponding to the '1's in the pairing matrix, P, and can serve to identify P and the pair matching information it should contain. If P is known and B is constrained to be

www.manaraa.com

diagonal, then the solution to Equation 5.37 can be expressed in the following closed form:

$$\begin{aligned}
\mathbf{b} &= \mathcal{A}^{\dagger}\,\mathbf{h} \qquad (5.39)\\
\mathbf{h} &= \mathrm{vec}\{H\}\\
\mathcal{A} &= W^{*} \otimes Q\,P\\
&= [\,\mathbf{w}_1^{*} \otimes Q\,\mathbf{p}_1 \;\; \mathbf{w}_1^{*} \otimes Q\,\mathbf{p}_2 \;\cdots\; \mathbf{w}_1^{*} \otimes Q\,\mathbf{p}_K \;\; \mathbf{w}_2^{*} \otimes Q\,\mathbf{p}_1\\
&\qquad \mathbf{w}_2^{*} \otimes Q\,\mathbf{p}_2 \;\cdots\; \mathbf{w}_K^{*} \otimes Q\,\mathbf{p}_K\,]\,,
\end{aligned}$$

where $\otimes$ is the Kronecker matrix product and $\mathrm{vec}\{\cdot\}$ is the columnwise matrix vectorization operator.

The derivation of the relationships in Equation 5.39 starts from the well known vectorization property of the quadratic matrix product, which is that the vectorized product of three general complex matrices can be expressed as

$$\mathrm{vec}\{A\,Y\,B\} = (B^{H} \otimes\, A\,)\,\mathrm{vec}\{Y\}\,, \qquad (5.40)$$

where the matrices A, Y, and B have dimensions appropriate for multiplication. A proof of this relationship for the real-matrix case and examples demonstrating its utility in solving matrix equations of the form $A\,Y\,B = C$ for Y can be found in [72]. After expressing the Maximum-Likelihood criterion in Equation 5.37 as the following approximation,

$$H \cong \hat{Q}\,P\,B\,\hat{W}^{H}\,, \qquad (5.41)$$

we vectorize it and use the relationship in Equation 5.40. The matrix product $\hat{Q}\,P$ represents the receive steering vectors reordered from their original arbitrary sequence to correspond pairwise to the transmit steering vectors ordered in $\hat{W}$. It is treated as a single quantity to produce

$$\begin{aligned}
\mathbf{h} = \mathrm{vec}\{H\} &\cong \mathrm{vec}\left\{ \underbrace{\hat{Q}\,P}\; B\,\hat{W}^{H} \right\} \qquad (5.42)\\
&\cong \left(\hat{W}^{*} \otimes \underbrace{\hat{Q}\,P} \right) \mathrm{vec}\{B\}\,.
\end{aligned}$$

www.manaraa.com

The least squares solution for $\mathbf{b} = \text{vec}\{B\}$ is $\mathbf{b} = \mathcal{A}^{\dagger}\,\mathbf{h}$ where $\mathcal{A}$ results from the expansion of $(\,\hat{W}^{*} \otimes \hat{Q}\,P\,)$. At this point, the definitions of $\mathbf{h}$, $\mathbf{b}$, and $\mathcal{A}$ match those shown in the form of the solution for the complex ray gains shown in Equation 5.39. We can gain insight into the structure of $\mathcal{A}$ by observing that $\hat{Q}\,\mathbf{p}_i$ represents the receive steering vector that has been reordered to correspond in the ray synthesis model with β_i and the transmit steering vector at ϕ_i.

The pairing algorithm exploits these relationships and uses a short interaction to solve Equation 5.37 in the presence of error in $\hat{B}$, as outlined in the following steps.

1. Compute unstructured $\hat{B}$ as in Equation 5.38.

2. Define T as a threshold value such that $2K$ elements, $\hat{b}_{i,j}$, of $\hat{B}$ have magnitudes greater than T. Extract placement of '1's in $\hat{P}$ by letting

$$\hat{P} = \{\hat{p}_{i,j}\}, \text{where}\, \hat{p}_{\,i,j} = \begin{cases} 1 & |\,\hat{b}_{i,j}\,| \geq T \\ 0 & \text{otherwise}\,. \end{cases} \tag{5.43}$$

   In other words, non-zero entries in $\hat{P}$ correspond to the $2K$ largest elements of $\hat{B}$. These are candidate ray angle pairs.

3. Repeat the following steps K times.

   (a) Find the ray departure-arrival angle pair that contributes least to reducing error in the forward modeled H. Using Equation 5.39 to solve for B for each (i,j) pair in the minimization, find

$$(i\,',j\,') = \arg \min_{(i,j)\,\in\,S,B} \| \,H - \hat{Q}\,P\,B\,\hat{W}^{H}\,\|_{F}^{2}\,, \tag{5.44}$$

   where $S = \{\forall\,(i,j)\,|\,p_{\,i,j} = 1\}$.

   (b) Remove this pair from $\hat{P}$, i.e. $p_{\,i\,',j\,'} = 0$.

4. The final P contains the K correct ray angle pairings, and is used in Equation 5.39 for the final estimate of $\mathbf{b}$.

www.manaraa.com

5.2.5 2-D Unitary ESPRIT for MIMO ULA's

The version of 2-D *unitary* ESPRIT described here is an adaptation of the algorithm described by Zoltowski *et al.* for simultaneous, closed form 2-D angle estimation with uniform rectangular arrays [73] applied to a MIMO system with Uniform Linear Arrays. It is presented as an alternative 2-dimensional subspace Direction of Arrival estimator that gives pairing information along with transmit and receive angles. Unitary versions of subspace based estimators allow performance comparable to forward-backward-averaged methods along with a computation savings realized from replacing complex-valued computations with real-valued ones and the option of substituting simple addition for many multiplication operations. Because the ray synthesis form of the MIMO channel model is composed of a weighted sum of outer products of array manifold vectors, the narrowband channel transfer matrix, H, is similar to the angular dependent response of a uniform rectangular array used as a receiver. This presentation assumes the ULA structure on both the transmit and receive sides of the MIMO system for consistency with the material in the reference. However, the authors state in their conclusions that the algorithm may be easily adapted for other array configurations with a dual invariance structure such as a cross array. Our presentation here will approximately follow the development and notation of [73].

The mathematical definition of *conjugate centrosymmetry* of a vector $\mathbf{a}_N \in \mathbb{C}^{N\times 1}$ can be stated as $\Pi_N \, \mathbf{a}_N = \mathbf{a}_N^*$, where

$$\Pi_N = \begin{bmatrix} & & 1 \\ & \iddots & \\ 1 & & \end{bmatrix} \in \mathbb{R}^{N\times N} . \tag{5.45}$$

Using the observation that the inner product between any two conjugate centosymmetric vectors is real-valued, any matrix whose rows are each conjugate centrosymmetric will transform the complex-valued element space array manifold into a

www.manaraa.com

real-valued manifold. The unitary FB averaging matrix, Q, transforms the complex-valued element space manifold into a real-valued manifold without loss of information and is typically defined as

$$Q_{2K} = \frac{1}{\sqrt{2}} \begin{bmatrix} I_K & j\, I_K \\ \Pi_K & -j\, \Pi_K \end{bmatrix} \tag{5.46}$$

for even numbers of array elements, or

$$Q_{2K+1} = \frac{1}{\sqrt{2}} \begin{bmatrix} I_K & \mathbf{0} & j\, I_K \\ \mathbf{0}^T & \sqrt{2} & \mathbf{0}^T \\ \Pi_K & \mathbf{0} & -j\, \Pi_K \end{bmatrix} \tag{5.47}$$

for odd numbers of array elements. We introduce the shorthand angle notation of

$$\mu_i = \frac{2\pi}{\lambda}\, \Delta_{xmit}\, \sin(\,\phi_i\,) \quad \text{and} \quad \nu_i = \frac{2\pi}{\lambda}\, \Delta_{rcv}\, \sin(\,\theta_i\,)\ , \tag{5.48}$$

where Δ_{xmit}, Δ_{rcv} and λ are respectively the element spacing for the transmitter array, the element spacing for the receiver array and the system operating wavelength. The transformed real-valued array manifold vectors are formed by

$$\mathbf{d}_{xmit}(\mu_i) = Q_M^H\, \mathbf{a}_{xmit}(\mu_i) \quad \text{and} \quad \mathbf{d}_{rcv}(\nu i) = Q_N^H\, \mathbf{a}_{rcv}(\nu_i)\ . \tag{5.49}$$

Beginning with the ray-synthesis form of the channel transfer matrix from Equations 5.2 and 5.3, we can write

$$H = A_{xmit}\, B\, A_{rcv}^H \tag{5.50}$$
$$= [\,\mathbf{a}_{xmit}(\mu_1)\ \cdots\ \mathbf{a}_{xmit}(\mu_D)\,]\ \text{diag}\{[\,\beta_1\ \cdots\ \beta_D\,]\}\ [\,\mathbf{a}_{rcv}(\nu_1)\ \cdots\ \mathbf{a}_{rcv}(\nu_D)\,]^H\ .$$

Applying the unitary averaging transform to both sides of H yields

$$\tilde{H} = Q_M^H\, H\, Q_N = Q_M^H\, A_{xmit}\, B\, A_{rcv}^H\, Q_N\ . \tag{5.51}$$

We can notice that the columns of $Q_M^H\, A_{xmit}$ are the $\mathbf{d}_{xmit}(\mu_i)$ vectors, and that the rows of $A_{rcv}^H\, Q_N$ are the $\mathbf{d}_{rcv}^H(\nu_i)$ vectors for $i = 1, \ldots, D$. This allows us to rewrite the expression of $\tilde{H}$ as

$$\tilde{H} = Q_M^H\, H\, Q_N = D_{xmit}(\mu)\, B\, D_{rcv}^T(\nu)\ , \tag{5.52}$$

www.manaraa.com

where the transformed array manifold matrices are

$$D_{xmit}(\mu) = Q_M^H \, A_{xmit} = [\, \mathbf{d}_{xmit}(\mu_1) \; \cdots \; \mathbf{d}_{xmit}(\mu_D) \,] \tag{5.53}$$

and

$$D_{rcv}(\nu) = Q_N^H \, A_{rcv} = [\, \mathbf{d}_{rcv}(\nu_1) \; \cdots \; \mathbf{d}_{rcv}(\nu_D) \,] \, . \tag{5.54}$$

Taking the real-valued singular value decomposition of $\tilde{H}$ gives information about the rank D left and right signal subspaces, U_S and V_S :

$$\tilde{H} = U \, \Sigma \, V^T = [\; U_S \; U_N \;] \begin{bmatrix} \Sigma_S & \\ & \Sigma_N \end{bmatrix} [\; V_S \; V_N \;]^T \, . \tag{5.55}$$

From this and Equation 5.52, we can conclude that the columns of $D_{xmit}(\mu)$ span the same subspace as the columns of U_S and that the columns of $D_{rcv}(\nu)$ span the same subspace as the columns of V_S. This can be expressed as

$$U_S = D_{xmit}(\mu) \, T_\mu \quad \text{and} \quad V_S = D_{rcv}(\nu) \, T_\nu \, , \tag{5.56}$$

where the full-rank transformations T_μ and T_ν have dimension $D \times D$. Additionally, we can see from

$$\tilde{H} = U_S \, \Sigma_S \, V_S^H = D_{xmit}(\mu) \, \underbrace{T_\mu \, \Sigma_S \, T_\nu^T}_{B} \, D_{rcv}^T(\nu) = D_{xmit}(\mu) \, B \, D_{rcv}^T(\nu) \tag{5.57}$$

that the two-sided transform

$$T_\mu \, \Sigma_S \, T_\nu^T = B \tag{5.58}$$

maps the singular values in Σ_S onto the ray gain factors in B.

Using results for 1-D *unitary* ESPRIT derived explicitly in [73], we can state the invariance relationships inherent in the ESPRIT subarray structure identified by the subarray selection matrices $J1$ and $J2$ as

$$K_1 \, D_{xmit}(\mu) \, \Phi_\mu = K_2 \, D_{xmit}(\mu) \tag{5.59}$$

$$K_3 \, D_{rcv}(\nu) \, \Phi_\nu = K_3 \, D_{rcv}(\nu) \, , \tag{5.60}$$

www.manaraa.com

where the following matrices have been defined:

$$K_1 = \mathcal{R}e\left\{Q_{M-1}^H\, J_2\, Q_M\right\} \quad \text{and} \quad K_2 = \mathcal{I}m\left\{Q_{M-1}^H\, J_2\, Q_M\right\} \tag{5.61}$$

$$K_3 = \mathcal{R}e\left\{Q_{N-1}^H\, J_2\, Q_N\right\} \quad \text{and} \quad K_4 = \mathcal{I}m\left\{Q_{N-1}^H\, J_2\, Q_N\right\} \tag{5.62}$$

$$\Phi_\mu = \begin{bmatrix} \tan\left(\frac{\mu_1}{2}\right) & & \\ & \ddots & \\ & & \tan\left(\frac{\mu_D}{2}\right) \end{bmatrix} \tag{5.63}$$

$$\Phi_\nu = \begin{bmatrix} \tan\left(\frac{\nu_1}{2}\right) & & \\ & \ddots & \\ & & \tan\left(\frac{\nu_D}{2}\right) \end{bmatrix}. \tag{5.64}$$

If we use Equation 5.59 and the substitution $U_S = D_{xmit}(\mu)\, T_\mu$ from Equation 5.56, we can expand the following expression for $K_2\, U_S$

$$\begin{aligned} K_2\, U_S &= K_2\, D_{xmit}(\mu)\, T_\mu = K_1\, D_{xmit}(\mu)\, \Phi_\mu\, T_\mu \\ &= K_1\, D_{xmit}(\mu)\, \underbrace{T_\mu\, T_\mu^{-1}}_{I}\, \Phi_\mu\, T_\mu \\ &= K_1\, \underbrace{D_{xmit}(\mu)\, T_\mu}_{U_S}\, \underbrace{T_\mu^{-1}\, \Phi_\mu\, T_\mu}_{\Psi_\mu} = K_1\, U_S\, \Psi_\mu\,. \end{aligned} \tag{5.65}$$

In an analogous fashion, $K_4\, V_S$ becomes

$$\begin{aligned} K_4\, V_S &= K_4\, D_{rcv}(\nu)\, T_\nu = K_3\, D_{rcv}(\nu)\, \Phi_\nu\, T_\nu \\ &= K_3\, D_{rcv}(\nu)\, \underbrace{T_\nu\, T_\nu^{-1}}_{I}\, \Phi_\nu\, T_\nu \\ &= K_3\, \underbrace{D_{rcv}(\nu)\, T_\nu}_{V_S}\, \underbrace{T_\nu^{-1}\, \Phi_\nu\, T_\nu}_{\Psi_\nu} = K_3\, V_S\, \Psi_\nu\,. \end{aligned} \tag{5.66}$$

It is significant to notice that $\Psi_\mu = T_\mu^{-1}\, \Phi_\mu\, T_\mu$ and $\Psi_\nu = T_\nu^{-1}\, \Phi_\nu\, T_\nu$ are similarity transforms. This guarantees that the eigenvalues of Ψ_μ and Ψ_ν are identical to those of Φ_μ and Φ_ν which are directly dependent on the transmit and receive angles as represented by the μ_i's and ν_i's. We can isolate the Ψ_μ and Ψ_ν matrices by using

www.manaraa.com

the following expressions which result from solving Equations 5.65 and 5.66 in a least-squares sense to obtain

$$\Psi_\mu = (K_1 U_S)^\dagger K_2 U_S \tag{5.67}$$

and

$$\Psi_\nu = (K_3 V_S)^\dagger K_4 V_S \, . \tag{5.68}$$

The remaining goal is to find an expression which pairs the eigenvalues of the two real-valued matrices Φ_μ and Φ_ν so that the association between μ_i and ν_j can be established. To accomplish this, we need a substitution for T_μ in terms of T_ν. This can be found by solving Equation 5.58, $T_\mu \Sigma_S T_\nu^T = B$, for T_μ as expressed in two useful forms as

$$\begin{aligned} T_\mu &= B \, T_\nu^{-T} \, \Sigma_S^{-1} \\ T_\mu^{-1} &= \Sigma_S \, T_\nu^T \, B^{-1} \, . \end{aligned} \tag{5.69}$$

Our starting point is to substitute $\Psi_\mu = T_\mu^{-1} \Phi_\mu T_\mu$ and $\Psi_\nu = T_\nu^{-1} \Phi_\nu T_\nu$ into the complex-valued expression $\Psi_\mu + j \, \Psi_\nu^T$ and proceed by using the expressions in 5.69:

$$\begin{aligned} \Psi_\mu + j \, \Psi_\nu^T &= T_\mu^{-1} \, \Phi_\mu \, T_\mu + j \, T_\nu^T \, \Phi_\nu \, T_\nu^{-T} \\ &= \Sigma_S \, T_\nu^T \, \underbrace{B^{-1} \, \Phi_\mu \, B} \, T_\nu^{-T} \, \Sigma_S^{-1} + j \, T_\nu^T \, \Phi_\nu \, T_\nu^{-T} \\ &= \Sigma_S \, T_\nu^T \, \Phi_\mu \, T_\nu^{-T} \, \Sigma_S^{-1} + j \, T_\nu^T \, \Phi_\nu \, T_\nu^{-T} \, . \end{aligned} \tag{5.70}$$

Notice that the grouped quantity $B^{-1} \, \Phi_\mu \, B$ consists of all diagonal matrices, so the product can be taken in any convenient order, such as

$$B^{-1} \, \Phi_\mu \, B = (\, B \, B^{-1} \,) \, \Phi_\mu = I \, \Phi_\mu = \Phi_\mu \, . \tag{5.71}$$

Equation 5.70 can be converted into a complex-valued similarity transform with only a slight modification:

$$\begin{aligned} \Sigma_S^{-1} \, \Psi_\mu \, \Sigma_S + j \, \Psi_\nu^T &= T_\nu^T \, \Phi_\mu \, T_\nu^{-T} + j \, T_\nu^T \, \Phi_\nu \, T_\nu^{-T} \\ &= T_\nu^T \, (\, \Phi_\mu + j \, \Phi_\nu \,) \, T_\nu^{-T} \, . \end{aligned} \tag{5.72}$$

www.manaraa.com

This is convenient because Σ_S can be obtained from the SVD of $\tilde{H}$. The eigenvalues of $\Sigma_S^{-1}\,\Psi_\mu\,\Sigma_S + j\,\Psi_\nu^T$, denoted $\lambda_1, \ldots, \lambda_D$, will be the appropriately paired entries of $\Phi_\mu + j\,\Phi_\nu$ such that

$$\mu_i = 2\tan^{-1}\left(\mathcal{R}e\left\{\lambda_i\right\}\right) \quad \text{and} \quad \nu_i = 2\tan^{-1}\left(\mathcal{I}m\left\{\lambda_i\right\}\right). \tag{5.73}$$

Once the μ_i's and ν_i's are known, they can be translated into ϕ_i and θ_{rcv_i} by solving Equation 5.48 :

$$\phi_i = \sin^{-1}\left(\frac{\mu_i\,\lambda}{2\pi\,\Delta_{xmit}}\right) \quad \text{and} \quad \theta_i = \sin^{-1}\left(\frac{\nu_i\,\lambda}{2\pi\,\Delta_{rcv}}\right). \tag{5.74}$$

At this point, the transmit and receive angle pairs have been estimated, and the gain factors for each ray can be estimated using the vectorized least squares approach in Equation 5.39.

The following steps summarize the 2-D ESPRIT estimation process:

1. Form the real-valued, smoothed $\tilde{H} = Q_M^H\,H\,Q_N$,
2. Calculate the SVD of $\tilde{H} = U\,\Sigma\,V^T$ and form the D-dimensional signal subspace model for $\tilde{H} = U_S\,\Sigma_S\,V_S^H$,
3. Solve for Ψ_μ and Ψ_ν using Equations 5.67 and 5.68 ,
4. Find the eigenvalues $\lambda_1, \ldots, \lambda_D$ of the complex matrix $\Sigma_S^{-1}\,\Psi_\mu\,\Sigma_S + j\,\Psi_\nu^T$,
5. Solve for the μ_i's and ν_i's in terms of the λ_i's using Equation 5.73 ,
6. Finally, solve for the ϕ_i's and θ_i's in terms of the μ_i's and ν_i's using Equation 5.74 .

5.3 Calculating Information Capacity of MIMO Channel with Feedback

In the standard Full-CSI waterfilling capacity solution described in Section 2.2, the covariance, Q, for the transmitted symbols is determined by finding the left

www.manaraa.com

dominant subspace of the channel matrix, H, using the SVD of H or the eigendecomposition of $H^H H$:

$$H = U \Sigma V^H \quad \text{or} \quad H^H H = U \Lambda U^H . \tag{5.75}$$

The covariance, Q, is chosen so that the quantity $\tilde{Q} \equiv U^H Q U$ will be diagonal as described in Equation 2.14. This indicates that Q should be formed from

$$Q = U \tilde{Q} U^H , \tag{5.76}$$

where the non-zero entries of $\tilde{Q}$ are obtained by the waterfilling equation:

$$\tilde{Q}_{ii} = (\mu - \lambda_i^{-1})^+ . \tag{5.77}$$

The λ_i's are the eigenvalues of $H^H H$ which are equivalent to the squared singular values of H, σ_i^2. The parameter μ is selected so that the maximum transmit power constraint is satisfied:

$$\text{tr}\,(Q) = \text{tr}\left(\tilde{Q} \right) = \sum_i (\mu - \lambda_i^{-1})^+ \leq \rho . \tag{5.78}$$

In the CSI-Feedback case, we assume that the best approximation of H available to the transmitter is the H_{model} generated using the ray-synthesis equation with the ray parameters passed from the receiver as in

$$\hat{H} = H_{model} = \sum_{i=1}^{N_{rays}} \mathbf{a}_{xmit}(\phi_i)\, \beta_i\, \mathbf{a}_{rcv}(\theta_i)^H . \tag{5.79}$$

This estimate is normalized to have average unit modulus elements to make it SNR independent by using

$$\hat{H} = \hat{H} \sqrt{\frac{M\,N}{\sum_{i=1}^{M} \sum_{j=1}^{N} |\hat{H}_{i,j}|^2}} = \hat{H} \sqrt{\frac{M\,N}{\| \hat{H} \|_F^2}} = \hat{H} \frac{\sqrt{M\,N}}{\| \hat{H} \|_F} . \tag{5.80}$$

The estimate of U is formed from the left dominant subspace of $\hat{H}$:

$$\hat{H} = \hat{U} \hat{\Sigma} \hat{V}^H \quad \text{or} \quad \hat{H}^H \hat{H} = \hat{U} \hat{\Lambda} \hat{U}^H . \tag{5.81}$$

www.manaraa.com

Then, the estimate of Q is calculated by following Equation 5.76 to obtain

$$\hat{Q} = \hat{U}\,\tilde{Q}\,\hat{U}^{H} \tag{5.82}$$

and estimating the non-zero entries of $\tilde{Q}$ using $\hat{\lambda}_i = \hat{\sigma}_i^2$ in the waterfilling equation under the standard maximum transmit power constraint in Equation 5.78:

$$\tilde{Q}_{ii} = (\,\mu \;-\; \hat{\lambda}_i^{-1})^{+}\,. \tag{5.83}$$

We can then insert $\hat{Q}$ into the mutual information equation to obtain the channel capacity for the CSI feedback case:

$$C_{feedback} = \log(\,\det(I_R + H\,Q\,H^{H}))\,. \tag{5.84}$$

The degree to which $C_{feedback}$ approaches the Full-CSI maximum capacity is determined by how well $\tilde{Q} = \hat{U}^{H}\hat{Q}\,\hat{U}$ is diagonalized and how closely the eigenvalues of $\hat{Q}$ match the optimal eigenchannel weightings from the waterfilling solution.

5.4 Simulation Results

To investigate the performance of the ray model feedback algorithm, we simulated instances of MIMO ULA channels synthesized using the ray-synthesis model with random parameters. The parameters and their random distributions are shown in Table 5.1. A random variable x with Circular Complex Gaussian (CCG) distribution having mean m and variance $\sigma^2 = \mathrm{E}\{\,(x-m)(x-m)^{*}\,\}$ can be generated using the following convenient function of random variables a and b which are uniformly distributed as $a, b \sim \mathcal{U}\,[0,1]$:

$$x = \sqrt{-\sigma^2 \ln(a)}\;\; \mathrm{e}^{j\,2\pi b} + m \;\sim\; \mathcal{CN}(m\,,\,\sigma^2)\,. \tag{5.85}$$

The random channel matrix is synthesized from the ray parameters using Equation 5.1:

$$H = \sum_{i=1}^{N_{rays}} \mathbf{a}_{xmit}\,(\phi_i)\;\beta_i\;\mathbf{a}_{rcv}\,(\theta_i)^{H}\,. \tag{5.86}$$

www.manaraa.com

Table 5.1: Comparison of model parameter values using different cluster identification strategies.

Model Parameter	**Notation**	**Distribution**
Transmit Angles	ϕ_i	Uniform $\sim\ \mathcal{U}\,[-90°, 90°]$
Receive Angles	θ_i	Uniform $\sim\ \mathcal{U}\,[-90°, 90°]$
Ray Gains	β_i	CCG $\sim\ \mathcal{CN}(m = 0\,,\ \sigma^2 = 1)$

The $\mathbf{a}_{xmit}$ and $\mathbf{a}_{rcv}$ were chosen for a 10-element ULA with $\lambda/4$ spacing to model the MIMO Channel Sounding measurements used in Section 5.5. Then, to make the channel realization SNR independent, it is scaled so the expected magnitude of each entry is unity, $\mathrm{E}\{\,|H_{i,h}|\,\} = 1$ for $i = 1, \ldots, M$ and $j = 1, \ldots, N$, using

$$H = H\,\sqrt{\frac{M\,N}{\sum_{i=1}^{M}\sum_{j=1}^{N}\,|H_{i,j}|^2}} = H\,\sqrt{\frac{M\,N}{\|\,H\,\|_F^2}} = H\,\frac{\sqrt{M\,N}}{\|\,H\,\|_F}\,. \tag{5.87}$$

This allows the SNR of the system to be defined as

$$\text{SNR (dB)} = 10\log\frac{P_T}{\sigma^2}\,, \tag{5.88}$$

where P_T is the total power emitted from the transmit array and σ^2 is the noise power present in a single element receiver, $\sigma^2 = \mathrm{E}\{\,n_i\,n_i^*\}$. In these simulations, the noise power, σ^2 is always chosen to be 1.

In the case of Full CSI simulations, the unit modulus H is used directly in estimating the model feedback parameters. When training-based estimation is used at the simulated endpoints, an estimate of H is obtained by generating a sequence of random training symbols received in noise using

$$X = H\,S + N\,. \tag{5.89}$$

The elements of the transmitted symbol matrix, $S \in \mathbb{C}^{N\times N_{symbols}}$, are independent and identically distributed (i.i.d.) as $\mathcal{CN}(0, \sigma_S^2)$, and the elements of the noise matrix,

www.manaraa.com

$N \in \mathbb{C}^{M \times N_{symbols}}$, are i.i.d. using $\mathcal{CN}(0, \sigma^2)$. $\hat{H}$ is obtained then from the least squares solution:

$$\hat{H} = X\, S^{\dagger}\,. \tag{5.90}$$

In estimated channel cases, the model parameter estimation algorithms operate upon $\hat{H}$. The full-knowledge H is always used in the calculation of the maximum capacity via the waterfilling solution (as if perfect CSI feedback were available) and the Fully Blind Transmitter capacity (where no CSI feedback is given). These provide upper and lower bounds for comparison of the feedback algorithms' capacity performance.

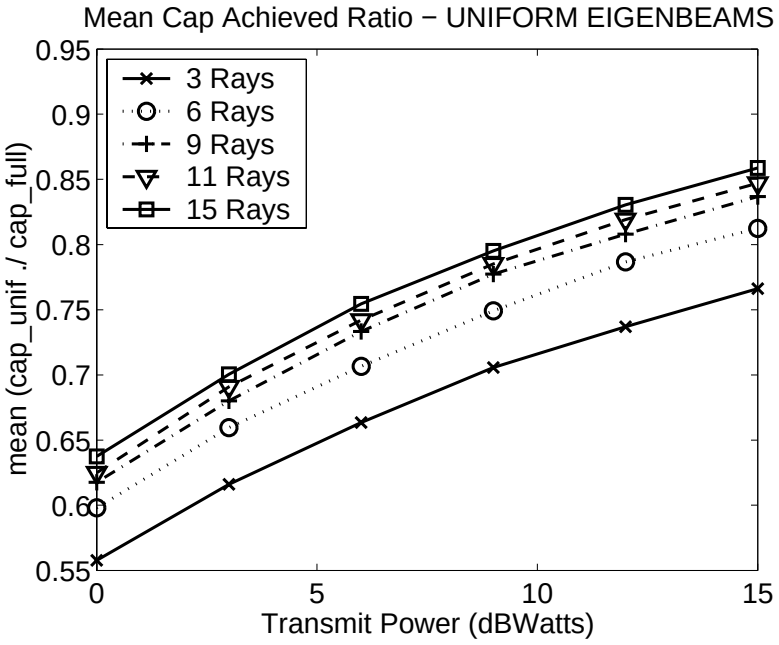

Figure 5.3: Mean capacity achieved ratio - fully blind transmitter with uniform power eigenbeams

As shown in Figure 5.3, the Fully Blind Capacity of the MIMO channel increases with the transmit power and the richness of the scattering environment (as represented by the number of contributing ray paths). This suggests that for high

www.manaraa.com

SNR values and very rich scattering, the capacity improvement possible from exploiting knowledge of the structure of H diminishes. In order to compare the capacity improvement by using model parameter feedback with the "no feedback" case over a range of SNR values and channel complexity, we decided to present the results in terms of the following ratios:

$$\text{Capacity Achieved Ratio} = \frac{C_{feedback}}{C_{maximum}} \tag{5.91}$$

and

$$\text{Capacity Improvement Ratio} = \frac{C_{feedback} - C_{uniform}}{C_{maximum}} \,. \tag{5.92}$$

In these expressions, the maximum capacity using full knowledge of the channel via the waterfilling solution is $C_{maximum}$, and $C_{uniform}$ represents the Fully Blind Transmitter case where the power allocation is uniform over all eigenchannels (i.e. $Q = \frac{P_T}{N} I_N$). The Capacity Achieved Ratio is a measure of how well the model parameter feedback approaches the Full CSI Transmitter case, and the Capacity Improvement Ratio indicates a comparison to the "no feedback" case to allow a decision about the merit of the additional complexity the feedback requires.

5.4.1 Full CSI Receiver

Figure 5.4 shows the Capacity Achieved Ratios and Capacity Improvement Ratios for Full CSI receivers using the four parameter estimation algorithms: MIMO Beamscan, MUSIC, 1-D ESPRIT, and 2-D ESPRIT. For each algorithm, we selected the number of trials in consideration of the simulation run times: Beamscan - 400 trials, MUSIC - 100 trials, 1-D ESPRIT - 100 trials, and 2-DESPRIT - 500 trials. As expected, the MIMO Beamscan algorithm has the worst performance, although it manages to achieve around 90% of the maximum capacity. It is interesting that the achieved ratio curves reverse slope as the number of active eigenchannels increases. MUSIC, 1-D ESPRIT, and 2-D ESPRIT all performed comparably well in this case, with nominally 100% maximum capacity achieved through feedback for channel orders smaller than the receive array size. As the channel order increases and the signal

www.manaraa.com

subspace dimension approaches the number of receive element, they all exhibit similar degradation.

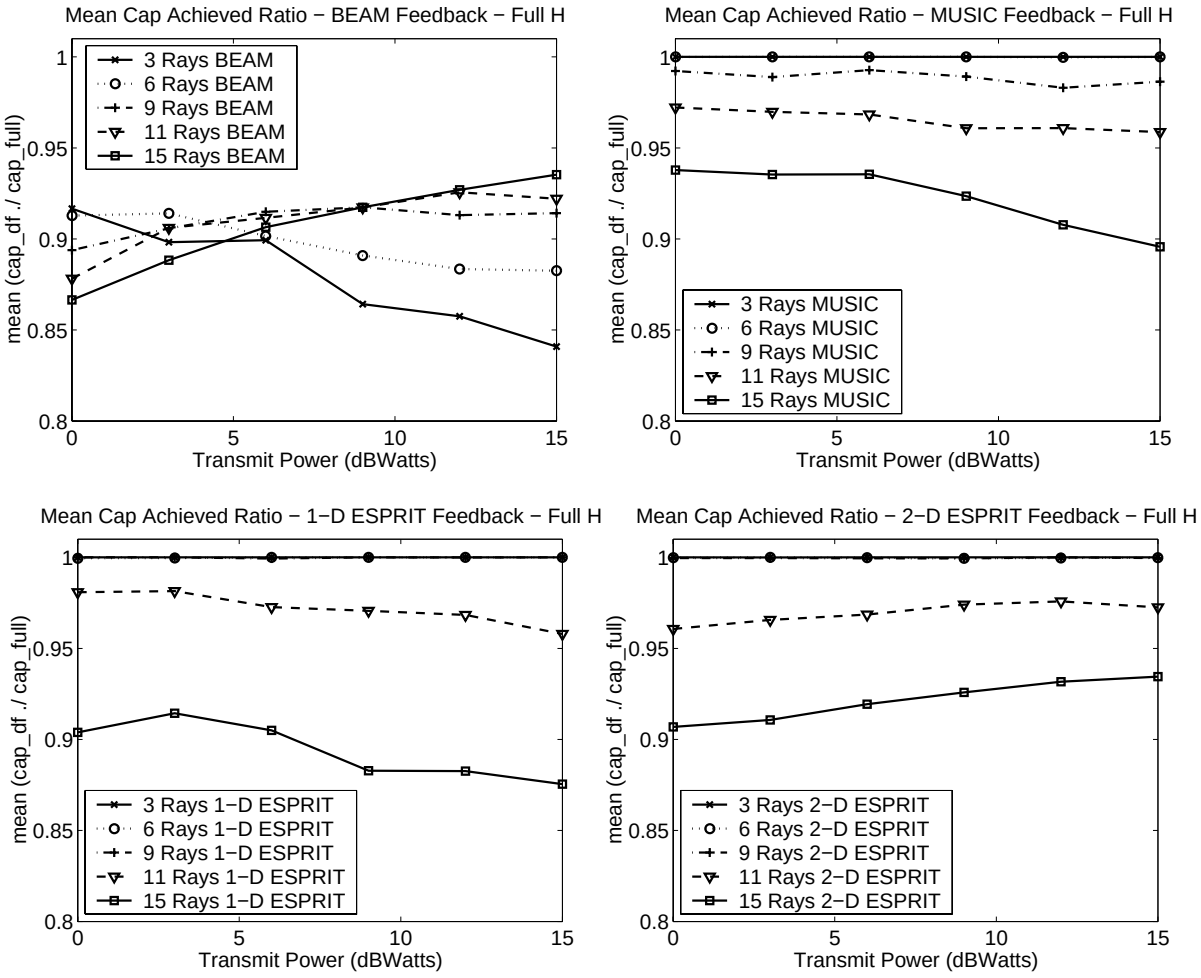

Figure 5.4: Mean capacity achieved ratio - full CSI - algorithm comparison.

www.manaraa.com

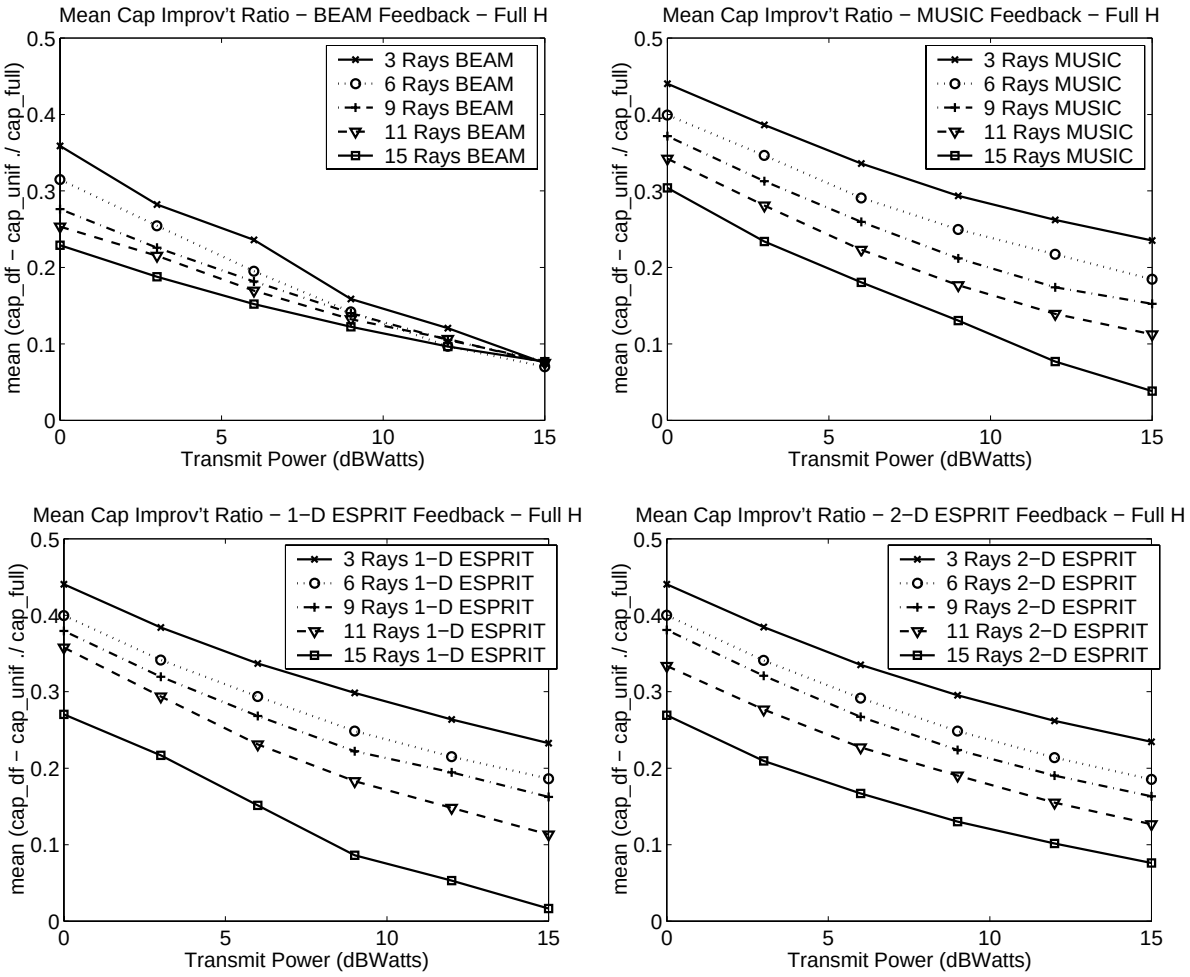

Figure 5.5: Mean capacity improved ratio - full CSI - algorithm comparison.

5.4.2 Training-Based Receiver

Figures 5.6 through 5.9 show the Capacity Achieved Ratio and Capacity Improved Ratio for the estimated channel case using MIMO Beamscan, MUSIC, 1-D ESPRIT, and 2-D ESPRIT feedback. In each case, the Capacity Achieved Ratio plots are in the left column, and the Capacity Improved Ratio plots are in the right column. A significant performance penalty is imposed as the estimation algorithms deal with an imperfectly estimated channel matrix, and the capacity ratios are much lower as a result. In each case, the effect of the number of training symbols used is examined by simulating with $N_{symbols} = 10$, 15 and 20. This indicates an S matrix with dimension

www.manaraa.com

$N \times N_{symbols}$. In the $N_{symbols} = 10$ case, the channel estimation problem is functioning with the minimum amount of data to allow a solution.

For the minimum number of symbols, all of the estimators seemed to be limited by errors in $\hat{H}$ when the SNR was low. They show dramatic improving trends as the SNR is increased. In this operating mode, the capacity improvement over $C_{uniform}$ is fairly flat with SNR for all of the estimators, with the MIMO BEAM approach yielding 5-10% improvement and the three subspace based techniques declining in performance as the dimension of the signal subspace increases. The MUSIC algorithm has some disconcerting performance at larger SNR values with higher complexity channels where it actually performs worse than the Blind Transmitter case. The best performance overall all comes from the 1-D ESPRIT with capacity achieved ratios above 93% or better when using reasonable numbers of training symbols with little dependence on SNR. 2-D ESPRIT avoids the iterative angle matching step with approximately 10% lower capacity improvement ratios than 1-D ESPRIT.

Figure 5.10 is included to provide a comparison among the four feedback algorithms. It shows the mean values for Capacity Achieved Ratio for all ray model feedback algorithms with selected parameter settings. The number of training symbols is fixed at 20, and the three plots show $N_{rays} = \{3, 9, 15\}$. Figures 5.11 and 5.12 show a comparison between random SVA clustered channels, iid zero-mean random channels, and the random Ray Synthesis channels used in the remainder of the simulations presented. The first figure shows mean Capacity Achieved Ratio at all SNR values, and the second shows CCDF's of the same data at SNR = $\{0, 6, 15$ dB$\}$. For these comparisons, the 1-D ESPRIT algorithm was used to determine the feedback with training-based channel estimation with $N_{symbols} = 20$. It is interesting to note that the SVA channel performance is equivalent to Ray Synthesis channels with about 9 rays at low SNR and with about 11 rays at higher SNR, and that the performance under iid zero-mean random channels is significantly lower. This indicates the capacity value of non-zero mean and correlation information in the channel matrix when using ray model feedback and underscores the related discussion in [8]. In a

www.manaraa.com

related manner, the assumption of zero-mean, uncorrelated channel gains produces much lower capacity as this reflects a condition where the long-term behavior of the channel has been averaged to remove all non-zero mean information in the channel gain terms and the number of multipath components is assumed large enough to remove all correlation. As the SNR increases, the ray model feedback is incapable of representing enough eigenmodes to keep up with the waterfilling solution, and the distribution becomes multi-modal as a function of the number of eigenchannels represented by the feedback model. This is reflected in the stair-step shape of the iid CCDF curve. When the channel state information is does not provide non-zero mean and non-white correlation information, ray model feedback is not a good choice for realizing the full information capacity of MIMO channels.

www.manaraa.com

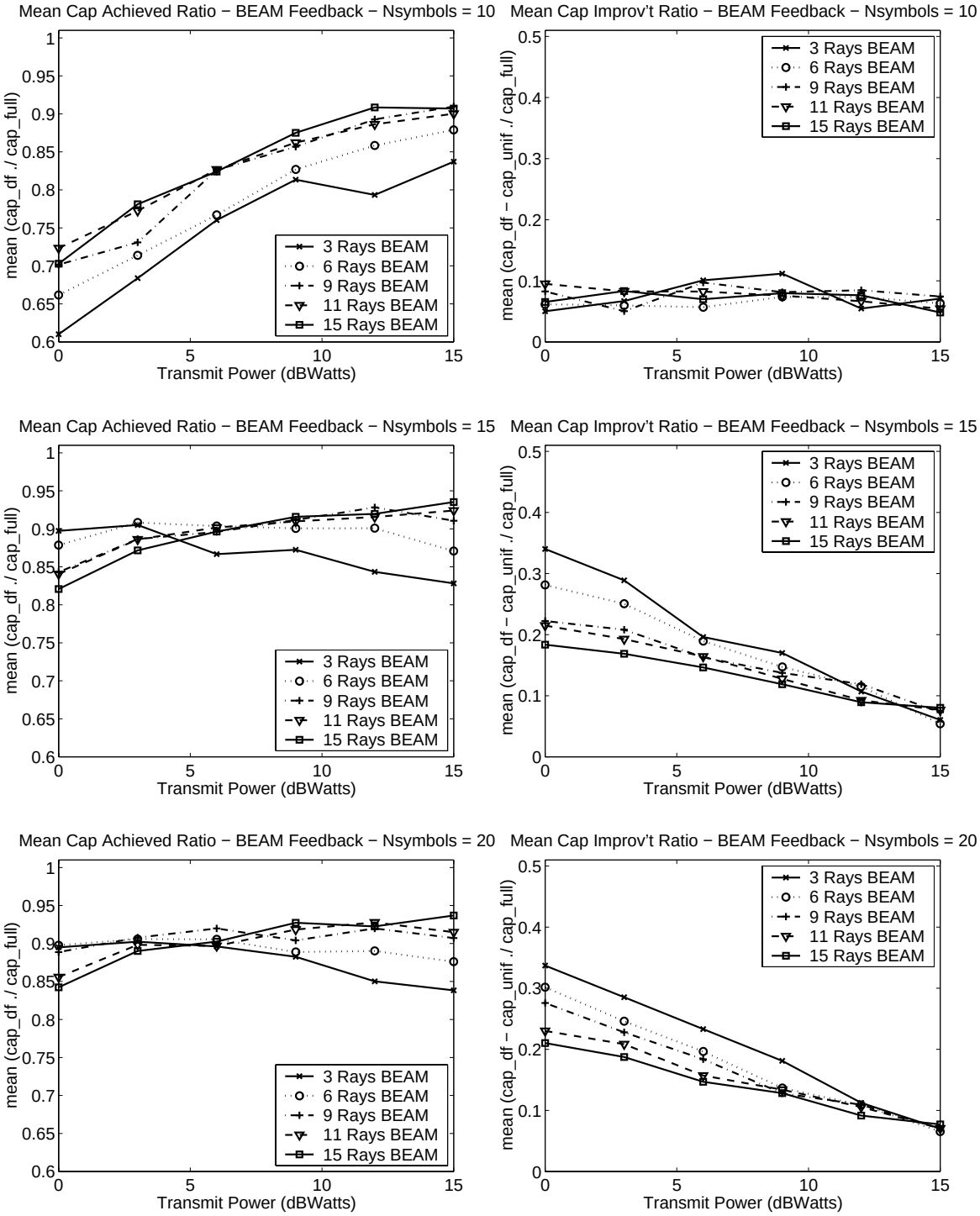

Figure 5.6: Mean capacity achieved ratio (left) and mean capacity improved ratio (right) - training beamscan feedback (400 trials, $N_{symbols} = \{10, 15, 20\}$)

www.manaraa.com

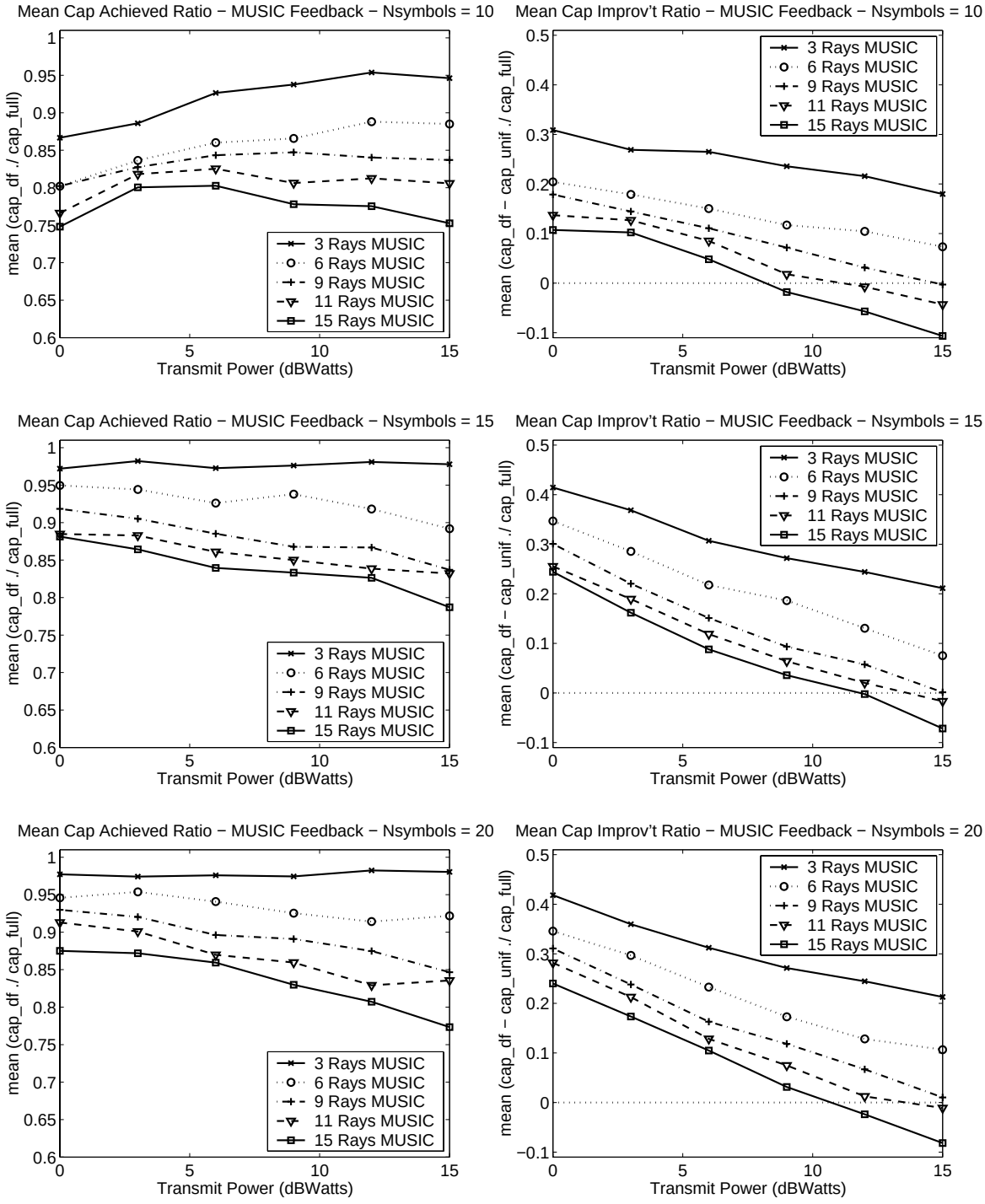

Figure 5.7: Mean capacity achieved ratio (left) and mean capacity improved ratio (right) - training MUSIC feedback (100 trials, $N_{symbols} = \{10, 15, 20\}$)

www.manaraa.com

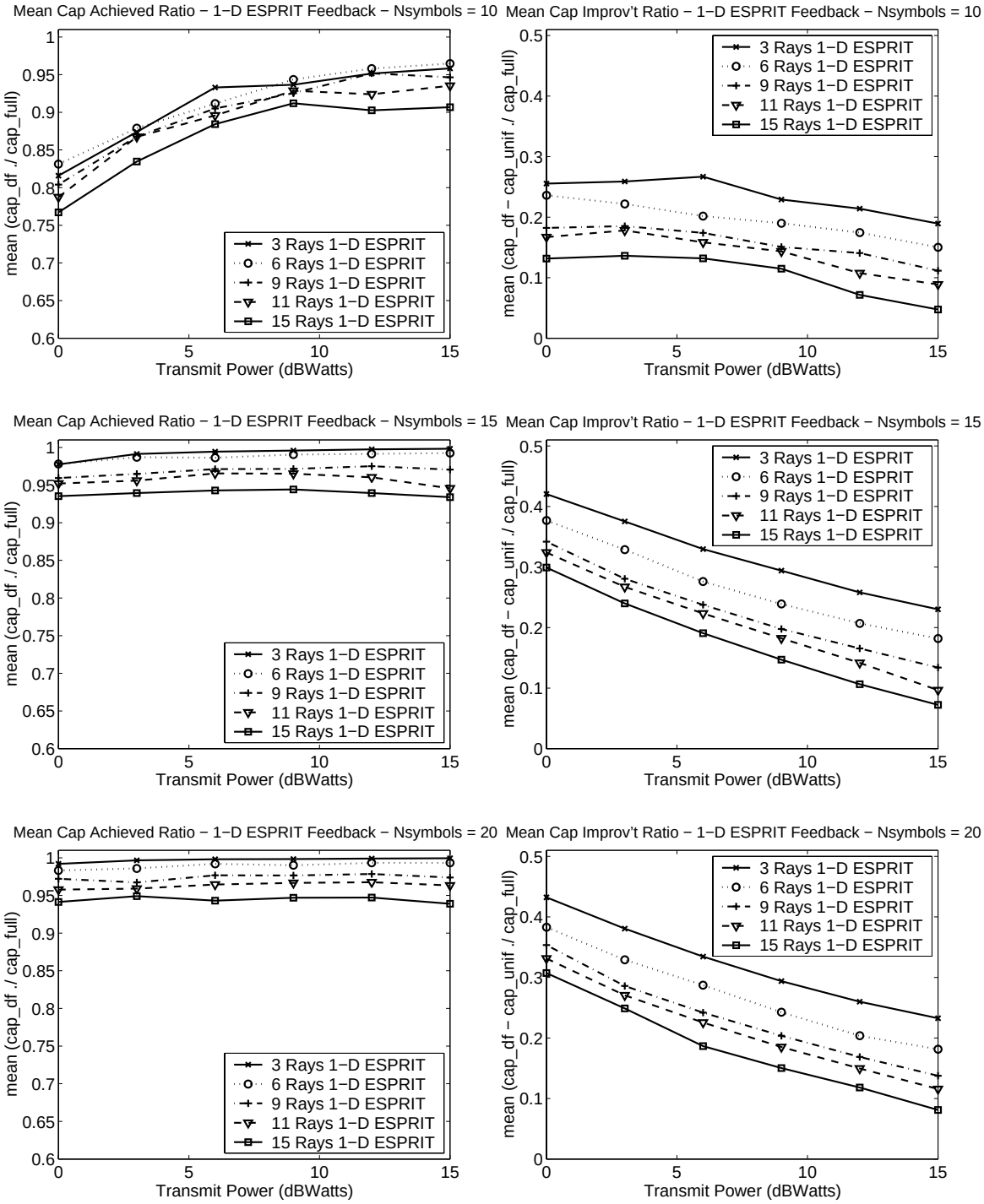

Figure 5.8: Mean capacity achieved ratio (left) and mean capacity improved ratio (right) - training 1-D ESPRIT feedback (100 trials, $N_{symbols} = \{10, 15, 20\}$, $\Delta = \lambda/4$)

www.manaraa.com

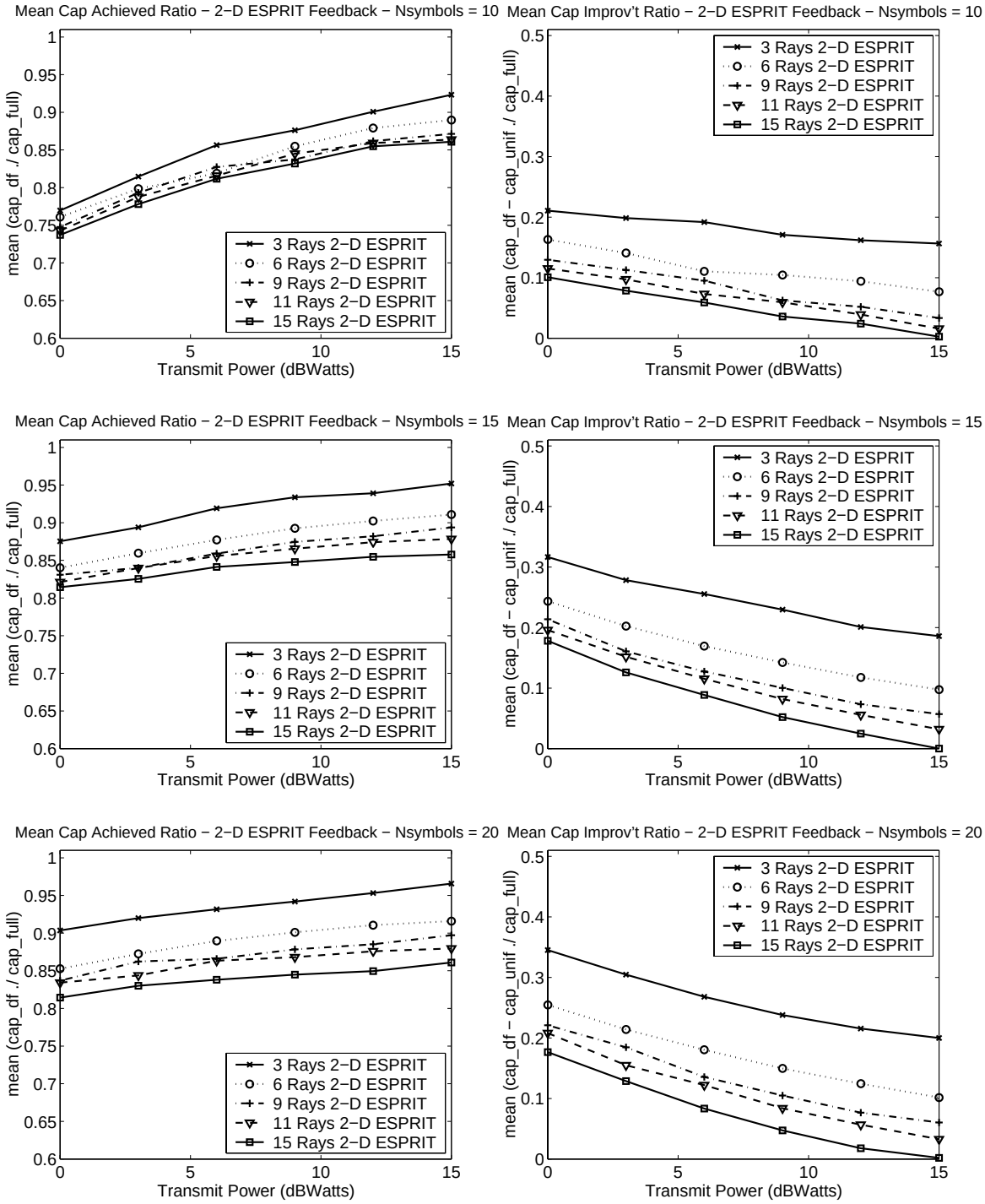

Figure 5.9: Mean capacity achieved ratio (left) and mean capacity improved ratio (right) - training 2-D ESPRIT feedback (500 trials, $N_{symbols} = \{10, 15, 20\}$, $\Delta = \lambda/2$)

www.manaraa.com

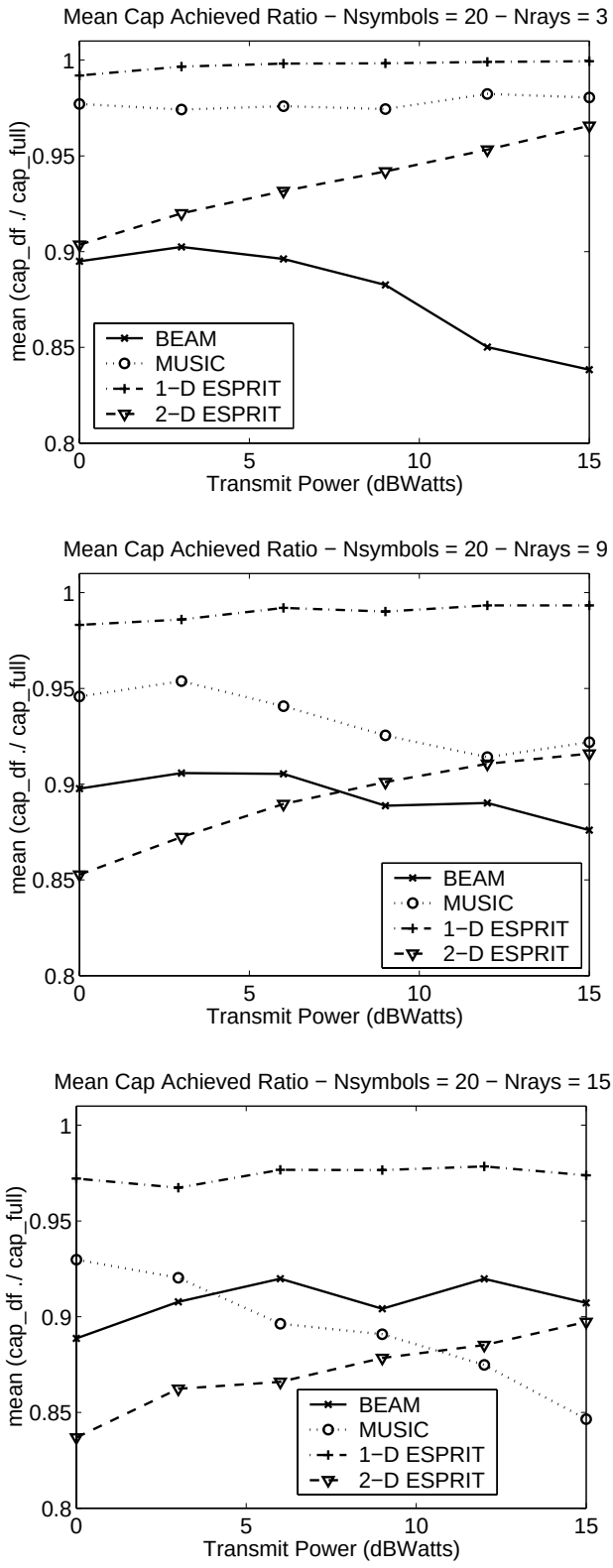

Figure 5.10: Mean capacity achieved ratio - all feedback algorithms - ($N_{symbols} = 20$, $N_{rays} = \{3, 9, 15\}$)

www.manaraa.com

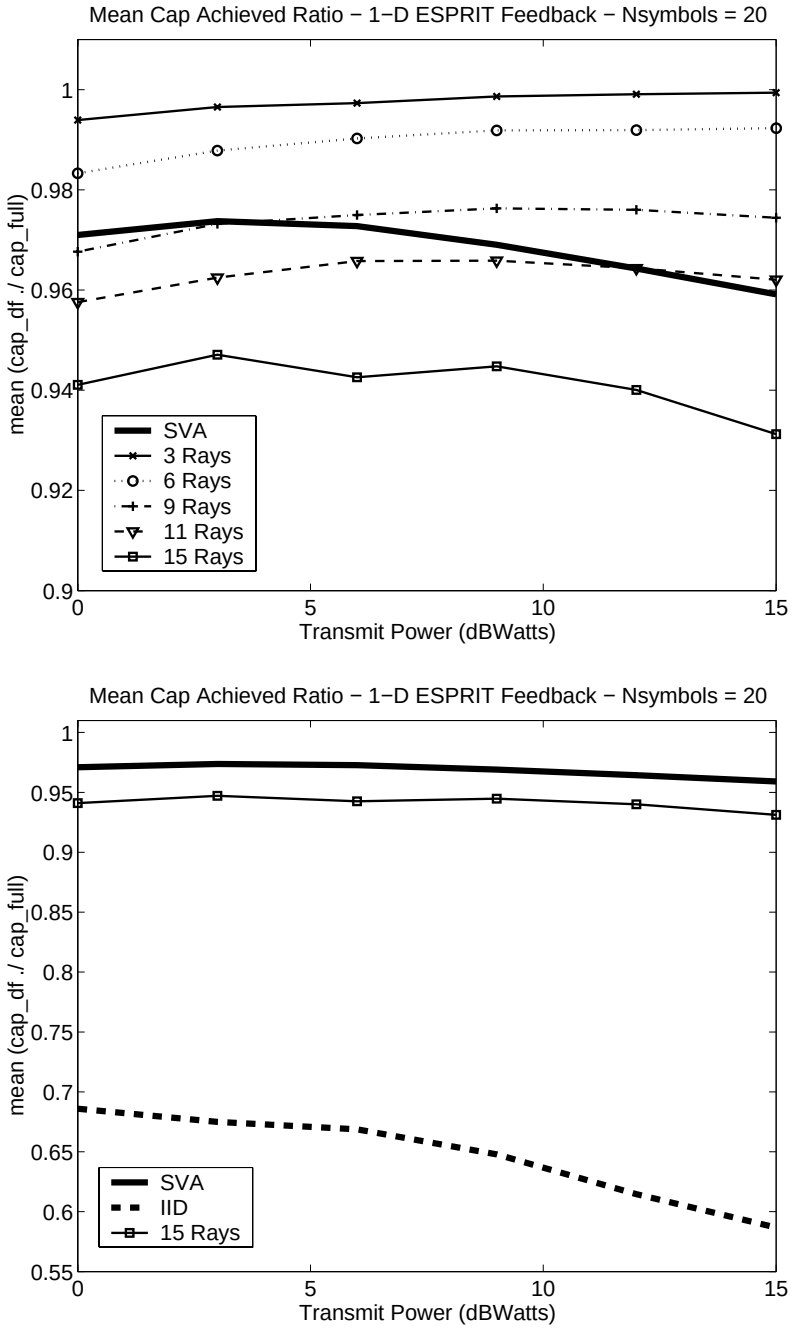

Figure 5.11: Mean capacity achieved ratio - 1-D ESPRIT - SVA and IID channels V. ray synthesis channels - ($N_{symbols} = 20$)

www.manaraa.com

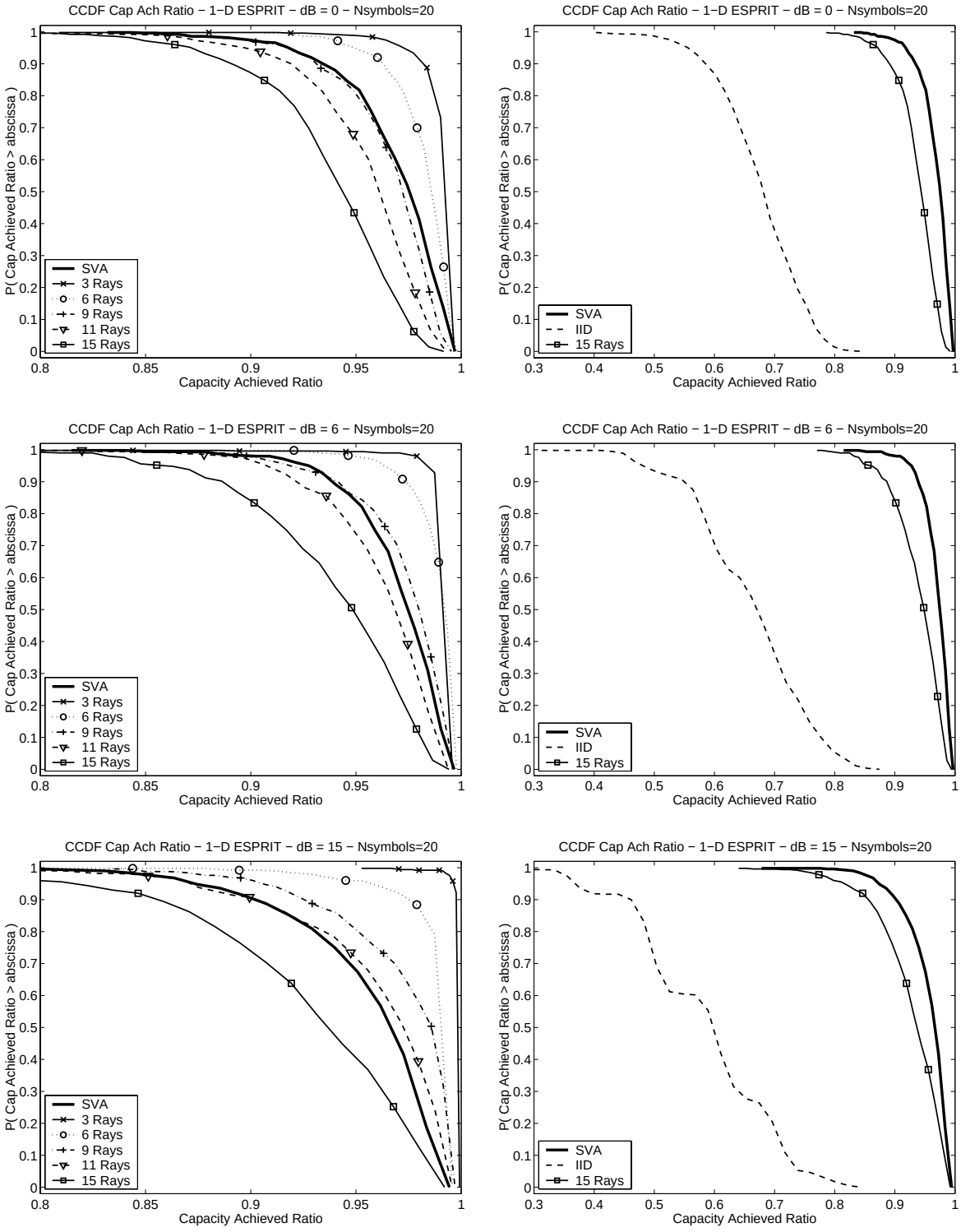

Figure 5.12: CCDF capacity achieved ratio - SVA and IID channels V. ray synthesis channels - ($N_{symbols} = 20$, $dB = \{0, 6, 15\}$)

www.manaraa.com

5.5 2.45 GHz MIMO Channel Sounding Results

Using the MIMO Narrowband Channel Measurement platform described in [42], we replicated several of the transmit/receive locations simulated with the WiSE ray tracing package to compare performance of the ray model feedback algorithm on measured data. The system operated at a center frequency of 2.45 GHz using symmetric 10×10 linear arrays of dipole elements with $\lambda/4$ spacing. In choosing the locations for measurements, we focused on locations where there was at least one wall (and preferably several) between transmitter and receiver to encourage rich scattering and less dominance of the Line of Sight path. The 7 endpoint locations are shown in Figure 5.13. At each location, measurements were taken in two combinations with the array broadside pointing north, south, east or west: the first pair being approximately broadside to each other and the second pair with one array oriented approximately endfire to the broadside of the other. For additional information, see [42] and [74].

For each of 26 measurement locations, there were between 3800 - 6200 instances of the channel measured 80 ms apart. For each measured H, the channel was normalized to average unit modulus using Equation 5.87, the feedback parameters were estimated, and the capacities were calculated for several values of SNR. The SNR variable only affected the value of P_T used in the waterfilling equations; neither H or the model feedback parameters varied with SNR. The measured H was used as if it were the "true" channel. No channel estimation was applied. The 1-D ESPRIT algorithm was selected for analysis with the measured data because of it seemed to be the most robust in the simulation results. The feedback capacity improvement was typically best at the lowest SNR values. Figure 5.14 shows the histograms of the capacity achieved ratio and capacity improved ratio over all measurement locations at SNR = 0 dB. A typical example showing the time-variability of capacity and its variability from location to location is shown in Figure 5.15 with each color swatch representing measurements at a fixed location with time. As an alternative visualiza-

www.manaraa.com

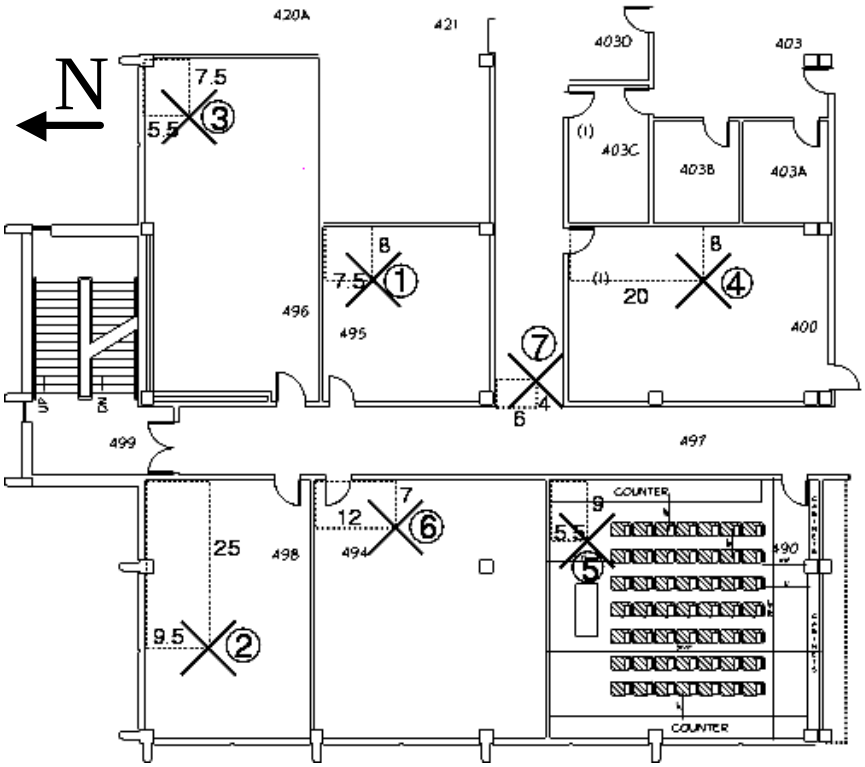

Figure 5.13: Measurement locations in northeast section of Clyde Bldg. 4th floor.

tion of the performance, the mean of these ratios over individual measurement sets is displayed as a function of SNR in Figure 5.16.

www.manaraa.com

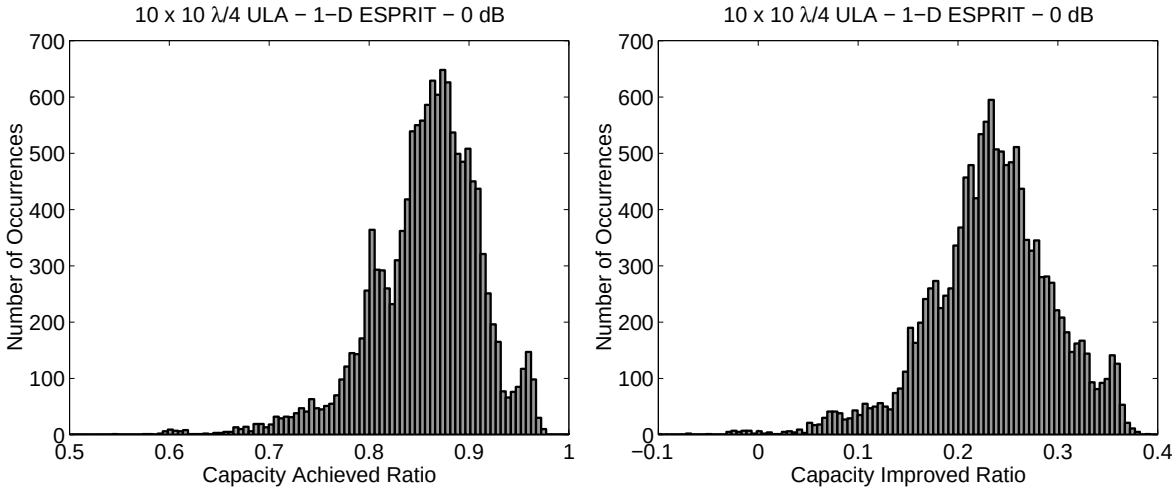

Figure 5.14: Typical histograms of capacity achieved ratio (left) and capacity improved ratio (right) - 1-D ESPRIT feedback over all H measurements - SNR = 0 dB

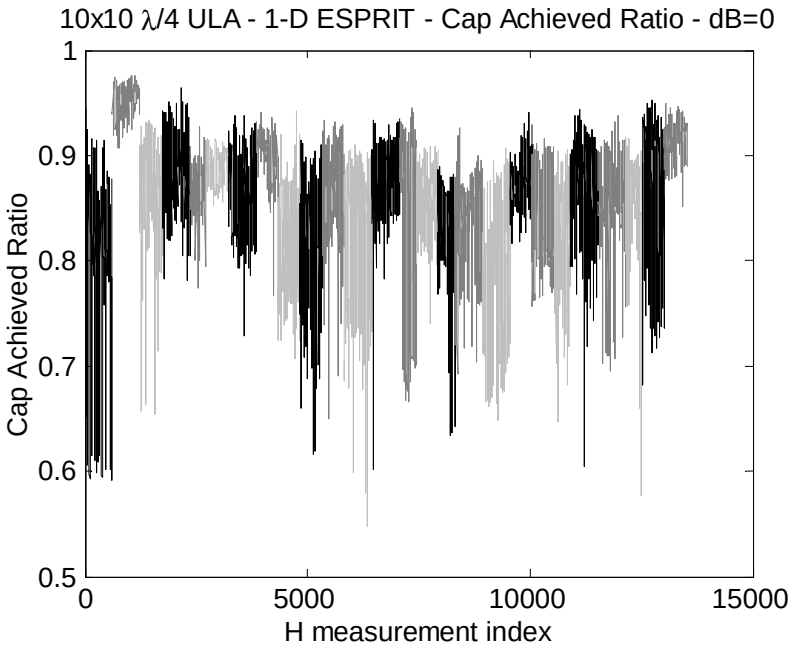

Figure 5.15: Mean capacity achieved ratio - 1-D ESPRIT feedback over all H measurements - SNR = 0 dB

www.manaraa.com

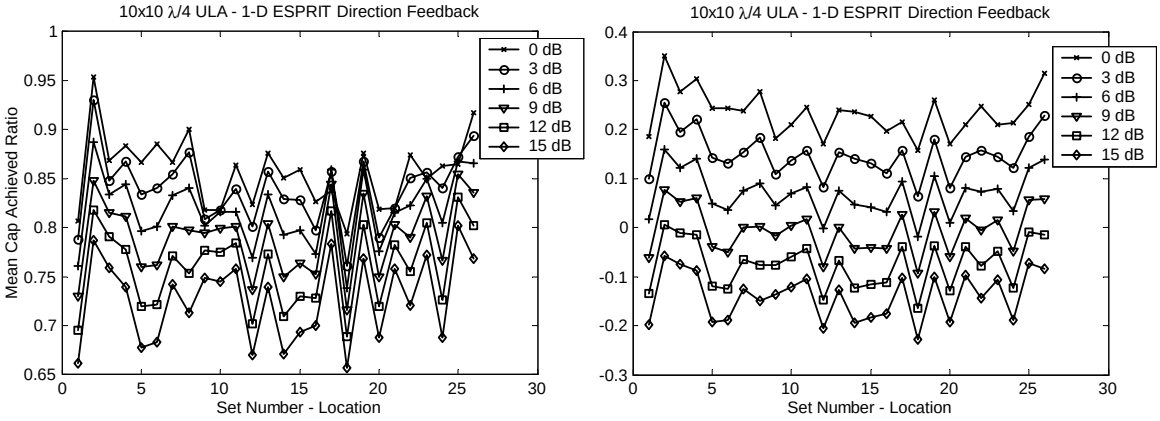

Figure 5.16: Mean capacity achieved ratio (left) and mean capacity improved ratio (right) - 1-D ESPRIT feedback

www.manaraa.com

Figure 5.17 shows complementary CDF representations of the capacity performance ratios for 1-D ESPRIT over the range of SNR values. These plots are useful to determine the percentage of measured channel realizations had capacity performance ratios equal to or greater than a particular value. Over the set of all measurements, the 1-D ESPRIT feedback algorithm gave the best capacity performance, similar to the results observed in the simulation data. Figure 5.18 shows a histogram of the selected value of N_{rays} aggregated over all 26 measurement locations. It is interesting to note that channels with order less than 5 occurred much less frequently. In viewing the raw data, these low order channels occurred in tight bunches dispersed among higher order measurements, rather than being evenly distributed through the data. Once the channel order was detected at 5 or above, the distribution was fairly uniform over the values from 5 to 9. Figure 5.19 shows a comparison of the number of eigenchannels with allocated energy in the waterfilling solution compared with the number of eigenchannels used with the direction-based feedback. As expected, the number of eigenchannels increases with SNR, but the direction feedback utilized fewer eigenchannels and increases more slowly with SNR.

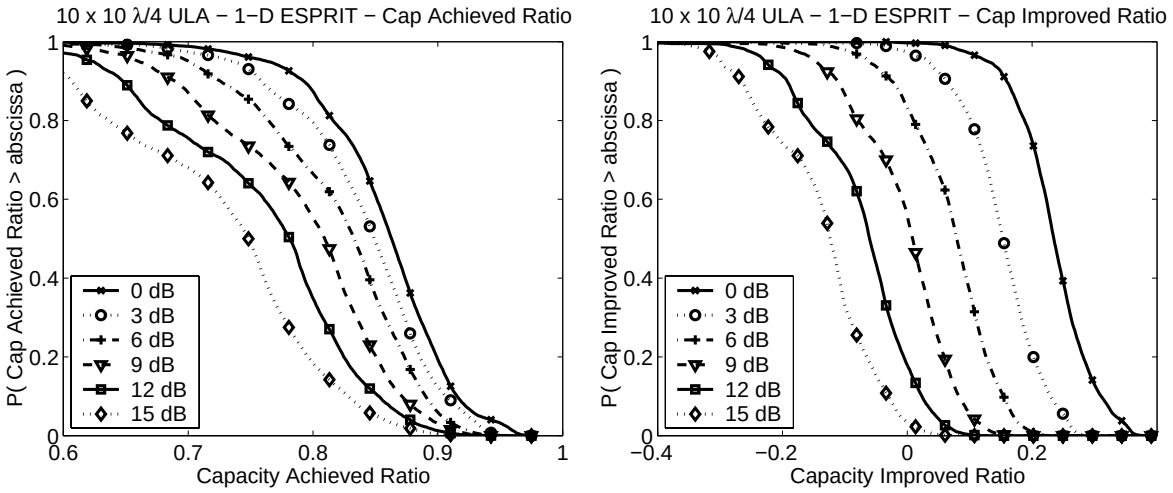

Figure 5.17: CCDF's of capacity achieved ratio (left) and capacity improved ratio (right) - 1-D ESPRIT feedback over all H measurements

www.manaraa.com

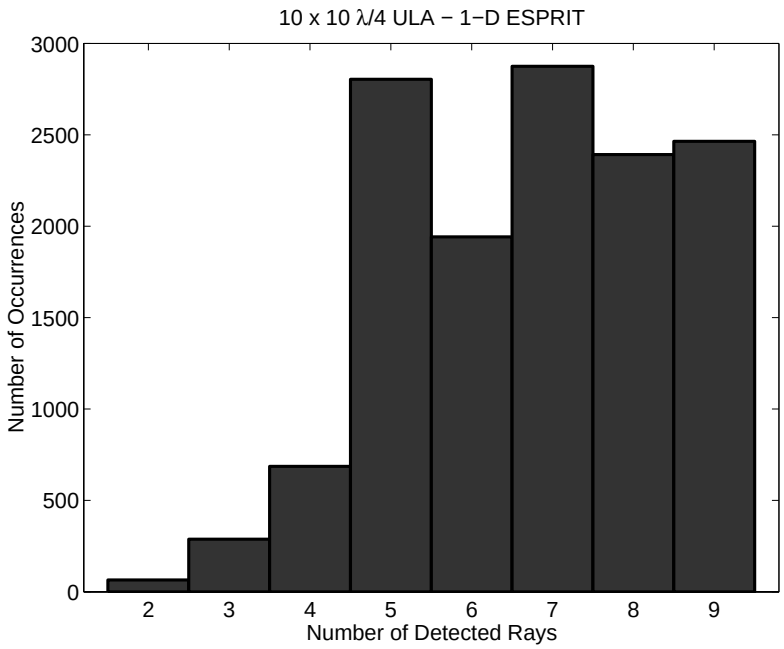

Figure 5.18: Histogram of selected N_{rays} value - 1-D ESPRIT feedback.

www.manaraa.com

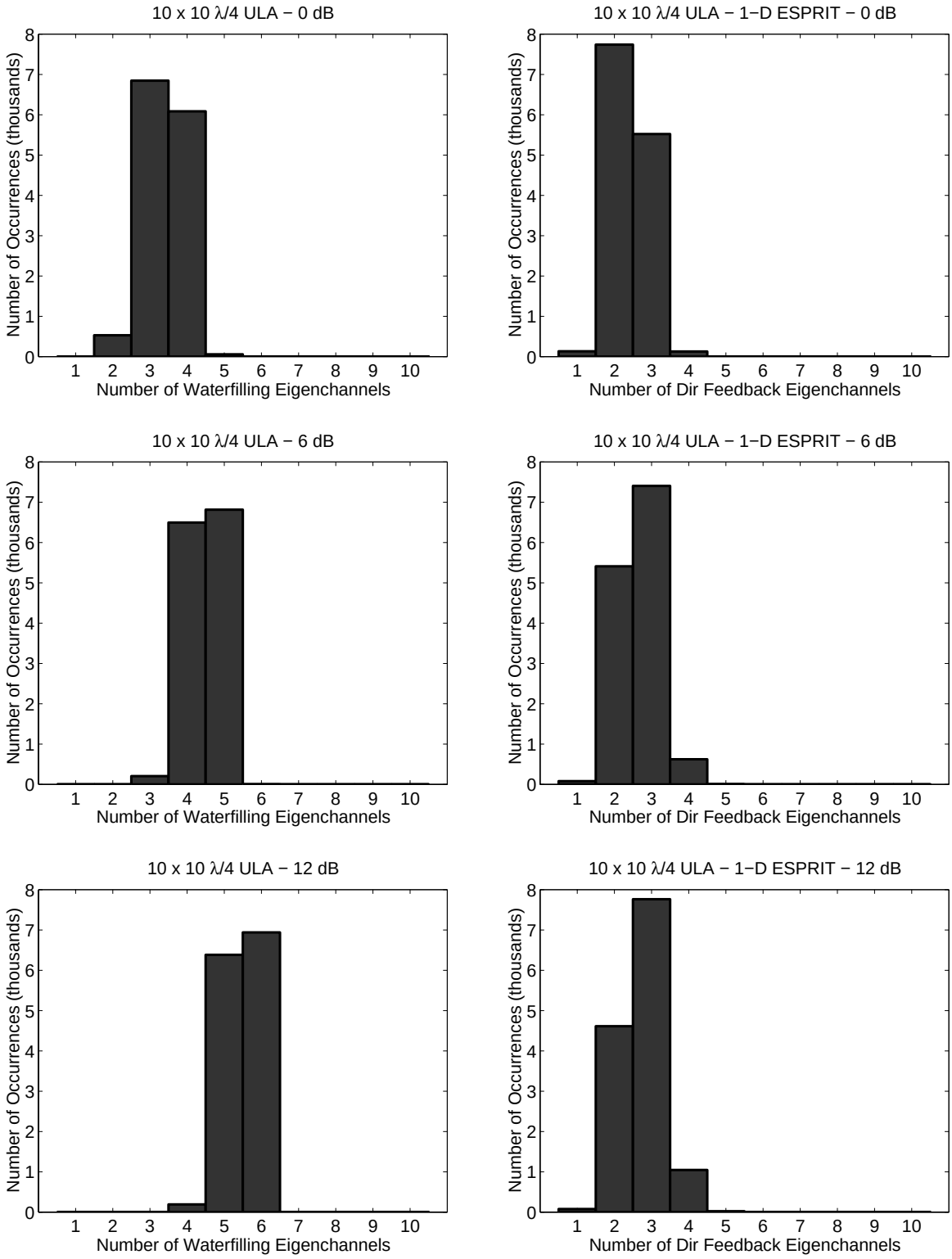

Figure 5.19: Number of waterfilling eigenchannels (left) and number of eigenchannels using 1-D ESPRIT feedback (right) - SNR $\in \{0, 6, 12$ dB$\}$

www.manaraa.com

5.6 Conclusions

From these results, we conclude that using ray model based feedback can significantly improve upon the Fully Blind Transmitter channel capacity. However, there are clear cases where the additional work involved yields only marginal benefits – and in extreme cases even detrimental results. The estimation algorithm that exhibited the best consistent performance was 1-D ESPRIT with iterative ad hoc ray angle pairing. The algorithms investigated here are most relevant at low SNR values when the number of active eigenchannels is low enough to leave significant room for improvement between the Fully Blind Transmitter capacity and the Full CSI Transmitter capacity.

www.manaraa.com

Chapter 6

Covariance Feedback for Improved Capacity

As an alternative to the ray-synthesis feedback for the channel matrix, H, we investigated the use of similar reduced parameter methods for representing the transmitted symbol covariance, Q, as a means of communicating channel state information (CSI). The structure of a covariance matrix provides for some advantages because

- Q is Hermitian symmetric ($Q = Q^H$) (This dictates that the diagonal entries of Q are purely real.) and
- Q is Positive Semi-Definite. (This requires that the eigenvalues of Q are non-negative.)

Q has no physical structure to exploit in ways similar to the discrete ray model. There may be more specific formulations which use ray based parameters to represent Q, but we did not investigate any of these options. A significant advantage of the covariance feedback approach is a reduction in the dimensionality of the feedback space. Where H is a complex matrix of dimension $R \times T$, it has an equivalent real-valued vector space representation of dimension $2RT$. The equivalent real-valued vector space represented by $Q \in \mathbb{C}^{T \times T}$ is only T^2 as seen by the sum of T real entries on diagonal and $T(T-1)/2$ unique complex entries on off diagonals which equals $T + 2\,T(T-1)/2 = T^2$ equivalent real entries. If $R = T$, this allows Q to be fully represented with half as many real parameters as H (T^2 rather than $2RT$).

Our feedback approach represents an approximate Q as a linear combination of Hermitian symmetric matrices where i takes values from a feedback set, $i \in S_f \subseteq$

www.manaraa.com

$\{1, \ldots, T^2\}$, as in

$$Q_f = Q_{feedback} = \sum_{i \in S_f} x_i \, Q_i \, , \tag{6.1}$$

where $Q_i = Q_i^H$ and $x_i \in \mathbb{R}$ for all values of i. The cardinality of the set S_f is N_{Qi}. The Q_i's are assumed to be pre-arranged so that they do not need to be transmitted in order to form Q_f. If N_{Qi} is relative small, the values of i may also be transmitted to identify the set S_f. But, as N_{Qi} takes larger values, it may be more efficient to assume that $S_f = \{1, \ldots, T^2\}$ and transmit $x_i = 0$ for unused i values. The values for N_{Qi} and x_i are selected using some optimality criteria. The two criteria investigated in this work are:

- LS - minimization of the squared error between $Q_{waterfilling}$ and Q_f.
- MAXDET - maximization of the determinant $\det(I + H\,Q_f H^H)$.

In both cases, the optimization is carried out subject to the following constraints:

$$\begin{aligned} &\mathrm{tr}(\,Q_f\,) \leq P && \text{(Maximum Power Constraint),} \\ &x^H Q_f \, x \, \geq 0 \;\; \forall \;\; x \in \mathbb{C}^T && \text{(Positive Semi-Definite Constraint).} \end{aligned}$$

Using the feedback information in the x_i's, the transmitter can reconstruct Q_f using Equation 6.1 and shape the covariance of the transmitted symbols by applying

$$x_f = Q_f^{1/2} x_w \, , \tag{6.2}$$

where x_w are the white symbols, i.e. $\mathrm{E}\{\, x_w \, x_w^H \,\} = I_{T \times T}$, and $Q_f^{1/2}$ is calculated from the eigendecomposition of $Q_f = S \Lambda S^H$ as $Q_f^{1/2} = S \Lambda^{1/2}$. This gives a transmit symbol covariance of

$$\begin{aligned} R &= \mathrm{E}\{\, x_f \, x_f^H \,\} = \mathrm{E}\{\, Q_f^{1/2} \, x_w \, x_w^H \, Q_f^{1/2\,H} \,\} \\ &= Q_f^{1/2} \underbrace{\mathrm{E}\{\, x_w \, x_w^H \,\}}_{I} \, Q_f^{1/2\,H} = Q_f^{1/2} \, Q_f^{1/2\,H} = Q_f \, . \end{aligned} \tag{6.3}$$

For well-selected x_i's, the feedback capacity given by

$$C_f = \log \det \left(I + H \, Q_f H^H \right) \tag{6.4}$$

www.manaraa.com

should approach the maximum value given by the waterfilling solution. Ideally, the feedback set, S_f, should be chosen so that C_f approaches the waterfilling capacity using a minimum of feedback information (i.e. as few x_i's as possible).

6.1 Selection of Q_i matrices

In our investigation, we desired Q_i matrices that would meet the Hermitian symmetry requirement and effectively span the space in which Q resides. In situations where a vector representation of Q or Q_i is needed, we make use of the following procedure for converting between complex, Hermitian matrices and purely real vectors which defines the operators $\text{vec}^*(\cdot)$ and $\text{mat}^*(\cdot)$. Given $Q = Q^H$, $\text{vec}^*(Q)$ stacks vertically (1) the diagonal entries of Q, (2) the real parts of the upper diagonal entries taken diagonal-wise, and (3) the imaginary parts of the upper diagonal entries taken diagonal-wise. For example,

$$\text{Let } A = \begin{bmatrix} 1 & 4+7i & 6+9i \\ 4-7i & 2 & 5+8i \\ 6-9i & 5-8i & 3 \end{bmatrix}, \ \text{vec}^*(A) = [\,1\ 2\ \ldots\ 8\ 9\,]^T\,. \tag{6.5}$$

The operator $\text{mat}^*(\cdot)$ is the inverse of $\text{vec}^*(\cdot)$ such that $\text{mat}^*(\,[\,1\ 2\ \ldots\ 8\ 9\,]^T)$ produces A from our example. Any similar procedure may be substituted, so long as it is applied consistently.

We selected T^2 vectors $q_i \in \mathbb{R}^{T^2}$ to form our set of Q_i's, desiring that the q_i's be orthonormal and form Q_i's which are Hermitian symmetric (satisfied by the nature of the $\text{mat}^*(\cdot)$ operator) and positive semi-definite. In practice, however, we found that the orthonormality of the q_i's was mutually exclusive to the PSD requirement of the Q_i's. The following procedure proved sufficient and prevented undesirable behavior in the MAXDET solution by ensuring that the Q_i's are positive semi-definite.

www.manaraa.com

1. $USV^H = \text{svd}(\,\text{rand}(\,T^2, T^2\,)\,); \quad U = [\,u_1\, u_2\, \ldots\, u_{T^2}\,]$
2. $Q_i = \text{mat}^*(u_i)$
3. Enforce PSD:
   (a) eigendecomposition of $Q_i = S\Lambda S^H$
   (b) $\Lambda_{j,j} = \min(\,0\,, \Lambda_{j,j}\,)$
   (c) $Q_i = S\Lambda S^H$
4. $Q_i = Q_i/\text{tr}(\,Q_i)$
5. $q_i = \text{vec}^*(\,Q_i)$

6.2 Construction of the Feedback Set

We used an ad hoc construction process to determine the members of the feedback set, S_f. Initializing with the empty set, $S_f = \emptyset$, all the members of the set $S_{unused} = \{1, \ldots, T^2\}$ are considered one at a time. For each $j \in S_{unused}$ the optimum value for the x_i's is calculated using $i \in S_{test} = S_f \cup \{j\}$, and the feedback capacity, C_{fj} is calculated using Equation 6.4. The element of S_{unused} which produces the maximum value for C_{fj} is identified as j_{max} and selected for inclusion into $S_f = S_f \cup \{j_{max}\}$. The element j_{max} is removed from S_{unused}. This process may be repeated, adding one member to S_f from each iteration, until all members of S_{unused} are removed, the size of S_f exceeds some allowed threshold, or the marginal gains in C_f are not sufficient to justify increasing the amount of feedback information to be transmitted.

6.3 LS Feedback Determination

Given a set of i values, such as the set S_{test} described in the previous section, we wish to find the values of the x_i's which minimize the squared error between Q_f and Q_{wf} (from the waterfilling solution) using $i \in S_{test}$ subject to the constraints that $\text{tr}(\,Q_f\,) \leq P$ and that Q_f be positive semi-definite. We start with a conventional

www.manaraa.com

least squares solution as follows:

$$q_{wf}^{*} = \mathrm{vec}^{*}(Q_{wf})$$

$$V = \left[\mathrm{vec}^{*}(Q_i^{(1)}) \quad \cdots \quad \mathrm{vec}^{*}\left(Q_i^{(N_{Qi})}\right) \right]$$

$$\mathbf{x}_{LS} = V^{\dagger}\, q_{wf}^{*}\,. \tag{6.6}$$

The feedback covariance is then formed using

$$Q_{LS} = \sum_{i \in S_{test}} x_i\, Q_i = \mathrm{mat}\left(\left[\mathrm{vec}(Q_i) \quad \cdots \quad \mathrm{vec}(Q_{N_{Qi}}) \right] \mathbf{x}_{LS} \right)\,, \tag{6.7}$$

where the vector $\mathbf{x}_{LS}$ is defined as $[\,x_1 \quad \cdots \quad x_{N_{Qi}}\,]^T$. This formulation allows the pseudoinverse, $V^{\dagger}$, to be calculated using purely real computations because V and Q_{wf}^{*} are real valued.

To ensure that Q_{LS} is positive semi-definite, we decompose it into its eigenstructure and recombine it setting negative eigenvalues to zero if necessary. This process is described step-wise as:

1. $Q_{LS} = S\,\Lambda\,S^{H}$.
2. $\lambda = \mathrm{diag}(\Lambda)$.
3. If no elements of λ are negative, then quit.
4. $\Lambda = \mathrm{diag}(\,\min(0\,,\lambda)\,)$.
5. $Q_{LS} = S\,\Lambda\,S^{H}$.

Finally, the power constraint is enforced by scaling Q_{LS} as in

$$Q_{LS} = \frac{P}{\mathrm{tr}(\,Q_{LS})}\, Q_{LS}\,. \tag{6.8}$$

The feedback capacity, C_f, can now be calculated using Equation 6.4 with Q_{LS} substituted for Q_f:

$$C_{f,\,LS} = \log\det\left(I + H\,Q_{LS}H^{H}\right)\,. \tag{6.9}$$

www.manaraa.com

6.4 MAXDET Feedback Determination

In the process of simulating the LS covariance feedback algorithm, we observed frequent cases where perturbations in the feedback coefficients, x_i, would produce increases in the feedback capacity at the expense of larger squared error. This suggests that while LS feedback determination is tractable with traditional methods, it does not necessarily produce feedback information for maximum capacity. Vandenberghe et. al. have presented a generalized framework for solving determinant maximization problems over a useful class of matrices which include our covariance determination problem [75]. Their determinant maximization problem is formulated using *linear matrix inequality* (LMI) constraints, which have been demonstrated to generalize many common constraints, including those of interest in our problem. In addition, they present a useful interior-point method for solving convex optimization problems where more specialized (and perhaps faster) algorithms may not be applied, and they have made available some extremely useful software, entitled "MAXDET", for either C-code or MATLAB environments [76]. This presentation of the MAXDET problem and its application to covariance feedback draws heavily from both of these references.

6.4.1 General MAXDET Problem

The general framework for MAXDET problems presented in [75] and [76] is

$$\begin{aligned} \text{minimize} \quad & c^T x + \log\det G(x)^{-1} \\ \text{subject to} \quad & G(x) \succ 0 \\ & F(x) \succeq 0\,, \end{aligned} \tag{6.10}$$

where the vector $x \in \mathbb{R}^m$ is the optimization variable. The inequality signs in 6.10 indicate that $G(x)$ is positive definite and that $F(x)$ is positive semi-definite. The matrix functions $G : \mathbb{R}^m \to \mathbb{R}^{l\times l}$ and $F : \mathbb{R}^m \to \mathbb{R}^{n\times n}$ are affine:

$$\begin{aligned} G(x) &= G_0 + x_1 G_1 + \cdots + x_m G_m \\ F(x) &= F_0 + x_1 F_1 + \cdots + x_m F_m\,, \end{aligned}$$

www.manaraa.com

where $G_i = G_i^T$ and $F_i = F_i^T$. The use of LMI constraints allows multiple constraints of varied types to be applied simultaneously. Many examples of the variety of constraints that can be expressed as LMIs can be found in [77] and [78]. One important feature of LMIs is the ability to enforce multiple LMI constraints simultaneously by stacking block diagonally. For example, the following formulations are equivalent:

$$\begin{array}{l} A(x) \succeq 0 \\ B(x) \succeq 0 \end{array} \quad \Longleftrightarrow \quad \left[\begin{array}{cc} A(x) & 0 \\ 0 & B(x) \end{array} \right] \succeq 0 \, . \tag{6.11}$$

Another useful property of LMIs which is found in [79] on page 202 is the means to express a complex LMI of the form

$$F_0 + x_1 F_1 + \cdots + x_m F_m \succeq 0 \, , \tag{6.12}$$

where $F_0, \ldots, F_m$ are complex with $F_i = F_i^H$ and $x \in \mathbb{R}^m$ is a real variable, as a real-valued LMI. This transformation makes use of the fact that

$$X \succeq 0 \iff \left[\begin{array}{cc} \Re X & -\Im X \\ \Im X & \Re X \end{array} \right] \succeq 0 \, , \tag{6.13}$$

where $\Re X$ and $\Im X$ are, respectively, the real and imaginary parts of some complex matrix, X. The "MAXDET" software only accepts real-valued arguments, so this equivalency allows conversion of complex-valued MAXDET problems to a corresponding split real and imaginary component format.

6.4.2 Formulation of Feedback Determination as MAXDET problem

We develop the MAXDET formulation for the Feedback Determination problem by first composing it as a complex-valued MAXDET problem and then using the transformation in 6.13 to express it as an equivalent real-valued problem suitable for the "MAXDET" software. The objective is to identify the feedback information that maximizes the ergodic capacity determinant where the transmit symbol covariance equals Q_f. Using the substitution $Q_f = \sum_{i \in S_f} x_i \, Q_i$ from Equation 6.1, this can be

www.manaraa.com

expressed as

$$\text{maximize} \quad \log\det(I + H\,Q_f H^H) = \log\det\left(I + \sum_{i\in S_f} x_i\,H\,Q_i H^H\right). \tag{6.14}$$

To convert this into the minimization operation used by MAXDET, we multiply the objective by -1 and apply the properties of the log and det operators to obtain

$$\text{minimize} \quad -\log\det\left(I + \sum_{i\in S_f} x_i\,H\,Q_i H^H\right) = \log\det\left(I + \sum_{i\in S_f} x_i\,H\,Q_i H^H\right)^{-1}, \tag{6.15}$$

which fits the general MAXDET objective function with the linear component set to zero, $c = 0$. The argument of the determinant can be written as an affine function, $G(x)$, using $G_0 = I$ and $G_i = H\,Q_i H^H$.

The maximum power constraint can be adapted to the LMI format as a scalar quantity by algebraic manipulation:

$$\begin{aligned} \operatorname{tr}(\,Q_f\,) &\le P \\ \operatorname{tr}\Big(\sum_{i\in S_f} x_i\,Q_i\Big) &\le P \\ \sum_{i\in S_f} x_i\,\operatorname{tr}(\,Q_i\,) &\le P \\ P - \sum_{i\in S_f} x_i \operatorname{tr}(\,Q_i\,) &\ge 0\,. \end{aligned} \tag{6.16}$$

This constraint results in a scalar affine function, $F^{(1)}(x)$, by assigning $F_0^{(1)} = P$ and $F_i^{(1)} = -\operatorname{tr}(\,Q_i\,)$.

The positive semi-definite constraint for Q_f is immediately recognizable as an LMI

$$Q_f = \sum_{i\in S_f} x_i\,Q_i \;\succeq\; 0\,, \tag{6.17}$$

which can be written as $F^{(2)}(x)$ using $F_0^{(2)} = 0$ and $F_i^{(2)} = Q_i$. Putting the objective and constraint functions together (using the block diagonal structure in Equation 6.11

www.manaraa.com

to combine $F^{(1)}(x)$ and $F^{(2)}(x)$ into a single function, $F(x)$) results in the complex-valued MAXDET problem given by

$$\begin{aligned} \text{minimize} \quad & \log\det\Big(\overbrace{I+\sum_i x_i\, H\, Q_i H^H}^{G(x)}\Big)^{-1} \\ \text{subject to} \quad & G(x) \succ 0 \\ & \begin{bmatrix} P-\sum_i x_i \operatorname{tr}(Q_i) & 0_{1\times T} \\ 0_{T\times 1} & \sum_i x_i\, Q_i \end{bmatrix} \succeq 0\ , \end{aligned} \tag{6.18}$$

where i is taken as $i \in S_f$ and both $G_i = G_i^H$ and $F_i = F_i^H$ have complex entries.

In order to translate this complex-valued problem into a real-valued version suitable for the "MAXDET" software, we must make one additional observation. While the constraint LMI involving $F(x)$ may be split directly using Equation 6.13, the determinant operator applied to $G(x)$ is non-linear and prevents a direct transformation of the objective function. However, by taking advantage of the fact that $\det(G(x))$ is non-negative, we can use the observation that for any complex Hermitian matrix, $X = X^H$,

$$\det\begin{bmatrix} \Re X & -\Im X \\ \Im X & \Re X \end{bmatrix} = \det(X)^2\ , \tag{6.19}$$

where $\Re X$ and $\Im X$ are the real and imaginary parts of X, respectively. Since $G(x)$ is Hermitian symmetric for all x, the optimization of $\det G(x)$ is equivalent to optimizing

$$\text{max.}\ \ \det\begin{bmatrix} \Re G(x) & -\Im G(x) \\ \Im G(x) & \Re G(x) \end{bmatrix} = \det\Big(G(x)\Big)^2 \Longleftrightarrow \text{max.}\ \ \det G(x)\ , \tag{6.20}$$

where $G(x) = \Re G(x) + j\,\Im G(x)$ represents the decomposition of $G(x)$ into its real and imaginary components.

www.manaraa.com

Bringing all of the pieces together, we can write the Feedback Determination problem in MAXDET form with all real-valued quantities:

$$\begin{aligned} &\text{minimize} && \log\det G^*(x)^{-1} = -\log\det \begin{bmatrix} \Re G(x) & -\Im G(x) \\ \Im G(x) & \Re G(x) \end{bmatrix} \\ &\text{subject to} && G^*(x) \succ 0 \\ & && F^*(x) = \begin{bmatrix} P - \sum_i x_i \operatorname{tr}(Q_i) & 0_{1\times T} & 0_{1\times T} \\ 0_{T\times 1} & x_i \Re Q_i & -x_i \Im Q_i \\ 0_{T\times 1} & x_i \Im Q_i & x_i \Re Q_i \end{bmatrix} \succeq 0\,. \end{aligned} \tag{6.21}$$

All instances of i are taken as $i \in S_f$, and the function $G(x)$ is used here as defined in Equation 6.18, $G(x) = I + \sum_i x_i\, H\, Q_i H^H$. Explicitly, the functions $G^*(x)$ and $F^*(x)$ are formed from:

$$G_0^* = \begin{bmatrix} I_{R\times R} & 0_{R\times R} \\ 0_{R\times R} & I_{R\times R} \end{bmatrix} = I_{2R\times 2R}$$

$$G_i^* = \begin{bmatrix} \mathfrak{Re}\left\{H\, Q_i H^H\right\} & -\mathfrak{Im}\left\{H\, Q_i H^H\right\} \\ \mathfrak{Im}\left\{H\, Q_i H^H\right\} & \mathfrak{Re}\left\{H\, Q_i H^H\right\} \end{bmatrix}$$

$$F_0^* = \begin{bmatrix} P & 0_{1\times 2T} \\ 0_{2T\times 1} & 0_{2T\times 2T} \end{bmatrix} = \operatorname{diag}\left(\left[\, P\ 0_{1\times 2T} \,\right]\right)$$

$$F_i^* = \begin{bmatrix} -\operatorname{tr}(Q_i) & 0_{1\times T} & 0_{1\times T} \\ 0_{T\times 1} & \Re Q_i & -\Im Q_i \\ 0_{T\times 1} & \Im Q_i & \Re Q_i \end{bmatrix}\,. \tag{6.22}$$

The solution to this problem produces x_i values which can be used to synthesize Q_{MAXDET} using

$$Q_{MAXDET} = \sum_{i\in S_{test}} x_i\, Q_i = \left[\, \operatorname{vec}(Q_i) \ \cdots\ \operatorname{vec}(Q_{N_{Q_i}}) \,\right] \mathbf{x}_{MAXDET}\,, \tag{6.23}$$

where the vector $\mathbf{x}_{MAXDET}$ is defined as $[\, x_1 \ \cdots\ x_{N_{Q_i}} \,]^T$. In contrast to the LS solution, Q_{MAXDET} already meets the PSD and power constraints, so they are not

www.manaraa.com

enforced separately. Once Q_{MAXDET} is known, the feedback capacity can be calculated using Equation 6.4 with Q_{MAXDET} substituted for Q_f:

$$C_{f,\,MAXDET} = \log\det\left(I + H\,Q_{MAXDET}H^H\right). \tag{6.24}$$

6.5 Simulation Results

The Covariance Feedback algorithms described in this section were tested with Monte Carlo simulations to compare their performance. The channel matrices were formed with *i.i.d.* elements with a Circular Complex Gaussian distribution of zero mean and unit variance in both the real and imaginary components. Each random channel matrix was scaled to have an average unit modulus for its entries using Equation 5.87 as indicated below:

$$H = H\sqrt{\frac{M\,N}{\sum_{i=1}^{M}\sum_{j=1}^{N}|H_{i,j}|^2}} = H\sqrt{\frac{M\,N}{\|\,H\,\|_F^2}} = H\,\frac{\sqrt{M\,N}}{\|\,H\,\|_F}. \tag{6.25}$$

The set of Q_i matrices used to represent the feedback covariance was randomly selected at the beginning of the experiment as described on page 108 and used without alteration for all Monte Carlo trials.

In all simulations, the transmit and receive arrays are Uniform Linear Arrays with equal numbers of elements, and the quantity $Nant$ is used to represent the number of antennas in these arrays: $Nant = T = R$. Each simulation was run with 500 trials as the array sizes and Signal-to-Noise ratio (SNR) are varied.

6.5.1 LS Covariance Feedback

Figure 6.1 shows typical results from the LS covariance feedback Monte Carlo trials displayed as a CCDF of Capacity Ratio as the number of feedback terms, N_{Qi}, is varied. To simplify the legend, we took advantage of the fact that the capacity ratio generally increases monotonically with N_{Qi}. In this example plot, the value of N_{Qi} has been explicitly labeled for several traces to illustrate this point. The leftmost trace shows the capacity ratio when no feedback is used, and uniform eigenvalues are

www.manaraa.com

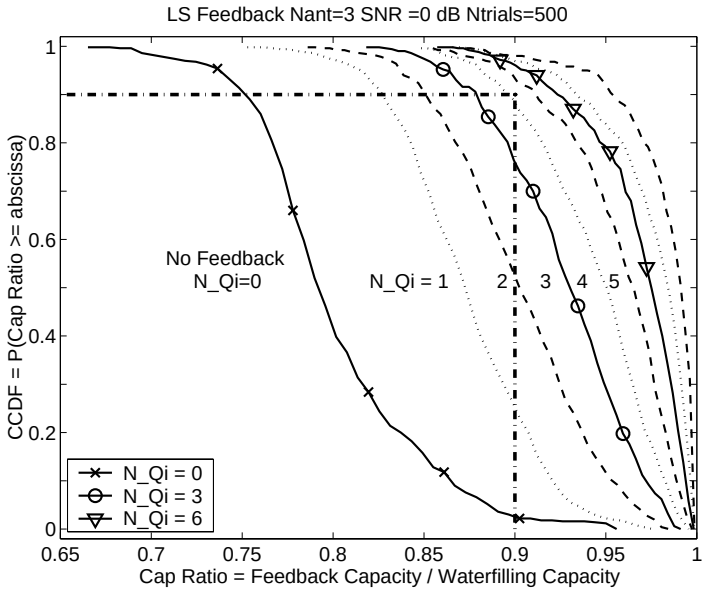

Figure 6.1: CCDF of LS capacity ratio Nant = 3 SNR = 3 dB 500 trials

used for the transmitted signal covariance. As we move to the traces to the right, N_{Qi} increases. The highlighted CCDF point illustrates that for $N_{Qi} = 4$, the probability that the capacity ratio is greater than or equal to 0.9 is approximately 90%. This point was used with varying values of SNR and number of antenna elements ($Nant$) to determine the minimum number of feedback terms needed to ensure that the capacity ratio was at least 0.9 with a probability of 90% or greater. These minimum values for N_{Qi} are shown in Table 6.1 for both LS and (MAXDET) methods. In some cases, there may be significant cushion present between the CCDF and the (0.9, 90%) point. The plots in Figure 6.2 show CCDF's for $Nant = 3$ as the SNR is varied over the set {0, 3, 6, 10 dB}. As expected, the marginal capacity benefit of adding another feedback element is the greatest for the first few terms and decreases as more feedback is used. Also, as the SNR increases, the performance of uniform eigenvalues (no feedback case) improves to the point that it may outperform cases with small values of N_{Qi} some fraction of the time. (Note that the abscissa axis limits are shifted for the two highest SNR values.) These behaviors are consistently observed for larger array sizes.

www.manaraa.com

Table 6.1: Minimum number of feedback values, N_{Qi}, using LS (MAXDET) to ensure $P(\text{Capacity Ratio} \geq 0.9) \geq 90\%$.

Nant \ **SNR**	**0 dB**	**3 dB**	**6 dB**	**10 dB**
3	5 (5)	4 (3)	2 (2)	1 (1)
4	6 (5)	4 (3)	2 (2)	0 (0)
5	8 (6)	5 (4)	2 (1)	0 (0)

Another means of analyzing these results is to look at the statistics of the quantity $\Delta\text{Capacity} = \text{Capacity}(N_{Qi}+1) - \text{Capacity}(N_{Qi})$, which indicates the marginal change in capacity resulting when one additional feedback term is used. The traces in Figure 6.3 show the behavior of ΔCapacity using Complementary CDF curves as N_{Qi} is varied. The indicated point illustrates the probability that increasing N_{Qi} from 0 to 1 will result in a capacity increase of at least 0.25 bits/sec/Hz is 40%. This type of graph clearly shows the decreasing marginal returns in capacity as additional feedback terms are used. These statistics could be used to evaluate the merit of increasing the amount of feedback information against the cost of feedback transmission. Figure 6.4 shows the same type of CCDF curves for Nant=3 as the SNR is varied over the set $\{0,\ 3,\ 6,\ 10\ \text{dB}\}$. Note that for higher SNR cases, the first feedback value is likely to result in a loss of capacity which can be recovered with a higher value of N_{Qi}. Additional figures showing Covariance Feedback performance, including results for larger array sizes. are included in Appendix A.

www.manaraa.com

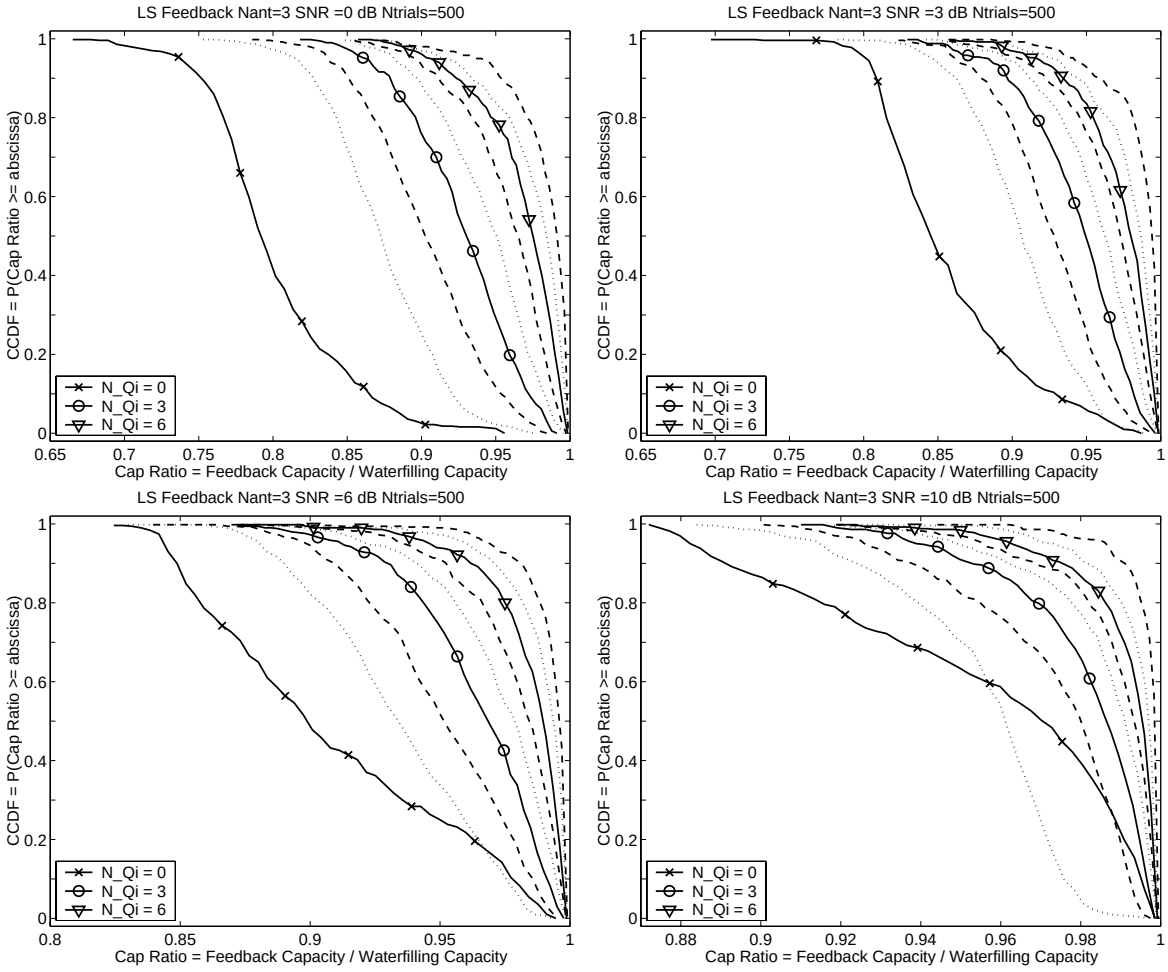

Figure 6.2: CCDF of LS capacity ratio Nant = 3 SNR $\in \{0, 3, 6, 10$ dB$\}$ 500 trials

6.5.2 MAXDET Covariance Feedback

Figure 6.5 shows the results from MAXDET covariance feedback Monte Carlo simulations using the same CCDF of the Capacity Ratio used in the LS results displayed in Figure 6.2. For further specifics regarding the organization of the plot, refer to Figure 6.1. Some perception of the improved performance of MAXDET feedback over the LS method can be gained from Table 6.1 on page 118, which shows that MAXDET meets the $P(\text{Capacity Ratio} \geq 0.9) \geq 90\%$ performance criterion with an equal, and frequently fewer, number of feedback terms.

www.manaraa.com

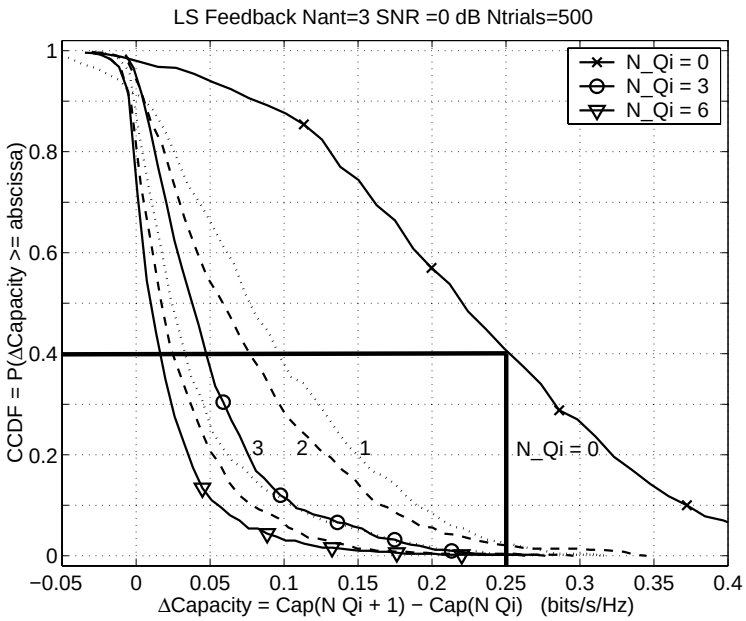

Figure 6.3: CCDF of LS ΔCapacity Nant = 3 SNR = 3 dB 500 trials

The MAXDET performance advantage can be more specifically observed using the statistics of the difference between the MAXDET Capacity Ratio and the LS Capacity Ratio. This CCDF of this quantity, defined as

$$\delta\text{CR} = \text{MAXDET Capacity Ratio} - \text{LS Capacity Ratio}\ , \tag{6.26}$$

is plotted in Figure 6.6 for 3-element arrays over the set of SNR values. It is interesting to note that for $N_{Qi} = 1$, there is no difference between the feedback coefficient calculated by the LS and MAXDET methods, for all observed array sizes and SNR values. Hence, the first trace never deviates from $\delta\text{CR} = 0$. It is clear from these figures, that as the SNR increases, the performance gap between the MAXDET method and the LS method decreases, and eventually both methods produce equivalent results. The performance gains for MAXDET are greatest at the lowest value of SNR. Figure 6.7 shows an exploded portion of the δCR graph for SNR = 0. This data indicates that greatest difference between MAXDET and LS performance occurs for $N_{Qi} = 3$ and 4, and it diminishes gradually as N_{Qi} is increased beyond that point. This characteristic holds true for higher SNR values, except that the progression of δCR increasing to its

www.manaraa.com

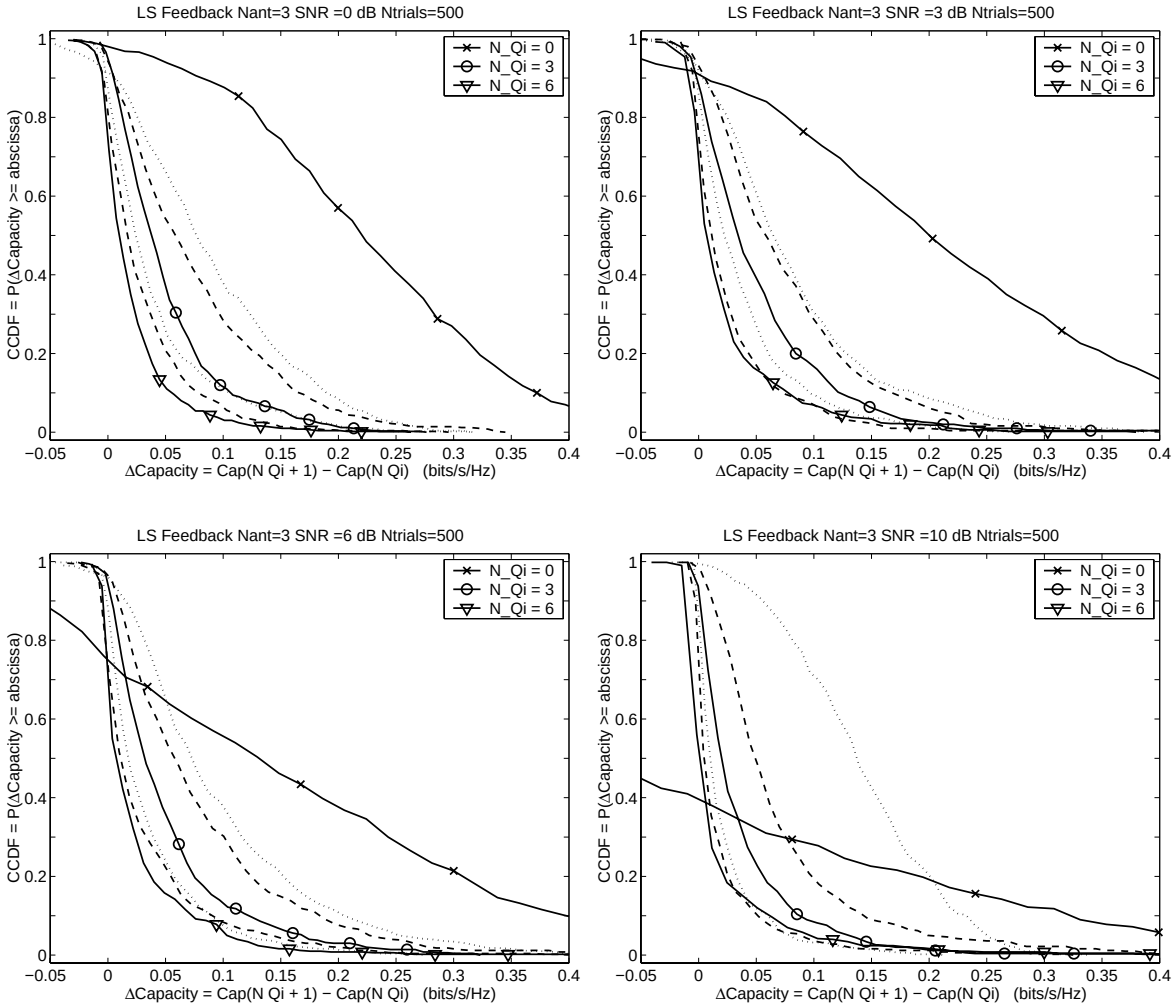

Figure 6.4: CCDF of LS ΔCapacity Nant = 3 SNR ∈ { 0, 3, 6, 10 dB} 500 trials

maximum value and then declining towards 0 takes place over a much wider range of N_{Qi}. In fact, for 4 element arrays, MAXDET's increased performance at the lowest SNR value is remarkably sustained, and it does not totally converge to the LS capacity performance even for higher SNR. This can be seen in Figure 6.8 which illustrates δCR for the 4 antenna case with SNR taking its range of values. Some values of N_{Qi} have been omitted to reduce the number of traces in the plots. The same behaviors are even more pronounced in the δCR plots using 5 elements as displayed in Figure 6.9. Additional plots for the $N_{ant} = 4$ and 5 simulations can be found in Appendix A.

www.manaraa.com

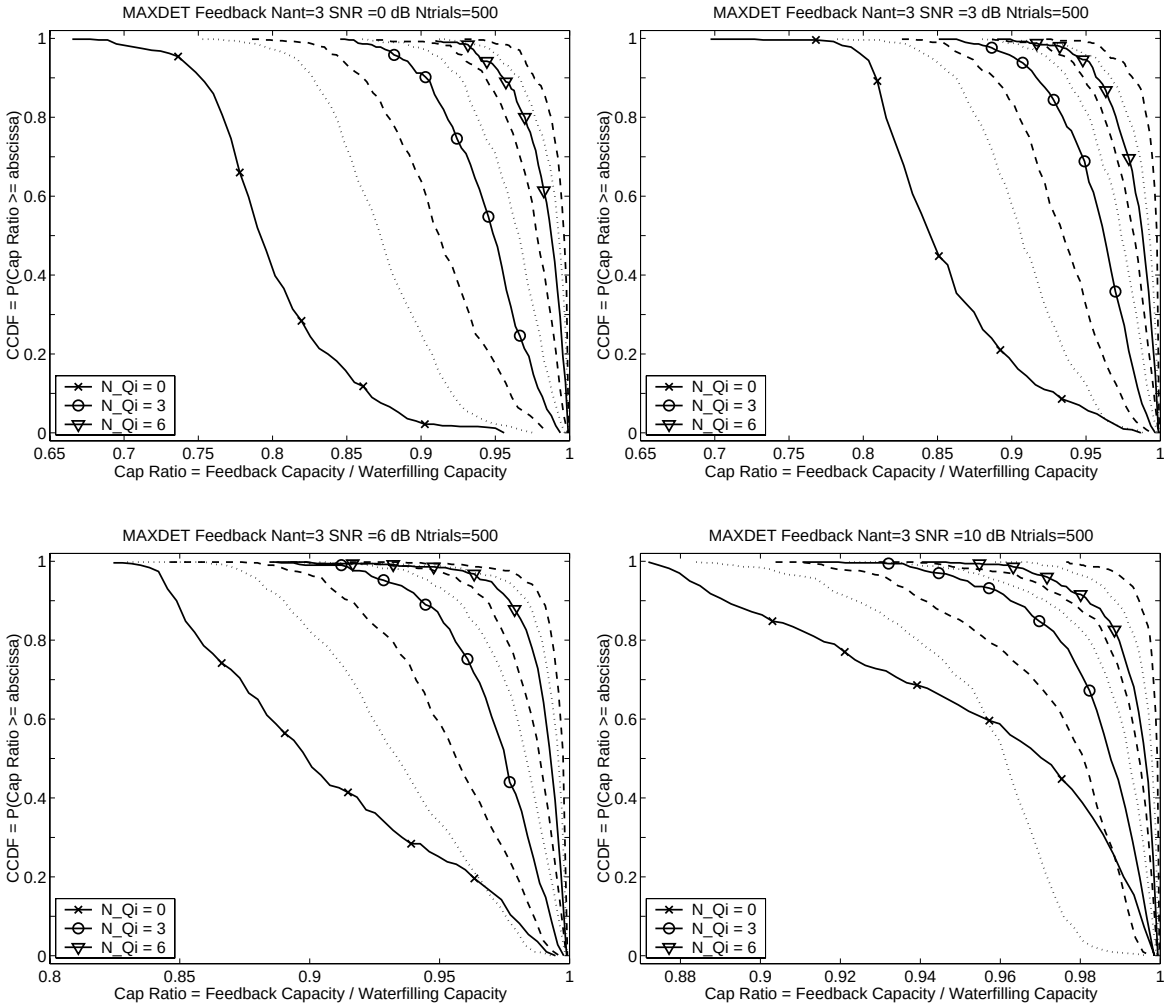

Figure 6.5: CCDF of MAXDET capacity ratio $N_{ant} = 3$ SNR$\in \{0, 3, 6, 10$ dB$\}$ 500 trials

www.manaraa.com

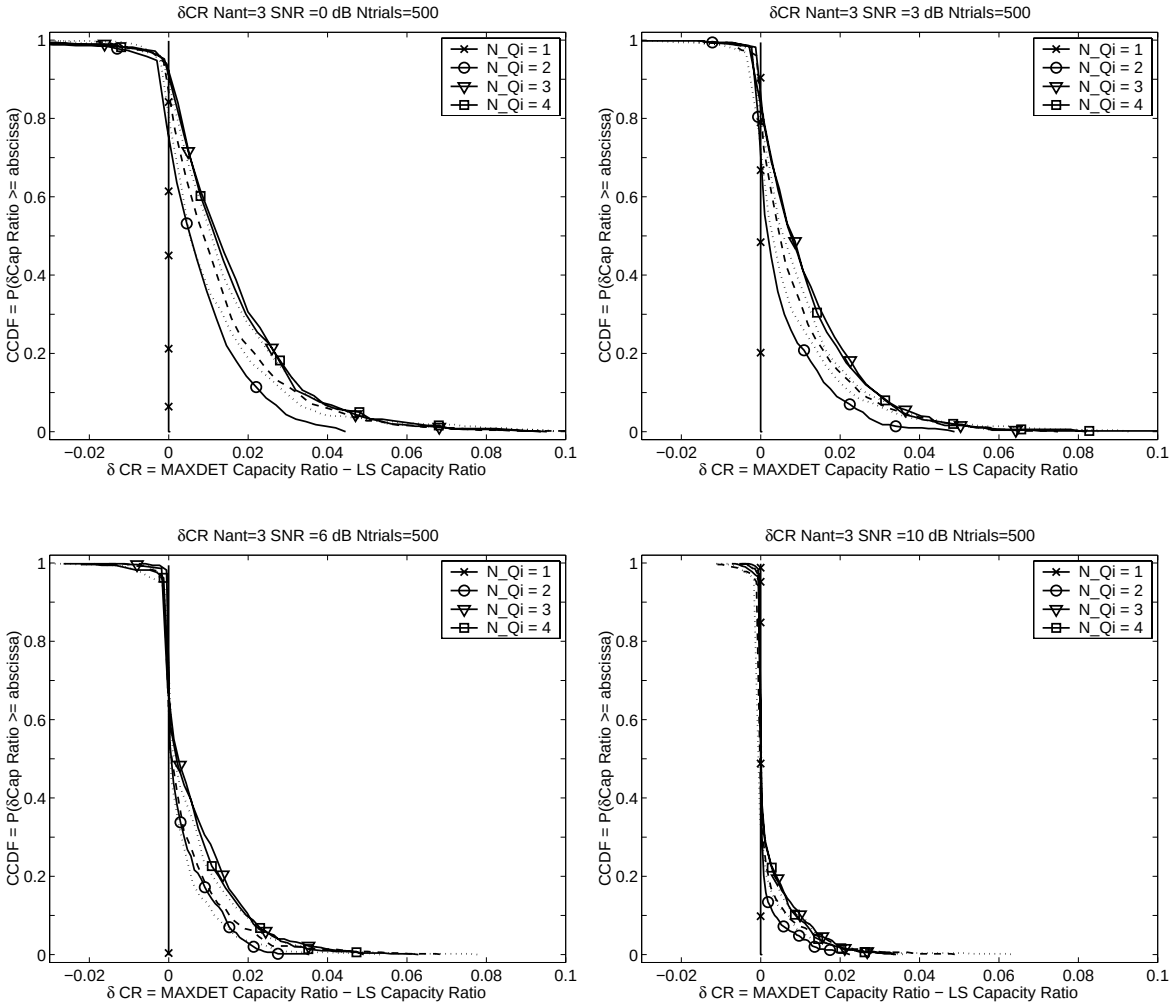

Figure 6.6: CCDF of δCR Nant = 3 SNR $\in \{0, 3, 6, 10$ dB$\}$ 500 trials

www.manaraa.com

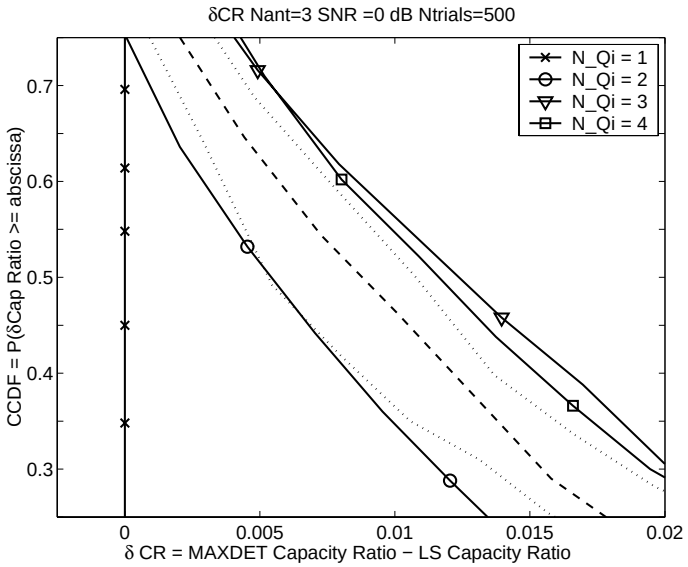

Figure 6.7: CCDF of δCR Nant = 3 SNR = 0 dB 500 trials (exploded view)

www.manaraa.com

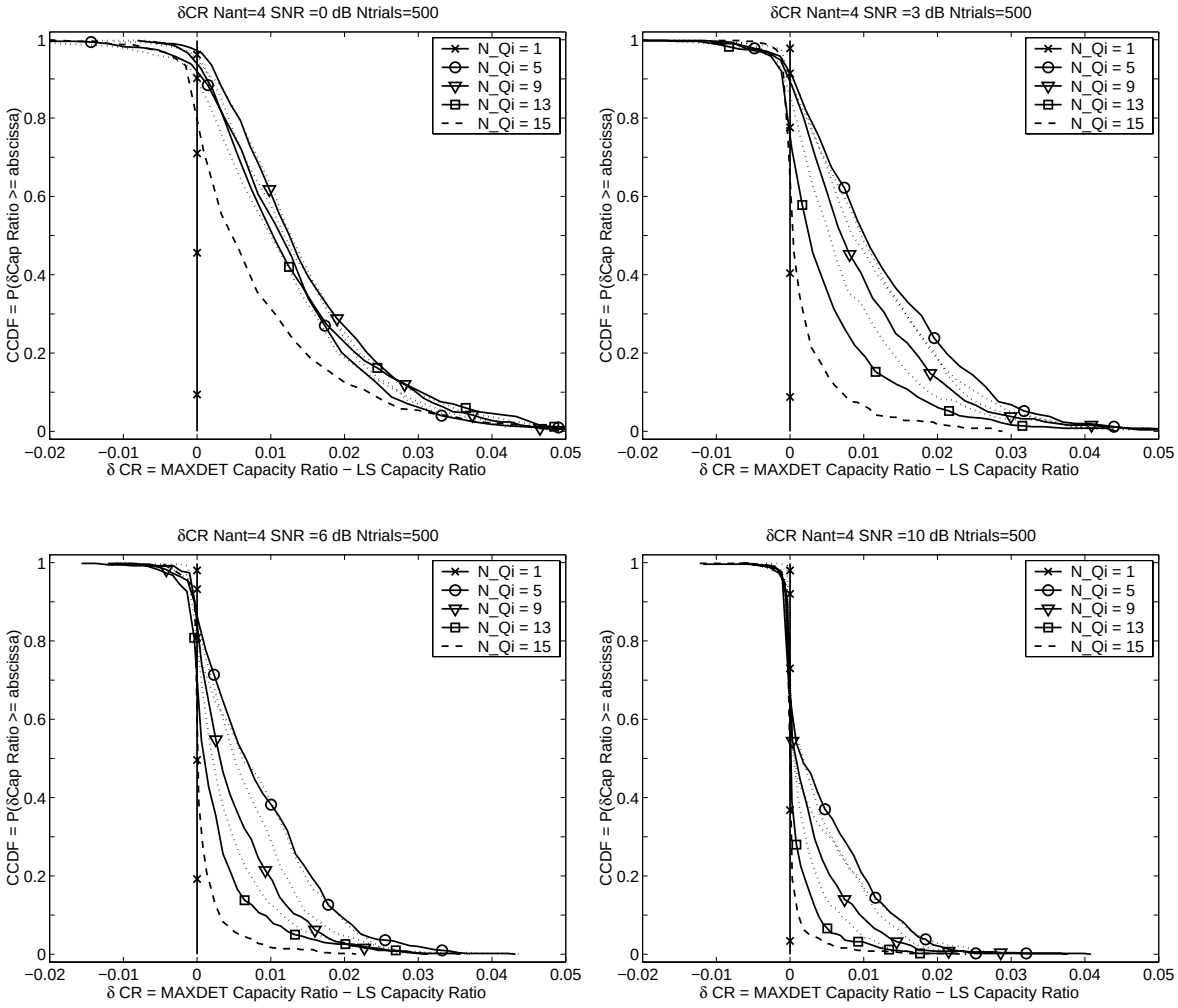

Figure 6.8: CCDF of δCR Nant $= 4$ SNR $\in \{\, 0,\, 3,\, 6,\, 10$ dB$\}$ 500 trials

www.manaraa.com

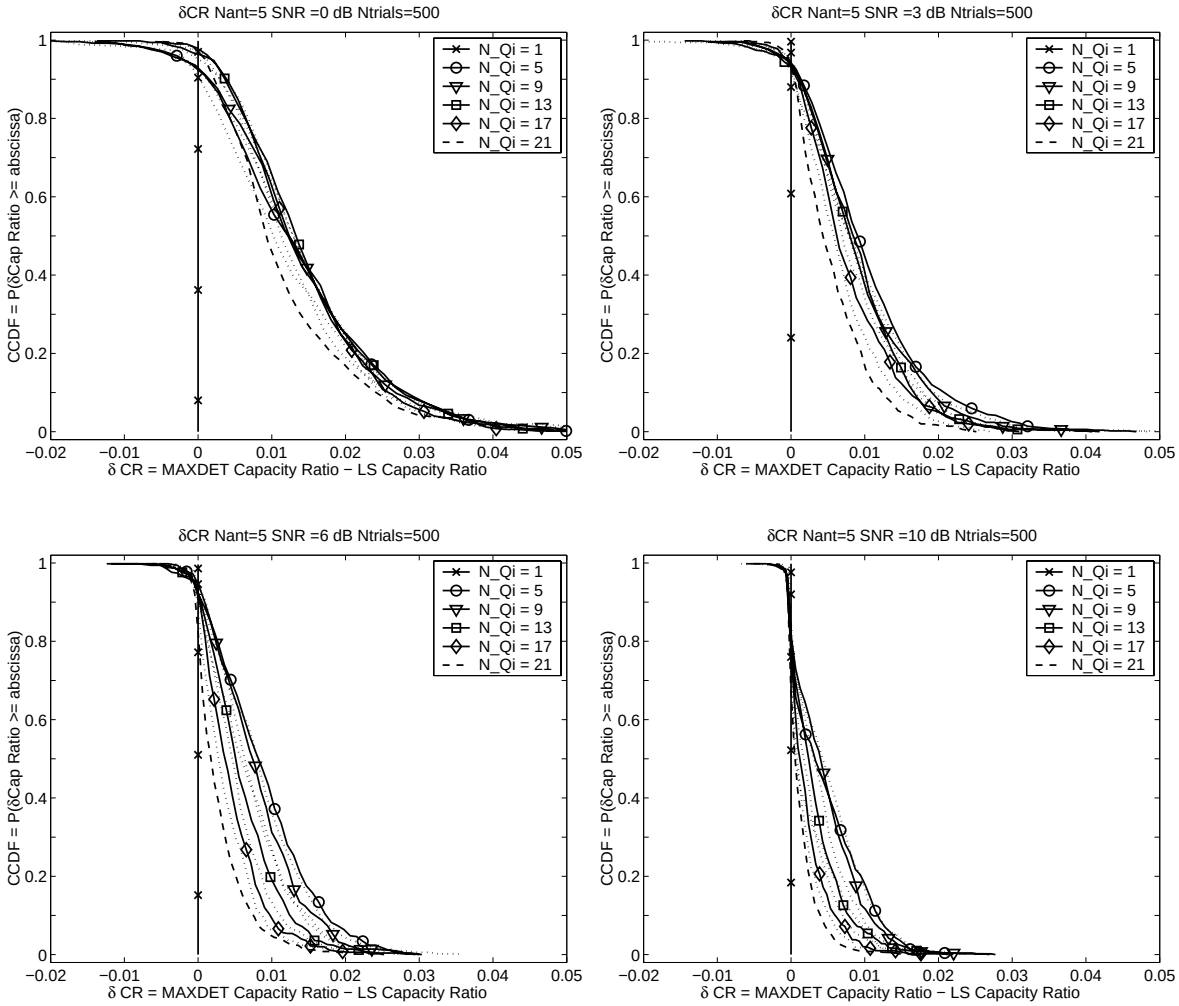

Figure 6.9: CCDF of δCR Nant $= 5$ SNR $\in \{0, 3, 6, 10$ dB$\}$ 500 trials

www.manaraa.com

6.6 2.45 GHz MIMO Channel Sounding Results

The most significant challenge in applying the Covariance Feedback methods described in this chapter to the 2.45 GHz measured channels is dealing with the 10×10 dimension of H where the progressive construction of the feedback set described in Section 6.2 requires exponentially increasing repetitions of the feedback calculations. To be specific, if the maximum number of feedback terms, $N_{Qi} = N^2$, are required for a square channel matrix of dimension $N \times N$, the feedback coefficient solution will need to be repeated $N^2 + (N^2 - 1) + \ldots + 1 = N^2(N^2 + 1)/2$ times. Restricting the feedback set to fewer terms produces some benefits, but the first few terms are the most expensive because the search set begins with its maximum cardinality. However, in order to produce meaniful comparisons with the Ray Model Feedback methods of Chapter 5, the full 10×10 measurements were analyzed using Covariance Feedback. The MAXDET mathod's complexity made it intractable for calculating the covariance feedback solution for each measurement. As an alternative, all available channel measurements were processed with LS Covariance Feedback. For each of the 26 measurement locations, three channel realizations were identified for MAXDET processing by selecting the channels with minimum deviation from the maximum, minimum, and mean Capacity Ratio performance under LS covariance feedback over all values of N_{Qi}. All calculations were performed using 0 dB SNR to parallel the improved performance of the Ray Model feedback methods at this power level.

As a first indication of the covariance feedback results, Figure 6.10 shows the mean value of the Capacity Ratio $= C_{feedback}/C_{waterfilling}$ over all of the measurements at all locations for $N_{Qi} = 0$ (no feedback case) up to a maximum value of $N^2 = 100$. The right plot shows a zoomed portion of the same data. Notice that the slope of the Capacity Ratio versus N_{Qi} begins large and decreases as more feedback terms are added. The maximum and minimum values of the Capacity Ratio are also plotted for each N_{Qi} to show the bounds of the distribution. Figure 6.11 shows the CCDF

www.manaraa.com

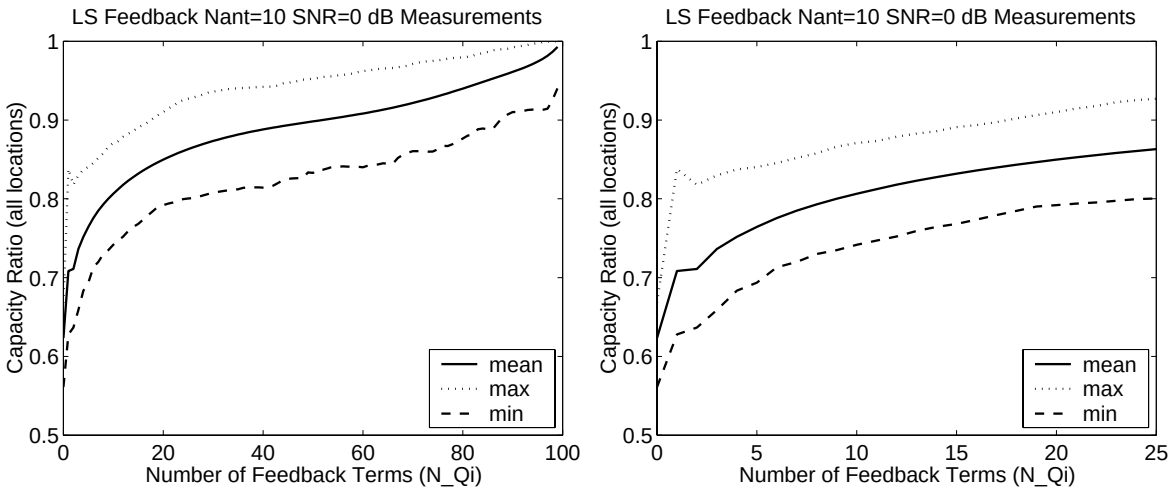

Figure 6.10: Capacity ratio - all locations - LS feedback - SNR 0dB

of capacity ratio over all measurements for two sets of N_{Qi} values. The $N_{Qi} = 0$ curves indicates the "no feedback" case. The region where covariance feedback shows its advantage is in the smaller values of N_{Qi} where the gains per additional term are steepest. For low SNR channels where the number of active eigenchannels is low, covariance feedback makes significant improvements over the no feedback case. Figures 6.10 and 6.11 include plots for small values of N_{Qi} to compare against the no feedback

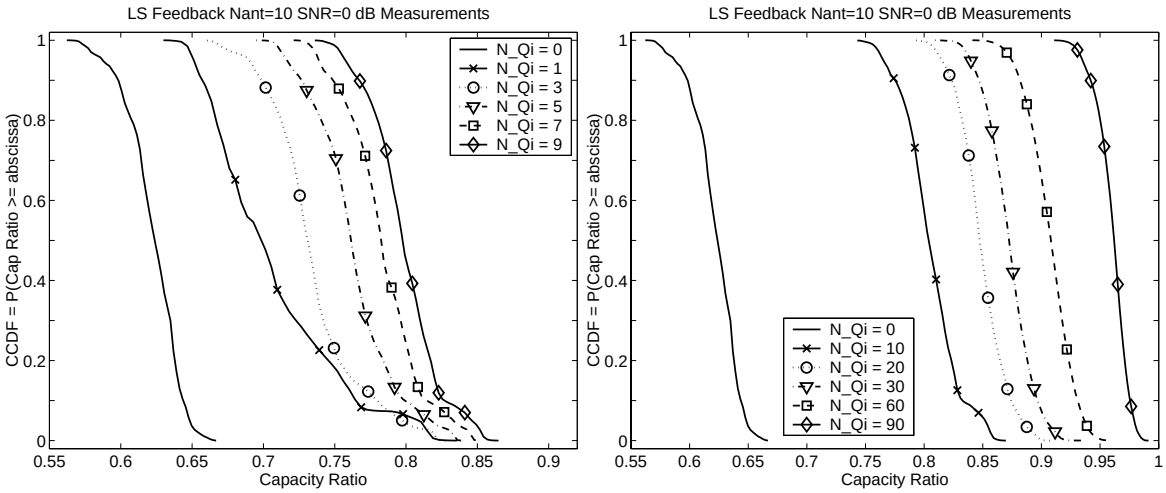

Figure 6.11: CCDF of capacity ratio all locations - LS feedback - SNR 0dB

www.manaraa.com

scenario. Unfortunately, the slope of the curve falls off too quickly, and many feedback terms are required to push the capacity ratio towards its upper limits. For larger N_{Qi} values, the quantity of covariance feedback exceeds the amount of information necessary to feedback the unique entries of Q, and the rising computational burden makes covariance feedback even more disadvantageous.

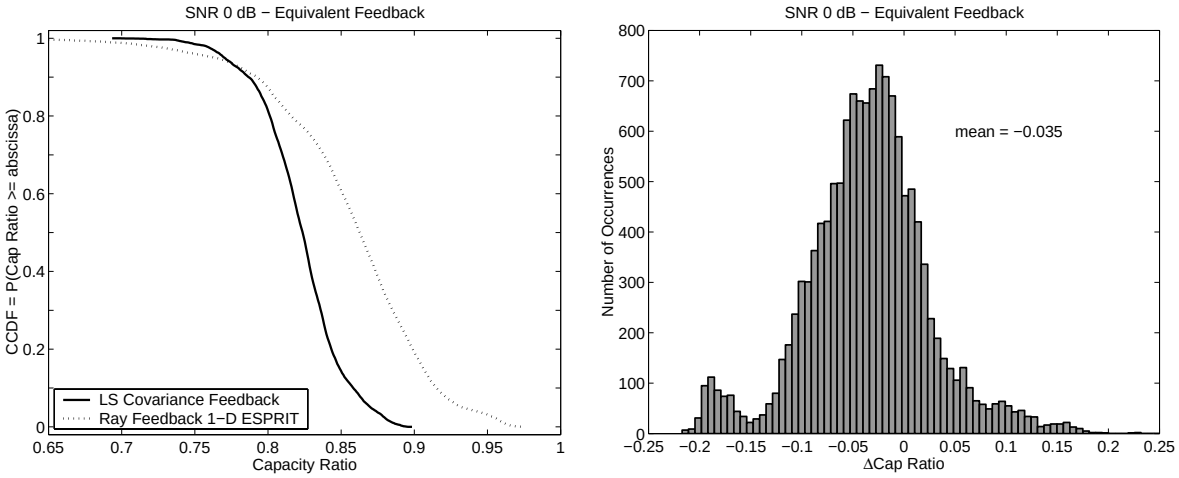

Figure 6.12: Capacity ratio - all locations - LS feedback - SNR 0dB

To further compare the two feedback methods, the capacity ratios can be related using an equivalent amount of feedback information. Because each Q_i contributes only two real-valued feedback parameters (x_i and i) and each ray model feedback value requires four-real valued parameters (ϕ_i, θ_i, and complex β_i), we consider that each ray feedback term represents the equivalent transmission load of two covariance feedback terms. The value of N_{Qi} in this case is selected to equal $2N_{rays}$. Figure 6.12 shows results in terms of the quantity ΔCapacity Ratio = Capacity Ratio using LS Covariance Feedback - Capacity Ratio using Ray Model 1-D ESPRIT Feedback. LS Covariance Feedback gives some relative increases in performace, but it requires too much feedback information in order to yield higher values of Capacity Ratio. Overall, its performance is slightly worse than the Ray Model Feedback using 1-D ESPRIT.

www.manaraa.com

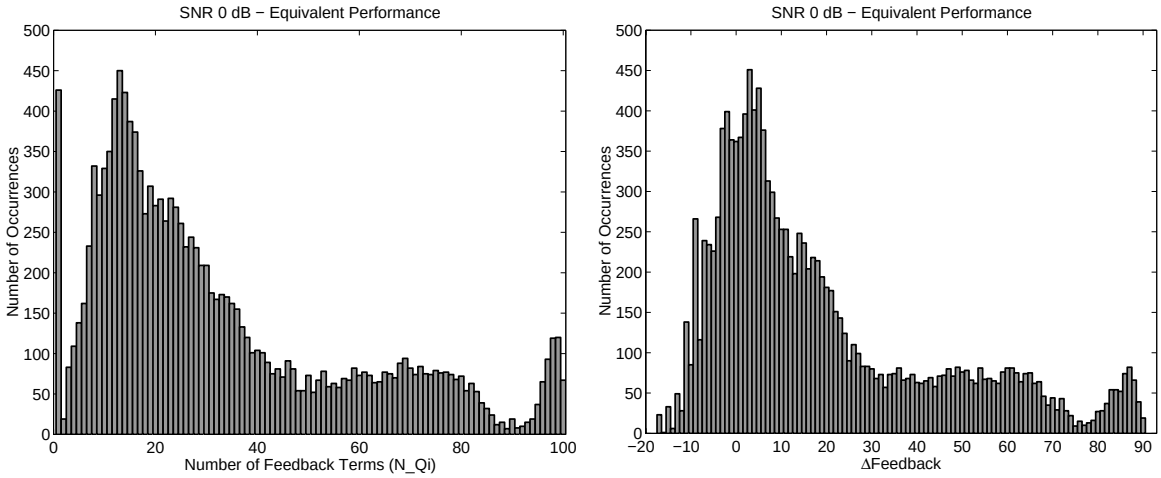

Figure 6.13: Histograms of N_{Qi} and ΔFeedback for equivalent performance

An alternative method is to determine the number of feedback terms required so that the performance using LS Covariance Feedback is equivalent to the 1-D ESPRIT Ray Model Feedback. This data is shown in Figure 6.13. The left histogram shows N_{Qi} for equivalent performance, and the right histogram is of the quantity ΔFeedback = N_{Qi} (equivalent performance) - $2N_{rays}$. When ΔFeedback is negative, the covariance feedback method is able to produce equivalent performance with a reduced quantity of feedback. This only occurs in 23.8% of the measured channels. Again, this indicates that the performance of LS Covariance Feedback is inferior to that of Ray Model 1-D ESPRIT Feedback.

The results of MAXDET feedback applied to a subset of the measured channels are shown in Figure 6.14. It is interesting to note that the two covariance feedback methods produce equivalent mean performance until $N_{Qi} = 12$ and then the LS performance begins to climb more slowly than that of MAXDET. Additional details of this comparison can be seen in the CCDF of Capacity Ratio curves in Figure 6.15 where three values of N_{Qi} are displayed: 20,30,40. Table 6.2 shows the Capacity Ratio values which yield 10% Outage Probability. The difference between MAXDET and LS performance increases with larger values of N_{Qi}. Unfortunately, the computational

www.manaraa.com

Table 6.2: Capacity ratio value for 10% outage probability using LS and MAXDET covariance feedback.

Feedback \ $\mathbf{N_{Qi}}$	**20**	**30**	**40**
LS	0.817	0.838	0.851
MAXDET	0.823	0.862	0.895
Δ	0.006	0.024	0.044

load of MAXDET feedback determination is too prohibitive to offset the marginal improvements it produces even for larger N_{Qi}.

6.7 Conclusions

The best capacity performance using covariance feedback methods occurs at low values of SNR where the number of active eigenchannels is small. In these scenarios, feedback information identifies the eigenchannels where power should be allocated and results in significant gains over the uniform power allocation strategy. As the SNR increases, a few covariance feedback terms still produce capacity gains, but the marginal benefit of additional feedback terms is noticeably less.

MAXDET feedback determination method produces slight gains over the LS algorithm, particularly when the SNR is low. MAXDET's range of enhanced performance is more sustained with larger array sizes, but these gains are offset by MAXDET's increased computational load to the point that the LS algorithm is a better choice overall.

In comparison between LS Covariance Feedback and 1-D ESPRIT Ray Model Feedback used with measured 10×10 channels, Ray Model Feedback gives superior capacity performance. This can be observed both in terms of the typical amount of feedback required for equivalent performance as well as the capacity ratio obtained when using an equivalent quantity of feedback.

www.manaraa.com

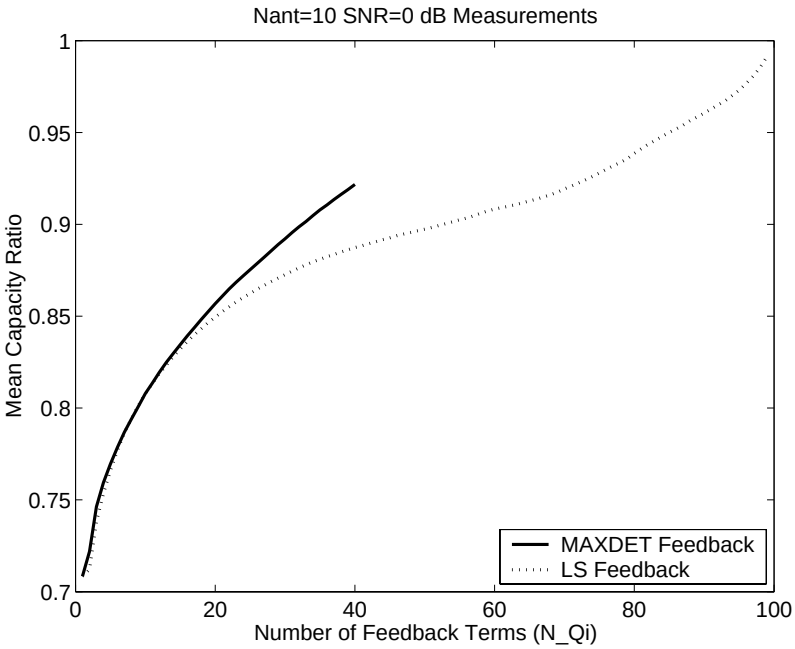

Figure 6.14: Mean capacity ratio using MAXDET V. LS covariance feedback (selected measurements)

www.manaraa.com

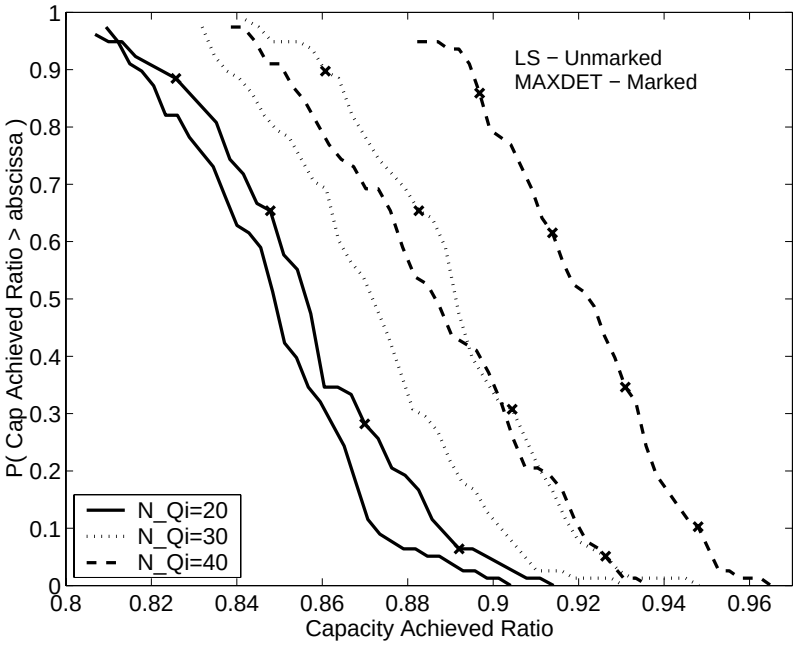

Figure 6.15: CCDF of capacity ratio - MAXDET V. LS covariance feedback (selected measurements)

www.manaraa.com

Chapter 7

Conclusions

7.1 Conclusions

The ray tracing simulations presented in this research confirm the time and angle clustering of ray arrivals in indoor channels observed by [6] and [7] and captured in the SVA model. Although the agreement between their measurements and deterministic simulation does not produce a ray for ray correspondence, the statistical distributions agree and produce model parameter estimates which are consistent. The ray tracing results indicate that the simulation's ability to predict time and angle related parameters is more robust than its predictions of power profiles. Our work also indicates that when modeling the indoor wireless transmission environment, the description of reflective scatters (such as door and window frames, rebar, and other metallic features) is more important than detailed information about the bulk materials (such as wall structure). While ray tracing offers a low cost alternative to channel sounding measurements, a reasonably high degree of detail is necessary to capture the important characteristics of the building within the geometry model.

Building on the discrete ray model of the MIMO communication channel, we presented several means to identify ray model parameters which can efficiently represent the channel state information for use in shaping the covariance of transmitted symbols for more optimum information capacity. Several feedback determination algorithms are investigated, including a 2-D Unitary Esprit method which solves directly for ray departure and arrival angles together with their pairing relationships.

www.manaraa.com

Although most of the algorithms gave nearly optimal results when perfect knowledge of the channel transfer matrix was available, the results degraded when using training-based estimation of the channel. In this more realistic case, the 1-D ESPRIT algorithm performed the best, yielding better than 90% of the ideal waterfilling capacity when adequate training is provided. It was observed that the performance gains from ray model feedback were most significant when the SNR was low. This scenario is ideal for feedback information because there are fewer eigenchannels in the waterfilling solution with non-zero power allocation, and the opportunity for improvement over uniform power allocation is much greater. As the SNR increases, the capacity gain from feedback is still significant, but as the performance of uniform power allocation increase, there is less room for improvement using feedback. We also used the 1-D ESPRIT ray model feedback algorithm to show the effects of typical assumptions about the random nature of the MIMO channel, and we observed that the SVA model and ray synthesis channel model yield comparable and significant capacity gains using ray model feedback. When the long term behavior of the channel matrix is averaged and assumed to be zero-mean and uncorrelated, the capacity gains of ray model feedback gains drop sharply. The ray model feedback methods were also applied to 10×10 measured channels taken to replicate the conditions used for the ray tracing simulations and earlier SISO measurements.

We also presented an alternative structure for feedback information using the transmitted symbol covariance. It was hoped that the symmetric, positive semi-definite structure of the covariance matrix would allow a reduction in the amount of feedback information required to realize significant capacity improvements over the uniform power allocation strategy. Having observed that minimizing the squared error to fit to a covariance matrix did not result in maximum capacity, we presented results for an alternative feedback determinant method, MAXDET, that directly maximized the capacity determinant subject to imposed constraints. MAXDET does produce some marginal capacity improvements over the traditional least squares method, but these gains are outweighed by MAXDET's increased computational burden which

www.manaraa.com

increase quickly with array size and number of feedback terms. Similar to the ray model feedback results, covariance feedback shows its most promising results under lower SNR conditions where there are fewer active eigenchannels. Significant improvements over the uniform allocation case can be achieved with a small number of feedback terms. However, the marginal capacity benefit of additional feedback decreases as more terms are added, and it is possible for the number of covariance feedback terms to outweigh to information required to simply feed back the unique entries of transmitted symbol covariance matrix. To assess the performance of covariance feedback relative to the ray model approach, we applied both methods to the 10 x 10 measured channel data. In this comparison, the ray model feedback had superior capacity performance - yielding increased capacity using equivalent amounts of feedback and delivering comparable capacity results with less feedback information. The covariance methods both required more computational effort than the 1-D ESPRIT ray feedback approach.

7.2 Suggestions for Future Work

- Use the ray tracing simulation tools to replicate other channel sounding measurements to investigate the validity of the current conclusions in varying channel environments.
- Investigate means to improve the quality the prediction of power-related behavior using the ray tracing software.
- Seek alternative feedback methods which use the additional information provided by the waterfilling solution about the number of eigenchannels with non-zero power allocated to them.
- Investigate the use of alternative methods for maximizing the feedback capacity with a minimum quantity of feedback information. Specifically, seek better ways

www.manaraa.com

of using the structure of the transmitted symbol covariance or the waterfilling solution to increase the capacity of the channel versus uniform power allocation.

- Investigate the affects of array geometries other than uniform linear array on the feedback determination algorithms and their performance.

www.manaraa.com

Appendix A

Covariance Feedback Simulation Figures

www.manaraa.com

This appendix includes additional figures displaying the results of the covariance feedback simulations described in Chapter 6. For more information on the contents and interpretation of these graphs, see Section 6.5.

4 Element Arrays $(T = R = N_{ant} = 4)$

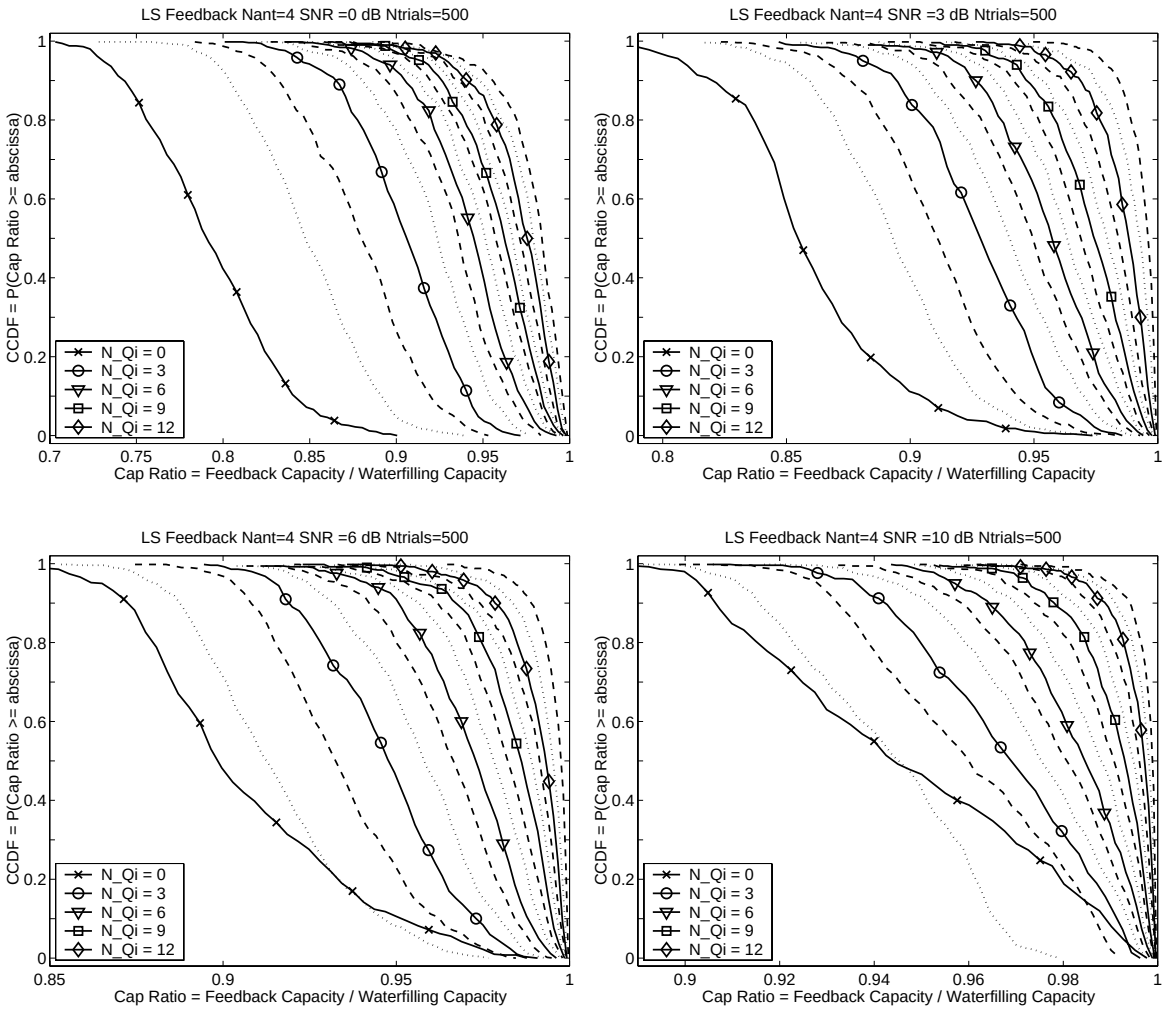

Figure A.1: CCDF of LS capacity ratio Nant = 4 SNR $\in \{0, 3, 6, 10$ dB$\}$ 500 trials

www.manaraa.com

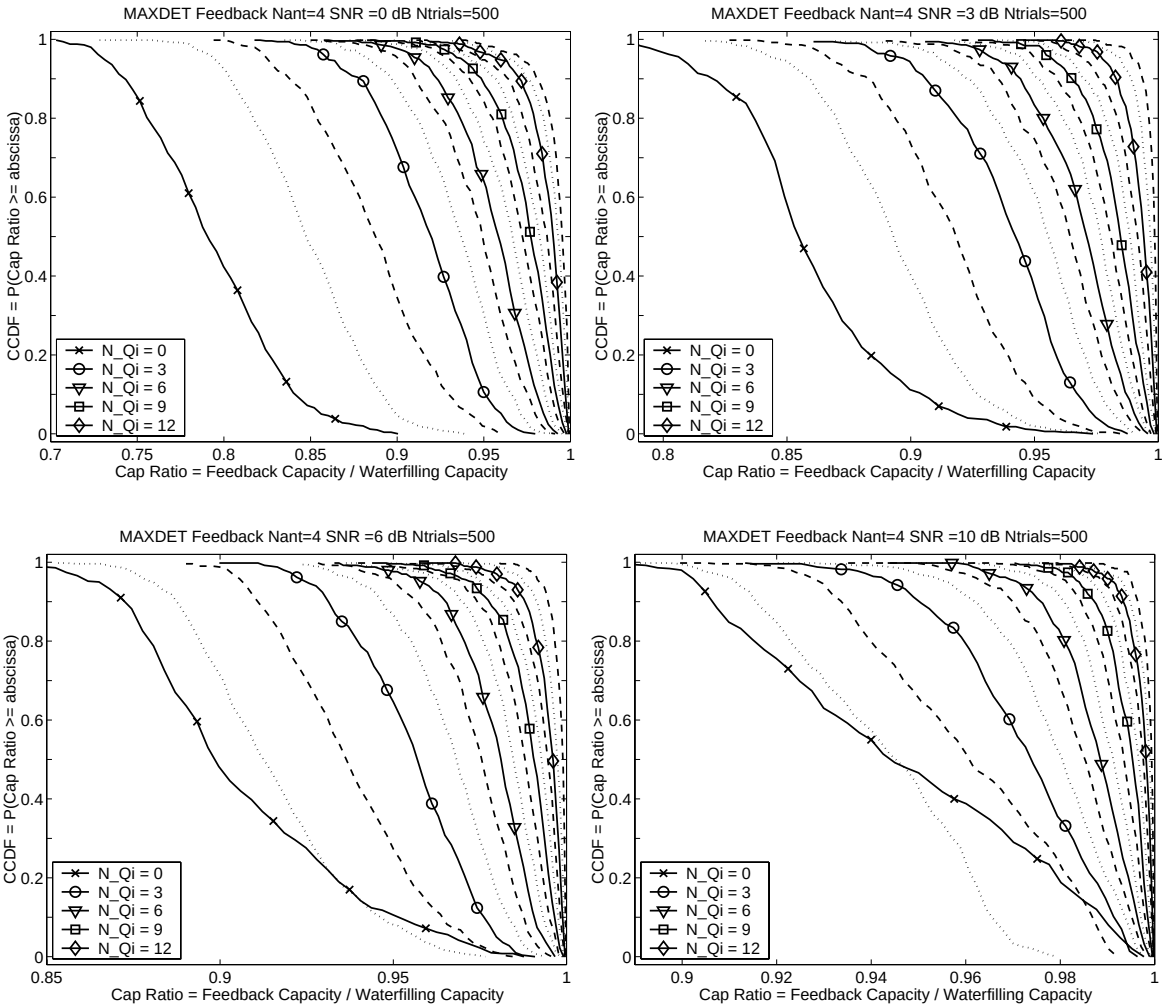

Figure A.2: CCDF of MAXDET capacity ratio $N_{ant} = 4$ SNR$\in \{0, 3, 6, 10$ dB$\}$ 500 trials

www.manaraa.com

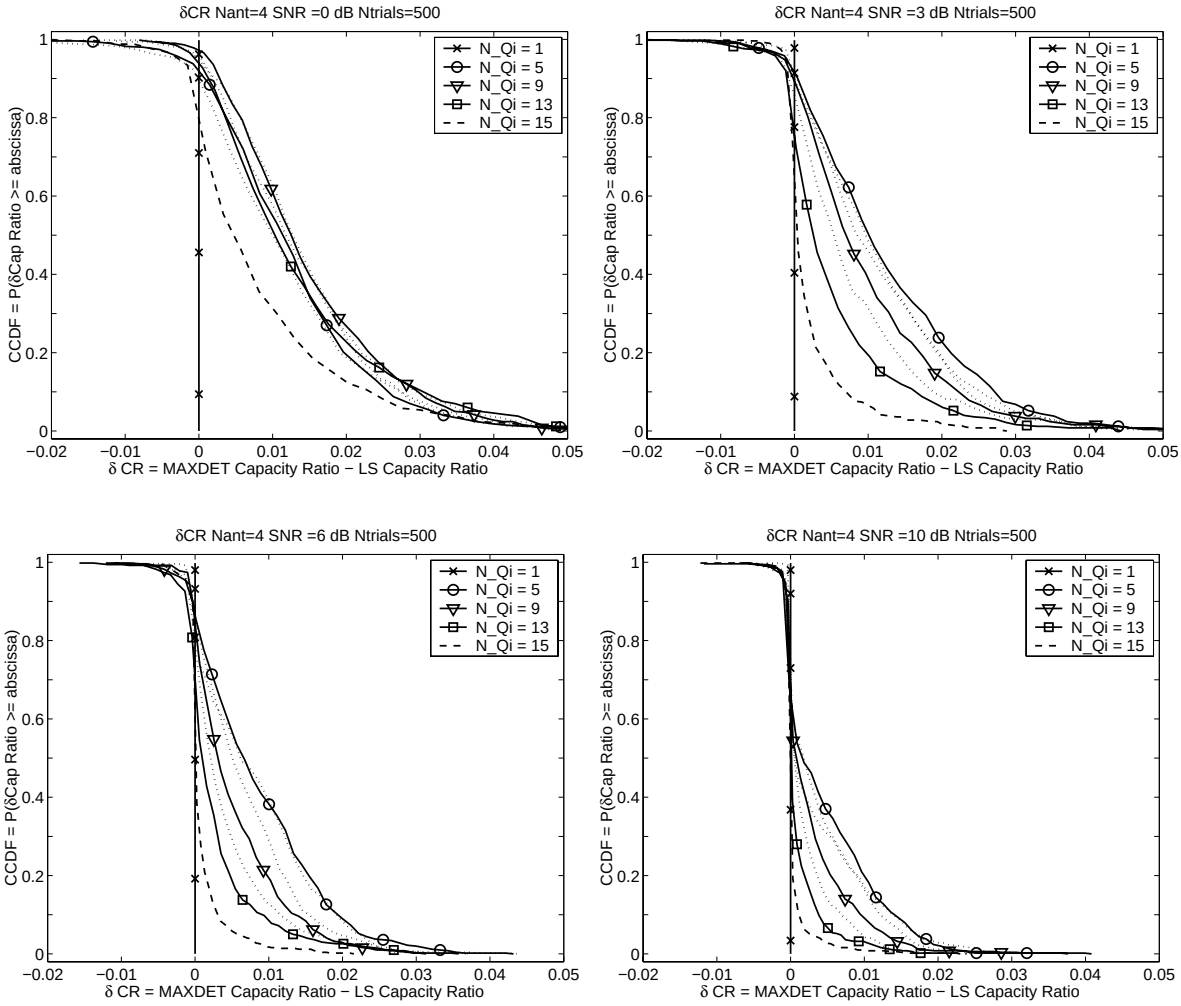

Figure A.3: CCDF of δCR Nant = 4 SNR $\in \{0, 3, 6, 10$ dB$\}$ 500 trials

www.manaraa.com

5 Element Arrays $(T = R = N_{ant} = 5)$

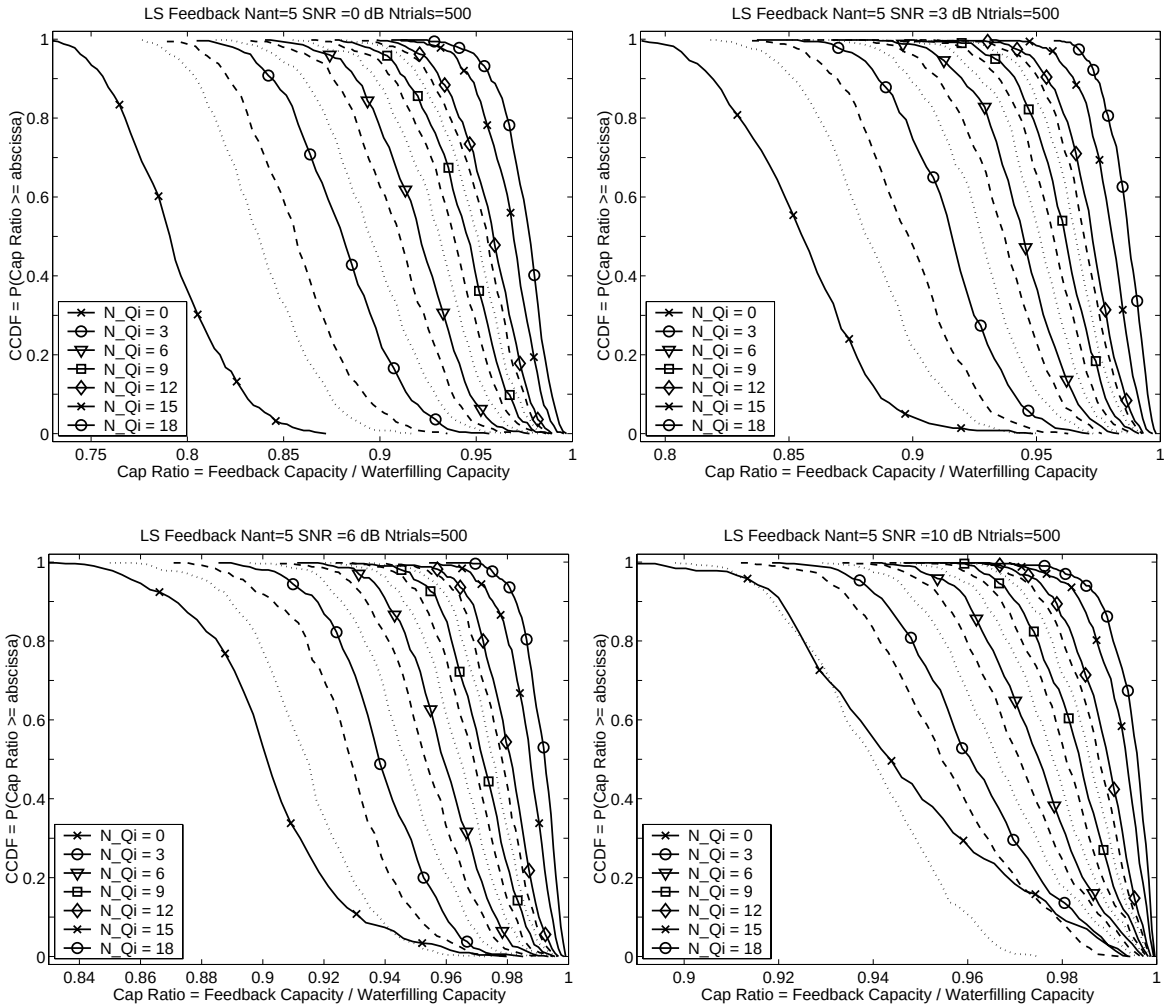

Figure A.4: CCDF of LS capacity ratio Nant = 5 SNR $\in \{0, 3, 6, 10\ \text{dB}\}$ 500 trials

www.manaraa.com

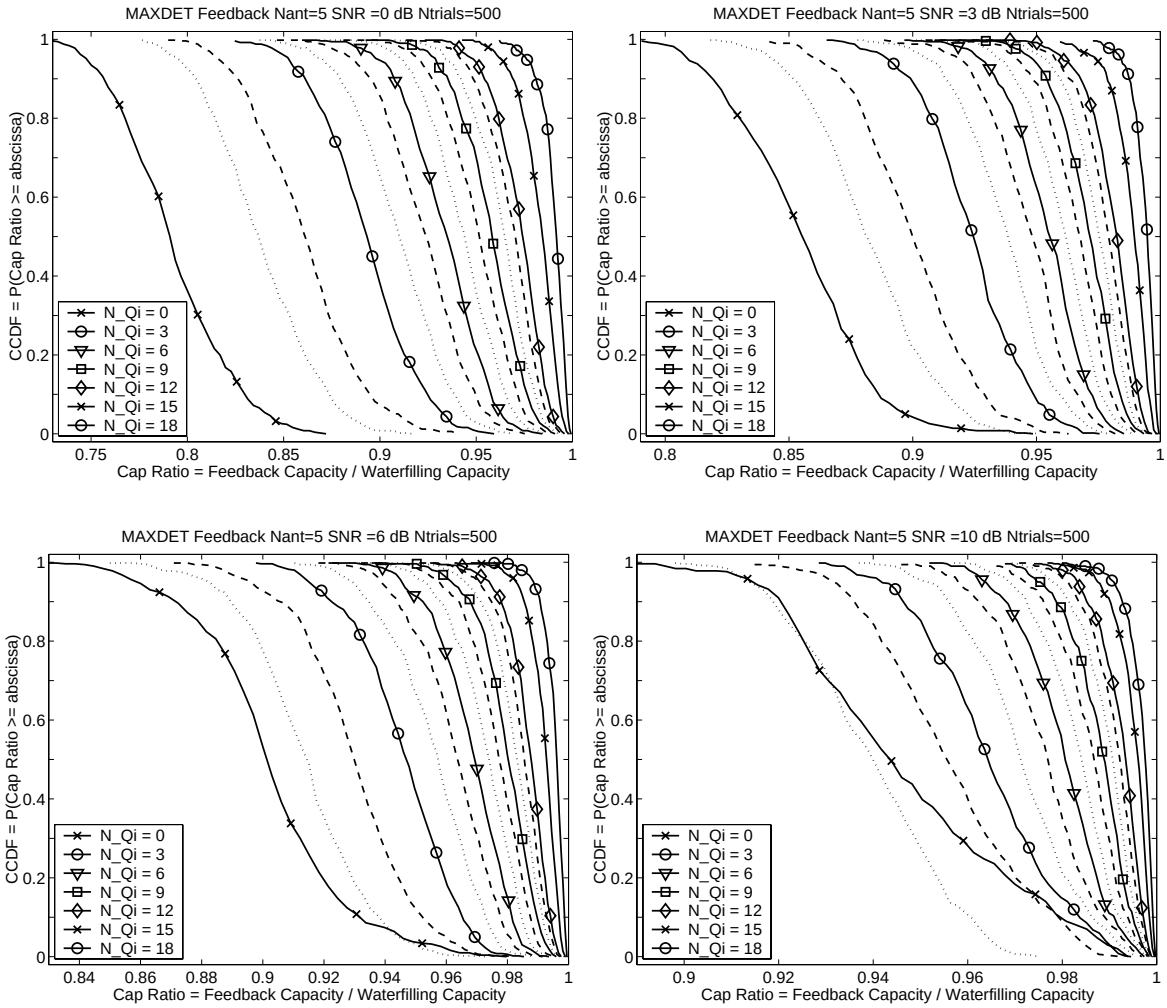

Figure A.5: CCDF of MAXDET capacity ratio $N_{ant} = 5$ SNR$\in \{0, 3, 6, 10$ dB$\}$ 500 trials

www.manaraa.com

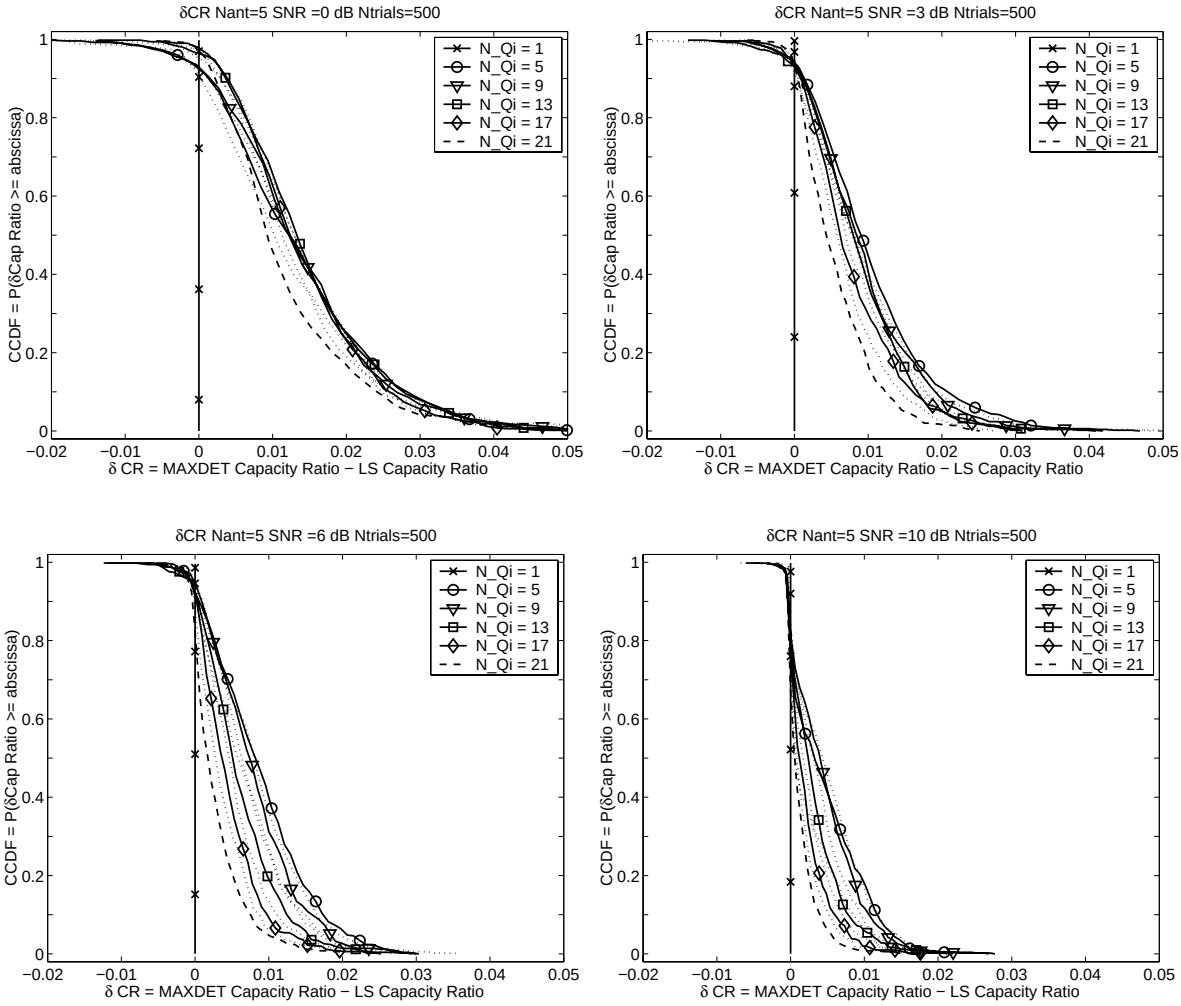

Figure A.6: CCDF of δCR Nant $= 5$ SNR $\in \{\, 0, 3, 6, 10$ dB$\}$ 500 trials

www.manaraa.com

Bibliography

[1] A. L. Swindlehurst, "A Quick Tutorial on Capacity." Brigham Young University Electrical Engineering 581 Class Notes.

[2] Q. H. Spencer, "Modeling the Time and Angle of Arrival Characteristics of an Indoor Multipath Channel," Master's thesis, Brigham Young University, December 1996.

[3] L. Telatar, "Capacity of Multi-Antenna Gaussian Channels," Technical Report #BL0112170-950615-07TM, AT&T Bell Laboratories, 1995.

[4] G. Foschini and M. Gans, "On Limits of Wireless Communications in a Fading Environment When Using Multiple Antennas," *Wireless Personal Communications*, vol. 6, 1998.

[5] K. Yu and B. Ottersten, "Models for MIMO Propagation Channels, A Review," in *Journal on Wireless Communications and Mobile Computing Special Issue: Adaptive Antennas and MIMO Systems*, John Wiley and Sons, August 2002. `http://www.s3.kth.se/~kaiyu/MIMOmodel.pdf`.

[6] Q. H. Spencer, B. D. Jeffs, M. A. Jensen, and A. L. Swindlehurst, "Modeling the Statistical Time and Angle of Arrival Characteristics of an Indoor Multipath Channel," *IEEE Journal on Selected Areas In Communications*, vol. 18, pp. 347–360, March 2000.

[7] A. Saleh and R. Valenzuela, "A Statistical Model for Indoor Multipath Propagation," *IEEE Journal on Selected Areas of Communications*, vol. SAC-5, pp. 128–137, February 1987.

www.manaraa.com

[8] A. Goldsmith, S. A. Jafar, *et al.*, "Capacity Limits of MIMO Channels," *IEEE Journal on Selected Areas of Communications*, vol. 21, pp. 684–702, June 2003.

[9] S. J. Fortune, D. M. Gay, *et al.*, "WISE Design of Indoor Wireless Systems," *IEEE Computational Science and Engineering*, vol. 2, pp. 58–68, Spring 1995.

[10] T. Zwick, C. Fischer, and W. Wiesbeck, "A Stochastic Multipath Channel Model Including Path directions For Indoor Environments," *IEEE Journal on Selected Areas of Communications*, vol. 20, pp. 1178–1192, August 2002.

[11] H. Ge, K. Wong, M. Barton, and J. Liberty, "Statistical characterization of multiple-input multiple-output (MIMO) channel capacity," *Wireless Communications and Networking Conference, 2002. WCNC2002*, vol. 2, pp. 789–793, 17-21 March 2002.

[12] D. Gespert, D. Bolcskei, *et al.*, "MIMO wireless channels: capacity and performance prediction," *Global Telecommunications Conference, 2000. GLOBECOM '00*, vol. 2, pp. 1083–1088, 27 Nov.-1 Dec. 2000.

[13] G. Povey and D. Levey, "Multiple input multiple output (MIMO) radio channel models," *3G Mobile Communication Technologies, 2002. Third International Conference on (Conf. Publ. No. 489)*, pp. 414–417, 8-10 May 2002.

[14] K. Liu, V. Raghavan, and A. Sayeed, "Capacity scaling and spectral efficiency in wide-band correlated MIMO channel," *Information Theory, IEEE Transactions on*, vol. 49, pp. 2504–2526, Oct 2003.

[15] M. Grzonka and Z. Wtodzimieri, "Two dimensional indoor ray tracing including geometrical theory of diffraction," *Microwaves, Radar and Wireless Communications, 2002. MIKON-2002*, vol. 2, pp. 437–440, 20-22 May 2002.

[16] Y. Lostanlen, Y. Corre, *et al.*, "Comparison of measurements and simulations in indoor environments for wireless local networks at 60 GHz," *Vehicular Technology Conference, 2002. VTC Spring 2002*, vol. 1, pp. 389–393, 6-9 May 2002.

www.manaraa.com

[17] B. Lee, A. Nix, and J. McGeehan, "Indoor space-time propagation modelling using a ray launching technique," *Antennas and Propagation, 2001. Eleventh International Conference on (IEE Conf. Publ. No. 480)*, vol. 1, pp. 279–283, 17-20 April 2001.

[18] A. Burr, "Evaluation of capacity of indoor wireless MIMO channel using ray tracing," *Broadband Communications, 2002. Access, Transmission, Networking. 2002 International Zurich Seminar on*, pp. 28–1 – 28–6, 19-21 Feb. 2002.

[19] D. Browne, J. Medbo, *et al.*, "A simple approach to site sensitive modeling of indoor radio propagation," *Vehicular Technology Conference, 2002. VTC Spring 2002. IEEE 55th*, vol. 1, pp. 384–388, 6-9 May 2002.

[20] S. Nagata, T. Toda, *et al.*, "Prediction and validation of propagation loss in urban micro-cell environment by using ray tracing simulation," *Wireless Personal Multimedia Communications, 2002. The 5th International Symposium on*, vol. 2, pp. 573–576, 27-30 Oct. 2002.

[21] P. Wertz, V. Cvijic, *et al.*, "Wave propagation modeling inside vehicles by using a ray tracing approach," *Vehicular Technology Conference, 2002. VTC Spring 2002. IEEE 55th*, vol. 3, pp. 1264–1268, 6-9 May 2002.

[22] J. Chen and S. Hall, "Efficient indoor and outdoor EM wave propagation in a compact terrain database (CTDB) representation of the urban canyon environment," *Vehicular Technology Conference, 2002. Proceedings. VTC 2002-Fall. 2002 IEEE 56th*, vol. 2, pp. 802–806, 24-28 Sept. 2002.

[23] F. Tila, P. Shepherd, and S. Pennock, "Theoretical capacity evaluation of indoor micro- and macro-MIMO systems at 5 GHz using site specific ray tracing," *Electronics Letters*, vol. 39, 6 March 2003.

www.manaraa.com

[24] T. Rautiainen, G. Wolfle, and R. Hoppe, "Verifying path loss and delay spread predictions of a 3D ray tracing propagation model in urban environment," *Vehicular Technology Conference, 2002. Proceedings. VTC 2002-Fall. 2002 IEEE 56th*, vol. 4, pp. 2470–2474, 2002.

[25] J. Medbo and J.-E. Berg, "Spatio-temporal channel characteristics at 5 GHz in a typical office environment," *Vehicular Technology Conference, 2001. VTC 2001 Fall. IEEE VTS 54th*, vol. 3, pp. 1256–1260, 7-11 Oct. 2001.

[26] J. Zhang and Y. Huang, "Indoor channel characteristics comparisons for the same building with different dielectric parameters," *Communications, 2002. ICC 2002. IEEE International Conference on*, vol. 2, pp. 916–920, 28 April-2 May 2002.

[27] D. Pena, R. Feick, *et al.*, "Measurement and modeling of propagation losses in brick and concrete walls for the 900-MHz band," *Antennas and Propagation, IEEE Transactions on*, vol. 51, pp. 31–39, Jan. 2003.

[28] J. Kim, K. Kim, *et al.*, "A study on the indoor propagation channel model for MIMO system," *Antennas and Propagation Society International Symposium, 2003. IEEE*, vol. 2, pp. 118–121, 22-27 June 2003.

[29] C. Passerini, "A quality measure for ray-tracing algorithms," *Antennas and Propagation, IEEE Transactions on*, vol. 49, pp. 500–502, March 2001.

[30] V. Erceg, S. Fortune, *et al.*, "Comparisons of a computer-based propagation prediction tool with experimental data collected in urban microcellular environments," *Selected Areas in Communications, IEEE Journal on*, vol. 15, pp. 677–684, May 1997 1997.

[31] C.-N. Chuah, J. Kahn, and D. Tse, "Capacity of multi-antenna array systems in indoor wireless environment," *Global Telecommunications Conference, 1998. GLOBECOM 98. The Bridge to Global Integration. IEEE*, vol. 4, pp. 1894–1899, 8-12 Nov. 1998.

www.manaraa.com

[32] D. Tse, C.-N.Chuah, and J. Kahn, "Capacity scaling in dual-antenna-array wireless systems," *Wireless Communications and Networking Conference, 2000. WCNC. 2000 IEEE*, vol. 1, pp. 25–29, 23-28 Sept. 2000.

[33] J. Ling, D. Chizhik, and R. Valenzuela, "Predicting multi-element receive & transmit array capacity outdoors with ray tracing," *Vehicular Technology Conference, 2001. VTC 2001 Spring. IEEE VTS 53rd*, vol. 1, pp. 392–394, 6-9 May 2001.

[34] C.-N. Chuah, G. Foschini, *et al.*, "Capacity growth of multi-element arrays in indoor and outdoor wireless channels," *Wireless Communications and Networking Conference, 2000. WCNC. 2000 IEEE*, vol. 3, pp. 1340–1344, 23-28 Sept. 2000.

[35] S. Guillouard, G. E. Zein, and J. Citerne, "Wideband propagation measurements and Doppler analysis for the 60 GHz indoor channel," *MTT Symposium Anaheim, USA*, 13-18 June 1999.

[36] D. Courivaud, C. Humbert, and M. Sylvain, "2 GHz single-floor indoor propagation results," *EUROCON'2001, Trends in Communications, International Conference on*, vol. 2, pp. 309–311, 4-7 July 2001.

[37] M.Stoytchev, J. Raveche, and H. Safar, "Joint spatial and temporal characterization of the wideband wireless communication channel for MIMO applications," *Radio and Wireless Conference, 2001. RAWCON 2001. IEEE*, pp. 233–236, 19-22 Aug. 2001.

[38] M. Batariere, T. Blankenship, *et al.*, "Wideband MIMO mobile impulse response measurements at 3.7 GHz," *Vehicular Technology Conference, 2002. VTC Spring 2002. IEEE 55th*, vol. 1, pp. 26–30, 6-9 May 2002.

www.manaraa.com

[39] R. Stridh, B. Ottersten, and P. Karlsson, "MIMO channel capacity of a measured indoor radio channel at 5.8 GHz," *Signals, Systems and Computers, 2000. Conference Record of the Thirty-Fourth Asilomar Conference on*, vol. 1, pp. 733–737, Oct.-1 Nov. 2000.

[40] V. Erceg, P. Soma, *et al.*, "Capacity obtained from multiple-input multiple-output channel measurements in fixed wireless environments at 2.5 GHz," *Communications, 2002. ICC 2002. IEEE International Conference on*, pp. 396–400, 28 April-2 May 2002.

[41] K. Kuroda, K. Sakaguchi, *et al.*, "FDM based MIMO spatio-temporal channel sounder," *Wireless Personal Multimedia Communications, 2002. The 5th International Symposium on*, vol. 2, pp. 559–562, 27-30 Oct. 2002.

[42] J. Wallace, M. Jensen, A. Swindlehurst, and B. Jeffs, "Experimental Characterization of the MIMO Wireless Channel: Data Acquisition and Analysis," *IEEE Transactions on Wireless Communications*, vol. 2, pp. 335–343, March 2003.

[43] J. Wallace and M. Jensen, "Spatial characteristics of the MIMO wireless channel: experimental data acquisition and analysis," *Acoustics, Speech, and Signal Processing, 2001. Proceedings. (ICASSP '01). 2001 IEEE International Conference on*, vol. 4, pp. 2497–2500, 7-11 May 2001.

[44] J. Wallace and M. Jensen, "Experimental characterization of the MIMO wireless channel," *Antennas and Propagation Society International Symposium, 2001. IEEE*, vol. 3, pp. 92–95, 8-13 July 2001.

[45] C. Martin, J. Winters, and N. Sollenberger, "Multiple-input multiple-output (MIMO) radio channel measurements," *Vehicular Technology Conference, 2000. IEEE VTS-Fall VTC 2000. 52nd*, vol. 2, 24-28 Sept. 2000.

www.manaraa.com

[46] J. Kermoal, L. Schumacher, *et al.*, "Experimental investigation of correlation properties of MIMO radio channels for indoor picocell scenarios," *Vehicular Technology Conference, 2000. IEEE VTS-Fall VTC 2000. 52nd*, vol. 1, pp. 14–21, 24-28 Sept. 2000.

[47] D. McNamara, M. Beach, *et al.*, "Initial characterisation or multiple-input multiple-output (MIMO) channels for space-time communication," *Vehicular Technology Conference, 2000. IEEE VTS-Fall VTC 2000. 52nd*, vol. 3, pp. 1193–1197, 24-28 Sept. 2000.

[48] D. Hampicke, M. Landmann, *et al.*, "MIMO capacities for different antenna array structures based on double directional wide-band channel measurements," *Vehicular Technology Conference, 2002. Proceedings. VTC 2002-Fall. 2002 IEEE 56th*, vol. 1, pp. 180–184, 24-28 Sept 2002.

[49] A. Richter, D. Hampicke, *et al.*, "MIMO measurement and joint M-D parameter estimation of mobile radio channels," *Vehicular Technology Conference, 2001. VTC 2001 Spring. IEEE VTS 53rd*, vol. 1, pp. 214–218, 6-9 May 2001.

[50] M. Steinbauer, A. Molisch, and E. Bonek, "The double-directional radio channel," *Antennas and Propagation Magazine, IEEE*, vol. 43, pp. 51–63, August 2001.

[51] M. Skoglund and G. Jongren, "On the capacity of a multiple-antenna communication link with channel side information," *Selected Areas in Communications, IEEE Journal on*, vol. 21, pp. 395–405, April 2003.

[52] A. Sutivong, T. Cover, and M. Chiang, "Tradeoff between message and state information rates," *Information Theory, 2001. Proceedings. 2001 IEEE International Symposium on*, p. 303, 24-29 June 2001.

www.manaraa.com

[53] A. Medles, S. Visuri, and D. Slock, "On MIMO capacity for various types of partial channel knowledge at the transmitter," *Information Theory Workshop, 2003. Proceedings. 2003 IEEE*, pp. 99–102, 31 March-4 April 2003.

[54] S. Bhashyam, A. Sabharwal, and B. Aazhang, "Feedback gain in multiple antenna systems," *Communications, IEEE Transactions on*, vol. 50, pp. 785–798, May 2002.

[55] E. Visotsky and U. Madhow, "Space-time transmit precoding with imperfect feedback," *Information Theory, IEEE Transactions on*, vol. 47, pp. 2632–2639, Sept 2001.

[56] S. Jafar and A. Goldsmith, "On optimality of beamforming for multiple antenna systems with imperfect feedback," *Information Theory, 2001. Proceedings. 2001 IEEE International Symposium on*, p. 321, 24-29 June 2001.

[57] S. Jafar, S. Vishwanath, and A. Goldsmith, "Channel capacity and beamforming for multiple transmit and receive antennas with covariance feedback," *Communications, 2001. ICC 2001. IEEE International Conference on*, vol. 7, pp. 2266–2270, 11-14 June 2001.

[58] M. Kang and M.-S. Alouini, "Impact of correlation on the capacity of MIMO channels," *Communications, 2003. ICC '03. IEEE International Conference on*, vol. 4, pp. 2623–2627, 11-15 May 2003.

[59] O. Oyman, R. Nabar, *et al.*, "Characterizing the statistical properties of mutual information in MIMO channels," *Signal Processing, IEEE Transactions on*, vol. 51, pp. 2784–2795, November 2003.

[60] T. Cover and J. Thomas, *Elements of Information Theory*. John Wiley and Sons, 1991.

[61] L. L. Scharf, *Statistical Signal Procession: Detection, Estimation, and Time Series Analysis*. Addison-Wesley, 1991.

www.manaraa.com

[62] The MathWorks Inc., *Matlab Function Reference, Release 12*. 'poly' command.

[63] J. E. Freund, *Mathematical Statistics*. Prentice Hall, 5th ed., 1992.

[64] G. G. Raleigh and J. M. Cioffi, "Spatio-Temporal Coding for Wireless Communication," *IEEE Transactions on Communications*, vol. 46, pp. 357–366, March 1998.

[65] B. D. Jeffs and J. Wallace, "MIMO Wireless Multipath Ray Parameter Estimation From Channel Transfer Matrix Measurements," in *Acoustics, Speech, and Signal Processing, 2002 IEEE International Conference on*, pp. 2345–2348, 2002.

[66] R. Schmidt, "Multiple Emitter Location and Signal Parameter Estimation," in *Proceedingcs of RADC Spectrum Estimation Workshop*, pp. 243–258, Griffiths AFB, Rome, NY, 1979.

[67] G. Bienvenu and L. Kopp, "Adaptivity to Background Noise Spatial Coherence for High Resolution Passive Methods," in *Proceedings ICASSP*, vol. 1, pp. 307–310, Denver, Colorado, April 1980.

[68] H. L. VanTrees, *Optimum Array Processing*. John Wiley and Sons, 2002.

[69] R. Roy, *ESPRIT: Estimation of Signal Parameters via Rotational Invatiance Techniques*. PhD thesis, Stanford University, 1987.

[70] A. L. Swindlehurst, *Applications of Subspace Fitting to Estimation and Identification*. PhD thesis, Stanford University, 1991.

[71] G. H. Golub and C. F. Van Loan, *Matrix Computations*. Johns Hopkins University Press, third ed., 1996.

[72] T. K. Moon and W. C. Stirling, *Mathematical Methods and Algorithms for Signal Processing*. Prentice Hall, 2000.

www.manaraa.com

[73] M. D. Zoltowski *et al.*, "Closed-Form 2-D Angle Estimation with Rectangular Arrays in Element Space or Beamspace via Unitary ESPRIT," *IEEE Transactions on Signal Processing*, vol. 44, pp. 316–328, February 1996.

[74] "`http://ee.byu.edu/ee/wireless/data/probe_narrow/info.cgi?data_012501`."

[75] L. Vandenberghe, S. Boyd, and S.-P. Wu, "Determinant Maximization with Linear Matrix Inequality Constraints," *SIAM Journal on Matrix Analysis and Applications*, vol. 19, no. 2, pp. 499–533, 1998.

[76] S.-P. Wu, L. Vandenberghe, and S. Boyd, *MAXDET: Software for determinant maximization problems: Users guide, alpha version.* Stanford Univ., Apr. 1996. `http://www.stanford.edu/~boyd/maxdet/doc.pdf`.

[77] L. Vandenberghe and S. Boyd, "Semidefinite programming," *SIAM Review*, vol. 38, no. 1, pp. 49–95, 1996.

[78] E. Klerk, C. Roos, and T. Terlaky, "A short survey on semidefinite programming," in *Ten Years LNMB, Ph.d. Research and Graduate Courses of the Dutch Network of Operations Research* (W. K. K. H. et al., ed.), vol. 122, pp. 323–339, Amsterdam, The Netherlands: Centrum for Mathematics and Informatics (CWI), 1997. `http://citeseer.nj.nec.com/deklerk97short.html`.

[79] B. S and L. Vandenberghe, *Convex Optimization.* Cambridge University Press, 2003. `http://www.stanford.edu/~boyd/cvxbook.html`.

www.manaraa.com